UNIVERSITA' DEGLI STUDI DI PARMA

Dottorato di ricerca in Scienza e Tecnologia dei Materiali

Ciclo XXIX

Development of printed semiconducting gas sensors: industrial, medical and environmental applications

Coordinatore:
Chiar.mo Prof. Enrico Dalcanale

Tutor:
Chiar.mo Ing. Antonino Bonanno

Co-Tutor:
Chiar.ma Dott. Maria Cristina Carotta
Chiar.mo Prof. Michele Sacerdoti

Dottorando: Ambra Fioravanti

In memory of Ing. Roberto Paoluzzi
Director of CNR-IMAMOTER

TABLE OF CONTENTS

INTRODUCTION

As a human being collects information about the surrounding environment with its senses, a sensor elaborates the signals perceived by a sensing element. However, while the reaction of a human being results into an emotional or intellectual behavior, the sensor only responds with analytical data.

The term “sensor” started to gain currency during the 1970s, and it identifies a transducer (or device) that detects and converts events or changes in its environment into data usefully observed or processed. In principle, the input quantity measured and the output data provided can be of various type (chemical, electrical, magnetic, mechanical, thermal, radiant, etc.) making the sensors an essential tool both in scientific applications and in everyday life. Their development was mainly reinforced by technological improvements, in term of new nanostructured materials, microelectronics and miniaturization, and by the demand of real time, low cost and online devices. Over the years, the development of sensors for several applications ranging from micromechanics to medical diagnostics is so increased that the first decade of the 21st century has been labelled as “the sensor decade” [1].

The gas sensing application too is in great demand, to control a large variety of parameters such as environmental, food quality, biomedical, industrial process control, etc..

Nowadays there is a variety of structures, materials and working principles exploitable to realize gas sensors. Among them, semiconductor gas sensors using metal oxides (MOX) as gas sensing element are a convenient choice to detect a wide range of gases both in scientific research and in industrial applications. Although the metal oxides used as sensing materials have wide band gap typical of insulators, they possess conductivity in the range of semiconductors due to point defects in crystal structure. The gas sensing devices generally consist of a MOX semiconductor between two metal electrodes and respond to changes in the composition of the surrounding atmosphere with a change in conductance [2]. This transduction mechanism of solid-state semiconducting gas sensors is normally referred to as chemo-resistive effect [3] and it is deepened in Chapter 1.

The first evidence about the dependence of electrical conductance from the concentration of the gases in the environment was reported in a seminal work by Brattain and Bardeen (1953) [4]. However, the first generation of commercial devices based on SnO_2 deposited via thick-film technology appeared in the sixties by Taguchi [5], who established the Figaro Engineering Inc.

Afterwards, chemo-resistive sensors grabbed the attention of researchers and investors with respect to different functional nanomaterials and many other techniques because this kind of sensors can be fabricated cheaply, are very compact, low-power consuming and easy to use and to implement.

The MOX sensors, can be in form of thin or thick films deposited trough screen-printing technique, spin coating, deep coating, sputtering, chemical vapor deposition, physical vapor deposition, epitaxial growth etc.. The sensing layers can be deposited onto different substrates, such as alumina, zirconia, quartz, beryllium oxide, micromachined silicon, etc.. The typical functional materials are ZnO, TiO_2, SnO_2, WO_3, Fe_2O_3, $LaFeO_3$, solid solutions as $(Ti_x,Sn_{1-x})O_2$, added with noble metals as catalyzers or foreign ions with the role of sensitizers or conductivity modifiers, or organic molecules, functionalized graphene oxide, nanocomposites, etc..

In this work, MOX sensors are in form of thick films and they have been deposited through screen-printing technique. Indeed, the mass-production capacity (up to some hundreds of sensors at a time) at low cost with respect to other technologies, combined with devices reliability in harsh operating conditions, makes thick film planar technology particularly suitable for sensors production. They have been deposited onto alumina substrates provided with comb-type electrodes and heating elements to give to the sensor the working temperature suitable to detect the desired gas. Usually such temperature is in the range 300 – 500 °C. The functional materials must be nanosized and for this reason they have been synthesized through wet chemistry processes. The composition of the functional material, the morphology and the size at nanometric level dominate electrical and sensitivity properties of the thick films. A detailed description of the realization of sensors trough screen-printing technology is reported in Chapter 2.

Among the functional materials prepared, ZnO has been mainly investigated due to its many and various properties, synthesizing several nanostructures (nanoparticle aggregates and elongated nanocrystals). The correlation between the obtained different morphologies and the electrical and spectroscopic behavior has been examined. Moreover ZnO gas sensors have been tested toward several reducing gases (acetone, ethanol, ammonia, etc.) typically found in exhaled human breath with the aim to use them in breath gas analysis for diagnosis of metabolic diseases. In Chapter 3, the synthesis process, the morphological, structural, spectroscopic and electrical characterizations, as well as the gas sensing properties of ZnO nanostructures are examined.

A second concrete implementation in industrial framework of the thick film gas sensors realized has been concerning the monitoring of the hydraulic oil aging. This is a novel approach (currently in patent stage) to the monitoring the aging of the hydraulic oil in real time and on-board both from a

methodological and instrumental standpoint. The same type of hydraulic oil was aged and collected using an hydraulic test bench developed at IMAMOTER-CNR and directly in a agrimotor. The oil samples have been characterized by means of gas chromatography and of a laboratory system, based on sensors, specifically prepared for this aim. It has been examined a correlation between the hydraulic oil aging and the composition of their vapors. For this application, oil samples have been also analyzed through organic electrochemical liquid sensors developed at IMEM-CNR. In Chapter 4, the oil samples collection, the methodologies used, the devices employed and the experimental results are discussed.

Finally, in Chapter 5, the description of a portable monitoring station, based on the MOX sensors, for the monitoring of traces of main atmospheric pollutant gases and some in-field experiment are came under review.

The monitoring station has been arranged, including electronics for acquisition, processing and wireless transmission of the data. A particular attention has been addressed to the development of a suitable sensor for each atmospheric pollutant gas detected (carbon monoxide, nitrogen dioxide, ozone and BTX). The in-field experiments performed during this work concerned an industrial zone in Ferrara in addition to a monitoring in Naples at monumental site of "Maschio Angioino" leaning out of an arterial road of heavy traffic close to docklands. The comparison performed between the temporal evolution of the conductivity changes of the sensors with the pollutants' concentrations, as measured by the analytical instruments located in fixed monitoring stations managed by ARPA resulted in good agreement.

REFERENCES

[1] J. S. Wilson (Ed.), Sensor technology Handbook, *Elsevier Inc*., 2005.

[2] P. Romppainen, *Acta Univ. Oul C* 47, 1988.

[3] M. J. Madou, S. R. Morrison, Chemical Sensing with Solid State Devices, *New York, Academic Press, Inc*., 1989.

[4] W. H. Brattain, J. Bardeen, *Bell System Tech. J* 32 (1953) 1.

[5] N. Taguchi, 1970 *Patent specification* 1280809.

CHAPTER 1

SEMICONDUCTING OXIDES GAS SENSORS: EXPERIMENTAL EVIDENCES AND RESPONSE MODELING

1.1 INTRODUCTION

Over the years, the demand of real time, low cost and small size devices is continuing to increase. In particular, the development of sensors for various applications ranging from micromechanics to medical diagnostics is so increased that the first decade of the 21st century has been labelled as “the sensor decade” [1].

The gas sensing application too is in great demand, to control a large variety of parameters such as environmental, food quality, biomedical, etc. [2-7]. In this area, recent advances in nanotechnology have been driven to an extensive investigation on semiconductor metal oxides (MOX), particularly in form of nanoceramic materials [8-11].

Sensors are devices changing almost one physical property as a result of a change of a physical or chemical property of the ambient. In particular the chemical sensors are devices changing a physical property (electrical, optical, etc.) as a result of a chemical interaction with the ambient. In this work, the sensors of interest are chemoresistive, which change their conductivity (bulk or surface) as a result of a chemical interaction with the gaseous ambient. In this frame, two categories of processes can be distinguished: i) variation in bulk conductance, which is of ionic type (it is applied the Nernst law); this type of sensors are used to control combustion processes by measuring oxygen partial pressure. The typical materials are zirconia and titania, being the working temperature greater than 700 °C; ii) variation in surface conductance is the physical quantity to measure traces of gases at constant oxygen pressure; the functional materials are metal oxides, such as SnO_2, TiO_2, In_2O_3, WO_3, ZnO, $LaFeO_3$, etc., solid solutions of them, while noble metals or foreign ions are added as catalysts or conductivity modifiers, the working temperature ranging between 200 and 500 °C.

The semiconductor oxides exhibit conductivity due to stoichiometric defects: in the ones of type n, such defects are oxygen vacancies behaving as donor levels; indeed, remaining the electrons weakly bounded, they easily enter into the conduction band. Such electrons contribute to the building of the

Schottky barrier *eVs* when they are captured by the acceptor surface states (in sensing materials oxygen atoms).

In a *n-type* semiconductor, the Schottky barrier formation occurs when the electrochemical potential at the surface is lower than that of the electrons in the conduction band. The electrons (ionized donors of the bulk) will occupy the acceptor surface states until the Fermi level will be identical in the two regions. In the diagram of the Fig. 1.1 A, the surface states are assumed neutral (acceptor states unoccupied and donor states occupied) with the Fermi level of the bulk in the middle between the bottom of the conduction band and the level of donors, while at the surface, the Fermi level is in the middle between the donor and acceptor surface states. This is an ideal case, the so-called case of "flat band". Indeed, as reported in the Fig. 1.1 B, the electrons will occupy the acceptor surface states until an equilibrium situation will be achieved.

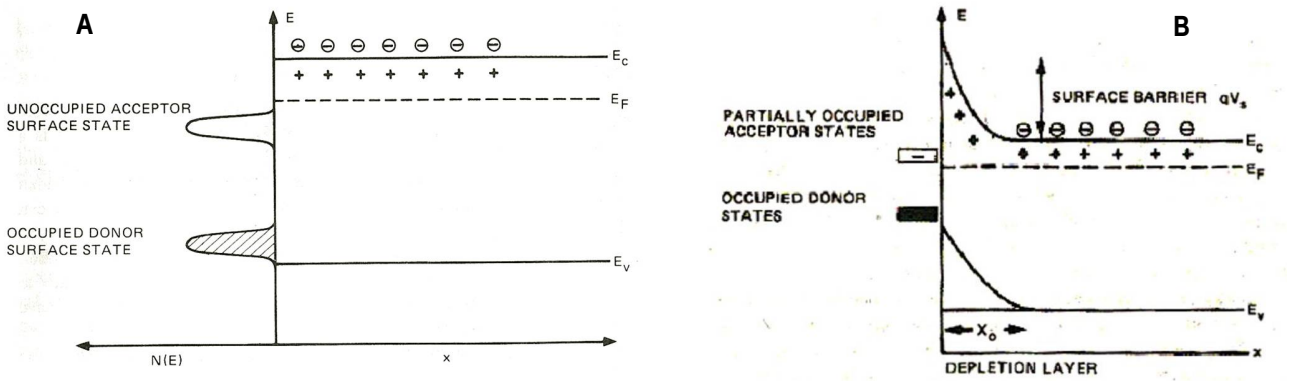

Fig. 1.1. Surface state bands in a semiconductor of n-type: A) flat band case; B) electron from the conduction band are captured by surface states, leading to a negatively charges surface with the counter-charge due to the positively charged donors near the surface (from Madou, Morrison, Chemical sensing with solid state devices, Academic Press Inc, San Diego, CA, 1989, p.26.).

The semiconductor oxides, differently from covalent semiconductors like silicon, prevalently exhibit ionic bonds, more localized in space and consequently more spread in energy, thus reducing the pinning effect of Fermi level [12]. This characteristic usually allows the semiconductor oxides to be used as gas sensors; indeed, as explained later, the surface potential depends on the environmental work function. In nanocrystalline semiconductors, the mechanism of conduction is thereby controlled by the presence of a huge series of intergranular point contacts at which a surface barrier develops, due to the presence of charged surface states. Conductance therefore is an activated process, since only those electrons with sufficient energy to cross the barrier take part to electrical conductance [13]. The sensing mechanism is

based on the variation of the potential barrier height as a result of surface chemical reactions with environmental gases, leading to the electrical conductance modification. Such a mechanism properly works when the temperature, usually between 200 and 500 °C, is optimized with respect to both functional material and detecting gas.

Starting with this peculiar mechanism, a lot of features determine the sensor performances, but certainly the grain size reduction at nanometric level is one of the main factors enhancing their detection properties [14–16], both for large specific surface offered and for the influence in reducing the surface charge density. Indeed, when the particle dimensions scale down below a critical value, the phenomenon of the unpinning of Fermi level occurs, thus improving the sensor response of these materials [12]. Apart from the grain size reduction, a lot of other complex factors affect the sensor performance which, in turn, is determined by the reception and transduction function along with the fabrication procedure (thin or thick film, porosity, particle agglomeration, etc.) [17]. The selection of the functional material, the synthesis procedure, crystal size and shape, the addition of foreign elements with the role of sensitizers or conductivity modifiers are some of the factors influencing the sensor response. Understanding the mechanisms through which the sensor response is modified by each of these factors makes the semiconductor oxide suitable to be prepared with tunable physical–chemical characteristics, thus enabling the fabrication of sensor devices with specific functionality.

1.2 EXPERIMENTAL EVIDENCES

Among the above-mentioned materials, a case in point is tin dioxide, the most widely used material for gas sensing, by which in 1970 Figaro Engineering Inc. fabricated and commercialized the first metal oxide gas sensor device [18]. SnO_2 exhibits n-type semiconductor behavior due to lattice defects, in particular oxygen vacancies acting as electronic donor levels. Indeed, Samson and Fonstad experimentally determined the presence of two donor levels, $Ed_1 = 0.034$ and $Ed_2 = 0.145$ eV below the bottom of the conduction band [19]. Figure 1.2 shows the Arrhenius plot obtained by changing the temperature between 360 and 900 K at the heating rate of 3 K/min (A) and the height of the surface barrier potential versus temperature (B) of a SnO_2 thick-film. The direct determination of the height of the surface potential barrier at a fixed temperature is carried out using the method of temperature-stimulated conductance measurements, firstly described by Clifford and Tuma [20], according to which the conductance is measured as a function of time, after a change of temperature so fast that it is

possible to assume the constancy of the barrier while the conductance changes due to the variation of free carriers. Afterwards, conductance measurements were performed by changing the temperature between 300 and 900 K at the heating rate of 3 K/min. Now, through Morrison's equation [21], which factorizes the surface and bulk contributions, the heights of the potential barrier as a function of temperature can be calculated from the measured conductance values. Further discussions and explanations on this point can be found in [22,23].

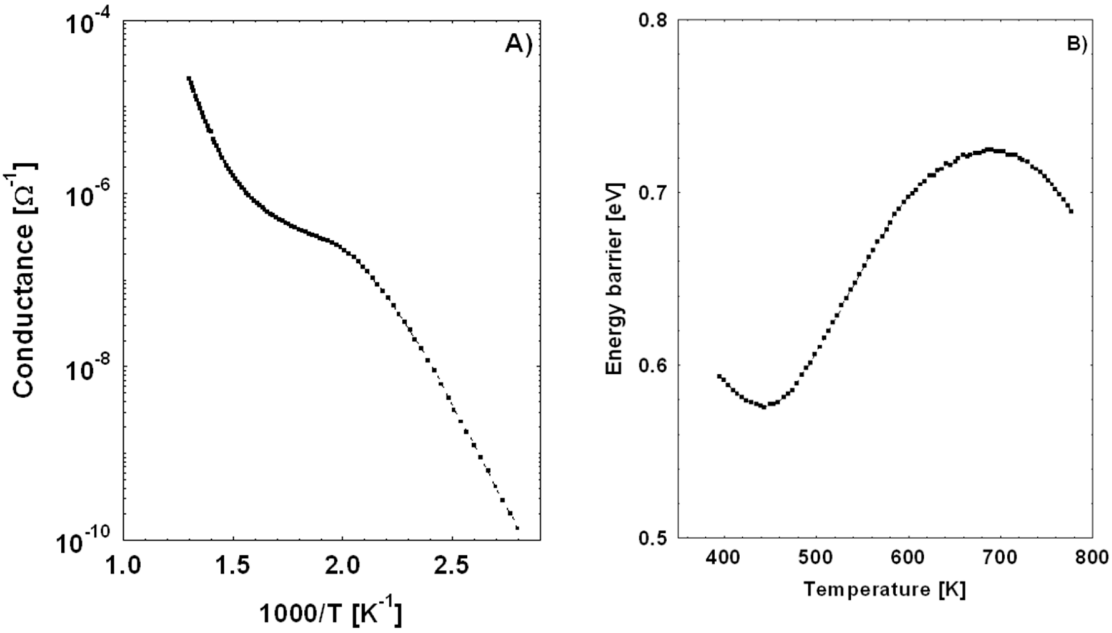

Fig. 1.2. Arrhenius plot (A) and energy barrier vs. temperature (B), for pure tin oxide films.

Different conductivity regions were observed, demonstrating the occurrence of different surface adsorption phenomena, in particular the O_2^- – O^- transformation, as experimentally proven by Chang through the correlation between electrical conductivity and EPR measurements [24]. The typical behaviour of the SnO_2 energy barrier versus temperature exhibits a minimum and a maximum corresponding to the increase of the depletion layer depth with temperature attributed to a negative surface charge accumulation, typically O^- ions. The ability of tin dioxide to sense either reducing agents at high temperature or oxidizing ones, like NO_2, at low temperature could be explained according to these characteristics. The interaction between the analyte and the surface of the semiconductor causes changes to the potential barrier height at the inter-granular contact and therefore to electrical conductance variations.

Passing to gas responses, Fig. 1.3 shows the SnO_2 energy barriers carried out in dry air and in 500 ppm of CO in dry air. Carbon monoxide strongly affects the surface barrier height, decreasing it at all temperatures, thus demonstrating an enormous capability for SnO_2 to sense CO within 200 – 400 °C. Indeed, it means that in the phenomenon just described a great amount of electrons participates to the detection process, thus promoting the gas response. Generally, whenever it has observed a very strong response to a reducing gas, it is also highlighted this trend: a growing reducing gas response with increasing the difference between the values of the two energy barriers measured as a function of temperature.

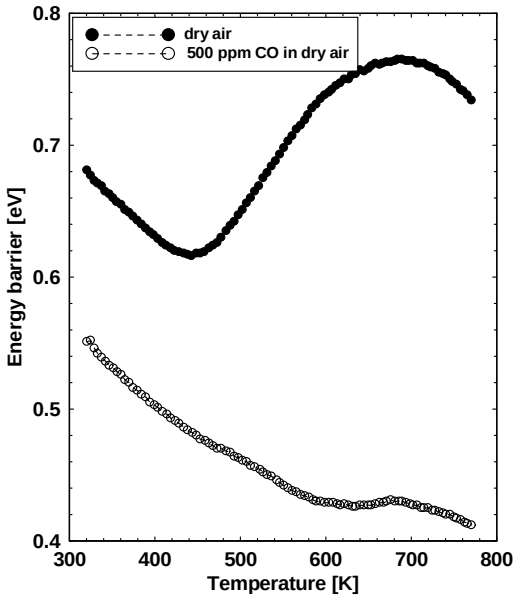

Fig. 1.3. Energy barrier for SnO_2 sample undergone to dry air (●) and to 500 ppm of CO in dry air (○).

As the first material extensively investigated in gas sensing, many studies have been performed to improve the sensing and selectivity properties of SnO_2, above all by adding small amounts of noble metals on the surface [25-29]. On this matter, in the paper of Batzill and Diebold the role of additives in gas sensing materials has been deeply reviewed [30].

As stated above, the grain size reduction at nanometric level is one of the main factors enhancing their detection properties decreasing the grain dimension to obtain a grain size smaller than the depletion layer [12,14,31,32]. Actually, in tin oxide thick film sensors is not usual to observe the grain size dependence of the response. Indeed, the firing at high temperature causes a grain coalescence to being the grain radius up to 20-30 nm. Because the depletion layer depth in tin oxide is smaller than 20 nm, to observe this phenomenon, the sensing layers must be deposited starting from very small powders (< 10

nm) and heated at moderate temperature (< 650 °C) [see next section]. Under these conditions, it was experimentally verified that the response to carbon monoxide is about twice when the grain size is about 10 nm with respect to that of a grain size of about 30 nm [33].

The second material to take into consideration for describing properties and behavior of metal oxide gas sensors is TiO_2. The major knowledge of titania as functional material come out from catalysis and photocatalysis [34-37]. In gas sensing field, titania was initially investigated as automotive exhaust sensor for the control of the air/fuel ratio and therefore to detect oxygen, using its ionic conductivity [38-40]. Only from the nineties, titania has been studied to detect atmospheric pollutants at moderate temperature (300-600 °C) [41]. Actually, titania is suitable to sense polluting gases in air, allowing good and stable responses, only if the grain dimension of the poly-crystalline material keeps at nanometric level. Indeed, differently from SnO_2, titanium dioxide, when heated, undergoes a phase transition from anatase into rutile, simultaneously resulting in very large grain coalescence [42,43]. The anatase phase can be stabilized through the addition of ions with valence 5^+ [44-46]. In particular Ta (10 at. %) allowed to hinder the transition to rutile up to 950 °C [44].

In spite of the excellent results in terms of anatase phase stabilization with the consequent maintenance of the grain dimension at nanometric size, the TiO_2-based gas sensors differ in gas sensing behaviour from SnO_2-based ones, being the latter much more reactive toward reducing gases.

Fig. 1.4 shows a comparison between the responses of samples of pure SnO_2 and pure TiO_2 (two sensors for each material, fired at 650 and 850 °C, respectively), to 100 ppm of CO in dry air at the working temperature of 450 °C. Two main observations can be made: i) sensing capability of SnO_2 is much higher than that of titanium dioxide; ii) unlike SnO_2, gas responses of titania sensors are strongly dependent on the grain size. Indeed, in SnO_2 sensors the firing at 850°C is accompanied by a modest grain coalescence, as mentioned above, while in TiO_2 sensors, the firing at temperatures higher than 750°C implies a crystalline phase transformation accompanied by an enormous grain coalescence, thus losing the sensing capability. TiO_2 strongly differ from SnO_2 also both for much smaller electrical conductivity and for the shape of the Arrhenius plot (see Fig. 1.5 A). Indeed, the sigma–shape caused in SnO_2 by the occurrence of surface reactions (in particular the O_2^- - O^- transformation in the 200 - 400 °C range) is not visible in TiO_2 because in this temperature range the donor states are not yet ionized.

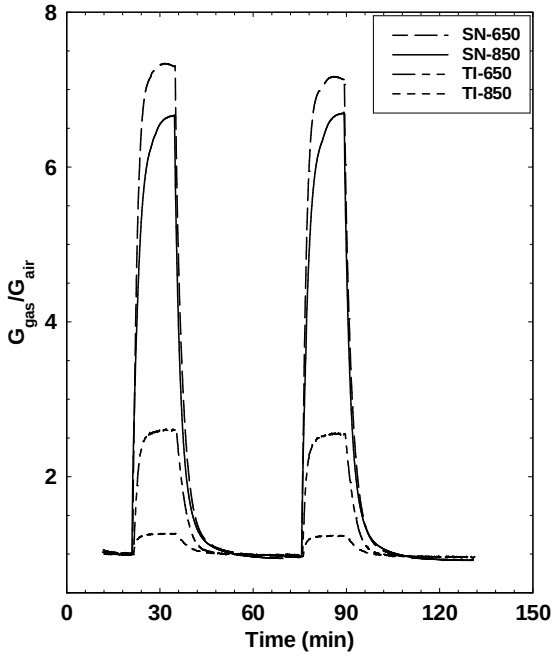

Fig. 1.4. Electrical responses to 100 ppm of CO (G_{gas}/G_{air}) for two of samples of pure SnO_2 and pure TiO_2 (two sensors for each material, fired at 650 and 850 °C, respectively) measured at 450°C.

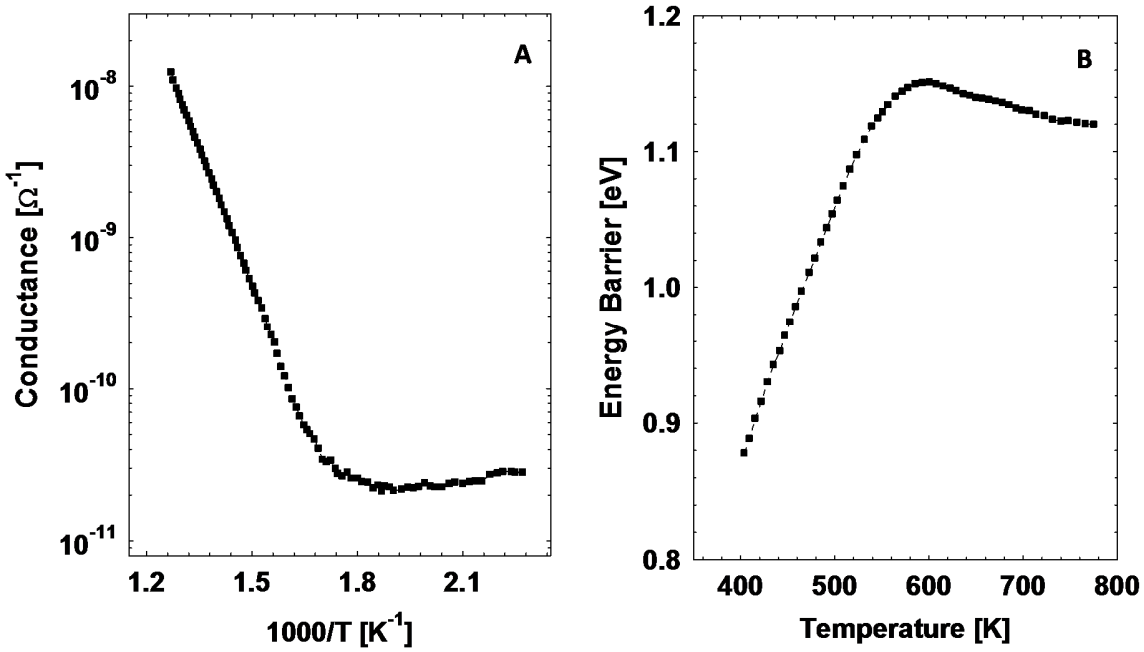

Fig. 1.5. Arrhenius plot for conductance (A) and energy barrier vs. temperature (B) for pure titania films

In fact, the n-type behaviour, similarly to SnO_2, depends to donor-like stoichiometric defects, generally ascribed to oxygen vacancies, but with energetic positions in TiO_2 much more deep inside the band gap

with respect to SnO_2 [19,47]. Actually some authors assign donor levels, 0.8 eV deep, at Ti_3^+ ions rather than at oxygen vacancies [37,48]. Moreover titania films feature energy barriers vs temperature much higher than SnO_2, where almost three activation energies are exhibited, differently from TiO_2, in which only two regions of barrier are present (see Fig. 1.5 B). Both effects (shape of the barrier and intensity of gas response) are strongly related to the density of surface states, which, in turn, depends on the dimensions of the nanograins, as illustrated in the next section.

The comparison between SnO_2 and TiO_2 comes naturally because they exhibit the same rutile crystalline structure, space group $P4_2/mnm$, easily giving rise to a solid solution with chemical-physical properties varying with the Ti-Sn molar ratio [49,50].

Actually, the SnO_2-TiO_2 mixed oxide is a very interesting material for thick-film gas sensors and its synthesis and investigation (as $Ti_xSn_{1-x}SnO_2$, $0 \leq x \leq 1$) allowed to discover a completely different phenomenon occurring during the sensing process in SnO_2-like materials compared with what happens in TiO_2-like ones [51]. Indeed, through FTIR analysis under CO atmosphere, for the materials with $x < 0.2$, as already observed in pure SnO_2, a very broad absorption in the MIR region, related to the photoionization of $VO^{\cdot}$, occurred, while samples with $0.3 \leq x \leq 1$ exhibited a completely different phenomenon consisting in an erosion of the absorption edge related to the skeletal M–O vibration modes related to the skeletal vibration modes is observable, indicating a loss of reticular oxygen at surface during the reducing treatment. This difference of behavior, together with the definition of the phenomenon of the unpinning of the Fermi level, contributed to understand the electrical differences between SnO_2 and TiO_2. In [52], it is reported the different behavior of the samples as a result of the contribution of two detection mechanisms: i) the chemical reaction happens between the analyte and ionosorbed oxygen atoms causing an electron transfer from the surface to the bulk and vice versa in turn causing a barrier modification; ii) the oxygen atoms involved in the detection mechanism are surface lattice oxygen atoms which bond electrons that do not participate to the development of the spatial charge region and therefore of the intergranular barrier. Thus, it is reasonable that in the materials with $x < 0.3$, the prevalent gas detection mechanism is the usual one (through barrier modification), whilst for $x \geq 0.3$, it mainly happens through bond electrons which, after the reaction, enter CB without affecting the barrier.

In summary, with regard to the electrical properties of the various solid solutions obtained by varying the Ti molar ratio, all examined samples with $0.1 \leq x \leq 0.9$ exhibited good sensing performance, even if they exhibited crystalline rutile structure. However, it must be noted that these materials do not undergo to phase transformation, exhibiting rutile phase as synthesized. For this reason, the grains only

moderately undergo coalescence when heated at high temperature. In Fig. 1.6, the response of the films to 50 ppm of CO (performed at the working temperature of 500°C) has been plotted together with the crystallite size of the corresponding powders heated at 1050°C,both as a function of Ti molar ratio. For both curves the best fit is a quadratic function with a correlation coefficient $r^2 = 0.847$ for CO response, while r^2 for crystallite size was 0.958.

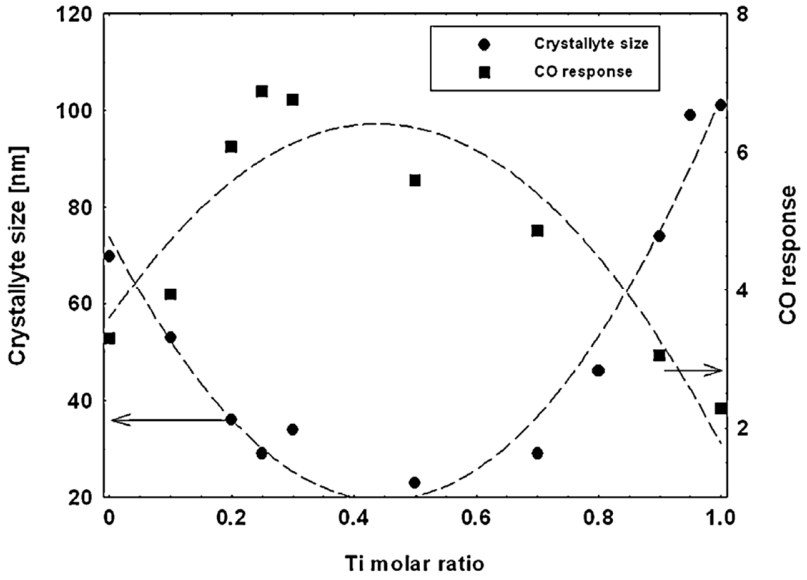

Fig. 1.6. Response to 50 ppm of CO (performed at the working temperature of 500◦C)plotted together with the crystallite size, both as a function of Ti molar ratio.

Both phenomena are strongly dependent on the Ti molar ratio, but in the case of CO response with a greater error. Indeed, in this case two phenomena concur to the response: the content of titanium in the solid solution, but also the grain size, respect to which the dependence is linear. Looking at the CO response vs. Ti molar ratio, the material with x = 0.25 offers the highest response, being probably the material, in which the contribution to the sensing process of both mechanisms is optimized.

Other semiconductor oxides are functional materials common in gas sensing, such as WO_3, ZnO, In_2O_3, etc., their electrical properties remaining in the range in which the Schottky barrier model for conductivity is accepted. Among them, ZnO has been pioneering material in gas sensing. Afterward it was abandoned, but recently it has met the interest of researchers as witnessed by an exponential growth of publications. Indeed, zinc oxide is a very attractive multifunctional material both for its great variety of properties and for the possibility to synthesize it in an enormous amount of nanostructures. In this work, an important part of the research activity has been devoted to the preparation and characterization

of ZnO nanostructures with a wide variety of morphologies such as nanoparticles, nanowires, nanobelts, nanorods, nanoflowers, etc., demonstrating that, in addition to the role of grain size, also the morphology can modify the electronic properties of the material, thereby having an effect onto the sensing properties.

1.3 RESPONSE MODELING

As stated above, n-type extrinsic semiconductors are characterized by the presence of free electrons in the conduction band mainly due to lattice defects, such as oxygen vacancies, generated by reducing processes during the synthesis of the material. The mechanism of conduction is controlled by electron flow through a huge series of intergranular point contacts. At these contacts a surface barrier originates in the presence of surface states, whose amount depends both on the chemical reactions with detecting gases and on the physical intrinsic characteristics of the material.

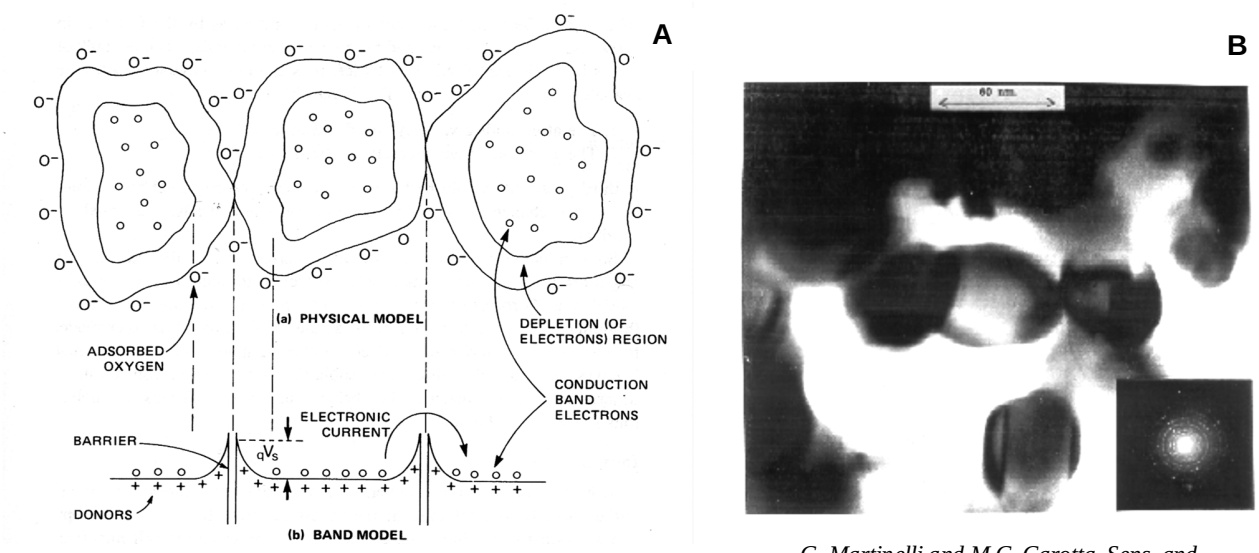

Madou, Morrison, Chemical sensing with solid state devices, Academic Press Inc, Sanm Diego, CA, 1989, p.37

G. Martinelli and M.C. Carotta, Sens. and Actuators B 23 (1995) 157-161.

Fig. 1.7. Physical and band model for three grains of semiconductor to show how the barrier develops (A) and a TEM image of three grains of a SnO_2 thick film (B).

The usual form of the Shottky barrier *eVs* and the corresponding potential *V*, is:

$$eV_s = W_{ss} - \chi_s; \qquad V = (W_{ss} - \chi_s)/e$$

e being the absolute value of the electron charge. W_{ss} represents the work function of the surface layer (environmental work function) and χ_s is the electron affinity of the semiconductor.

Considering the hypotheses of the depletion approximation (DA) − applicable if the grains are much larger than the depletion layer width − : i) the total charge density equal to qN_d all over the depleted region of thickness Λ and zero elsewhere: ii) the potential $\Phi(r)$ equal to zero at the centre of the grain, as well as the electric field, and solving the Poisson equation in planar geometry:

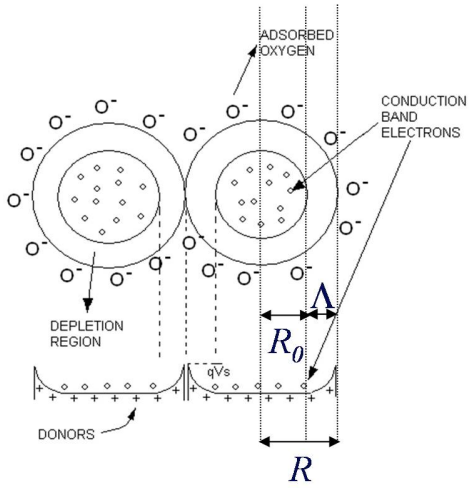

$$\frac{d^2\Phi}{dx^2} = -\frac{\rho}{\varepsilon}$$

the Schottky relation is:

$$V_s = \frac{eN_d\Lambda^2}{2\varepsilon_0\varepsilon_r}$$

where N_d is the density of donors and $\varepsilon(=\varepsilon_0\varepsilon_r)$ the dielectric constant. The planar model, however, fails when the grain size is comparable to the extension of the depleted region Λ. In this case, indeed, it is necessary to solve the Poisson equation in spherical symmetry, since the curvature of the grain plays a relevant role. Applying the suitable boundary conditions (potential and electric field equal to zero at the centre of the grain) and imposing the grain charge neutrality, new relations for Vs and the surface state density Ns can be obtained:

$$\begin{cases} \frac{1}{r}\frac{d^2}{dr^2}(r\Phi(r)) = -\frac{\rho(r)}{\varepsilon} \\ -\left.\frac{d\Phi(r)}{dr}\right|_{r=R-\Lambda} = 0 \\ \Phi(r)\big|_{r=R-\Lambda} = 0 \\ eN_d\left(\frac{4}{3}\pi R^3 - \frac{4}{3}\pi R_o^3\right) = eN_s 4\pi R^2 \end{cases}$$

$$\begin{cases} V_s = \frac{eN_d}{2\varepsilon}\Lambda^2\left(1-\frac{2\Lambda}{3R}\right) & (1) \\ N_t = \Lambda N_d\left(1-\frac{\Lambda}{R}+\frac{\Lambda^2}{3R^2}\right) & (2) \end{cases}$$

Solving Eq. (2) by setting the experimental values for ε, N_d and V_s, for particles ranging from 50 to 150 nm, it turned out that for SnO_2, N_S is almost constant. On the contrary, for TiO_2 N_S resulted in strongly decreasing as the grain radius decreased below 60 nm (see Fig. 1.8).

The traditional Schottky relation is obtained from equation 2 as Λ/R tends to zero. On the opposite limit, when $R \cong \Lambda$, the corrective terms due to curvature, become relevant.

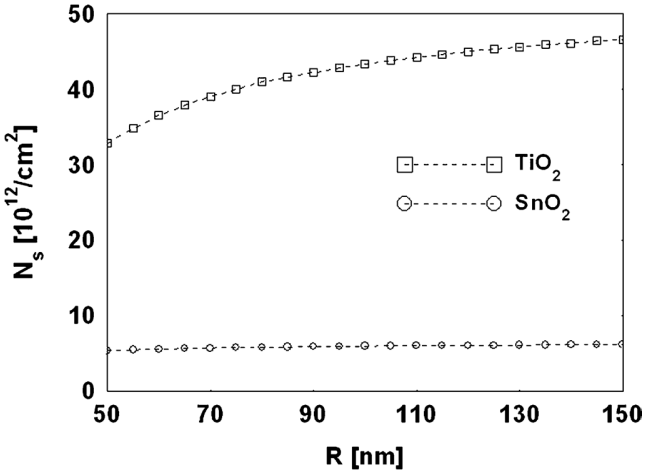

Fig. 1.8. Calculated density of charged surface states N_S as a function of grain radius for SnO_2 and TiO_2.

This situation leads to a so-called unpinning of the Fermi level, allowing good gas responses, because the Fermi level is not forced to be at a distance from the minimum of conduction band equal to the neutral level of the surface states [53]. Therefore, in the considered range,SnO_2 cannot be considered as nanostructured, on the contrary for TiO_2.

The DA, however, fails also when the free charge density current cannot be neglected. The Poisson equation must be formulated considering the complete charge density $\rho(r)$, being the second term the contribution of the mobile charge carrier at nonzero temperature:

$$\rho(r) = \frac{eN_d}{\varepsilon} - \frac{eN_d}{\varepsilon} e^{e\Phi(r)/k_B T} \qquad (3)$$

The charge density used in the DA must be achievable from this expression, in which the zero of energy (and potential) is at the bottom of the conduction band. The problem is that, in the case of powdered or polycrystalline semiconductors, the bulk can be reached only if the grain is sufficiently large. The DA

assumes, instead, that the zero-potential is always attained, independently of the grain size (see the boundary conditions for DA). This is the reason for inapplicability of the DA to small grains, for which the potential does not necessarily vanish even on the center.

The Poisson equation, considered the complete charge density, is:

$$\frac{1}{r}\frac{d^2}{dr^2}\left[r\Phi(r)\right] = -\frac{eN_d}{\varepsilon} + \frac{eN_d}{\varepsilon}e^{e\Phi(r)/k_BT}$$

Here the boundary conditions are slightly different from those for the DA. Because of the spherical symmetry, the condition on the field is that it vanishes on the center of the grain. For what concerns the condition on the potential, we set the zero at the bottom of the conduction band on the center of a sufficiently large grain, according to the literature. The condition of grain charge neutrality is written through the Gauss theorem.

$$\Phi(r)\big|_{r=R} = -V_b$$

$$-\frac{d}{dr}\Phi(r)\big|_{r=0} = 0$$

$$-\frac{d}{dr}\Phi(r)\big|_{r=R} = \frac{eN_t}{\varepsilon}$$

Since $\Phi(r) \leq 0$, when $\Phi(r)$ is of the order of k_BT, the last term could be very significant. This equation doesn't have an analytical solution and the approximation for low values of $\Phi(r)$ leads to the Debye length

$$\lambda_D = \sqrt{\varepsilon k_B T / e^2 N_d}$$

Therefore, the complete extinction length of the potential is given by $\Xi = \Lambda + \lambda_D$. Provided that the grain radius is sufficiently large, the DA is a good approximation when Λ is significantly larger than λ_D. When, instead, the surface potential is small and the slope is high, the charge density used for DA is inadequate even if the radius of the grain is greater than Ξ; this is precisely the case experimented for WO_3 oxide, for which a weak dependence of conductance versus temperature reported and a low energy barrier has been measured. In this case, the depletion layer approximation doesn't work because the condition $eV_S >> k_T$ is not anymore satisfied.

Going back to the case of SnO_2 and TiO_2, using the spherical model based on the complete charge density, the difference between the two materials is evident.

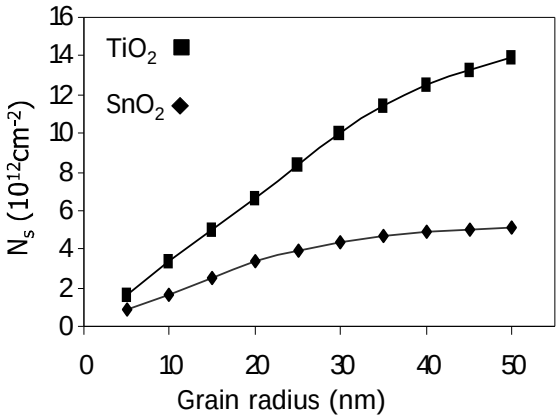

Fig. 1.9. Calculated density of charged surface states N_S as a function of grain radius for SnO_2 and TiO_2 in the case of numerical solution of the Poisson equation with the complete charge density.

The diagram of Fig.1.9 highlights the dependence of the density of the surface states on the grain radius both for SnO_2 and TiO_2, being the numerical parameters the same used in the case of depletion approximation. In SnO_2, the decreasing of the surface states occurs below 20 nm, while for TiO_2 it is already noticeable below 50 nm. Thereby, the two materials can be considered as nanostructured (from the point of view of the electrical conductivity) below two different critical values.

REFERENCES

[1] Jon s. Wilson (Ed.), Sensor technology Handbook, Elsevier Inc., 2005.

[2] Kyounghoon Lee, Dae-Hyun Baek, Han-Il Jung and Jongbaeg Kim, Miniaturized VOC Detectors for Monitoring Indoor Air Quality, in C.-M. Kyung (ed.), Smart Sensors for Health and Environment Monitoring, KAIST Research Series, DOI 10.1007/978-94-017-9981-2_7.

[3] Inkyu Park, Daejong Yang and Kyungnam Kang, Microfabricated and Nanoengineered Chemical Sensors for Air Quality Monitoring System, in C.-M. Kyung (ed.), Smart Sensors for Health and Environment Monitoring, KAIST Research Series, DOI 10.1007/978-94-017-9981-2_6.

[4] S. Li, A. Simonian, and B. A. Chin, The Electrochemical Society Interface • Winter 2010

[5] M. Righettoni, A. Amann and S. E. Pratsinis, Breath analysis by nanostructured metal oxides as chemo-resistive gas sensors, Materials Today, Volume 18, Number 3, April 2015.

[6] Il-Doo Kim, Seon-Jin Choi, Sang-Joon Kim and Ji-Su Jang, Exhaled Breath Sensors, in C.-M. Kyung (ed.), Smart Sensors for Health and Environment Monitoring, KAIST Research Series, DOI 10.1007/978-94-017-9981-2_2.

[7] B P J de Lacy Costello, R J Ewen and N M Ratcliffe, A sensor system for monitoring the simple gases hydrogen, carbon monoxide, hydrogen sulfide, ammonia and ethanol in exhaled breath, J. Breath Res. 2 (2008) 037011.

[8] A. Ryzhikov, J. Jonca, M. Kahn, K. Fajerwerg, B. Chaudret, A. Chapelle, P. Menini, C.H. Shim, A. Gaudon, P. Fau, Organometallic synthesis of ZnO nanoparticles for gas sensing: towards selectivity through nanoparticles morphology, J. Nanopart. Res. 17(7) (2015).

[9] D. Lutic, M. Sanati and A. Lloyd Spetz (2007), Gas Sensors, in Rodríguez J A and Fernandez García M, Synthesis, Properties and Applications of Oxide Nanomaterials, New York, Wiley, 411-450.

[10] J.G. Lu, P. Chang, Z. Fan, Quasi-one-dimensional metal oxide materials – synthesis, properties and applications, Materials Science and Engineering R 52 (2006)49–91.

[11] Yu-Feng Sun, Shao-Bo Liu, Fan-Li Meng, Jin-Yun Liu, Zhen Jin, Ling-Tao Kong and Jin-Huai Liu, Metal Oxide Nanostructures and Their Gas Sensing Properties: A Review, Sensors 2012, 12, 2610-2631; doi:10.3390/s120302610.

[12] C. Malagù, V. Guidi, M.C. Carotta, G. Martinelli, Unpinning of Fermi level innanocrystalline semiconductors, Appl. Phys. Lett. 84 (2004) 4158–4160.

[13] M.C. Carotta, M. Benetti, E. Ferrari, A.Giberti, C. Malagù, M. Nagliati, B. Vendemiati and G. Martinelli, Basic interpretation of thick film gas sensors for atmospheric application, Sens. Actuators B, 126 (2007) 672-677.

[14] C. Xu, J. Tamaki, N. Miura, N. Yamazoe, Grain size effects on gas sensitivity of porous SnO_2-based elements, Sens. Actuators B 3 (1991) 147–155.

[15] X.-J. Huang, Y.-K. Choi, Chemical sensors based on nanostructured materials, Sens. Actuators B 122 (2007) 659–671.

[16] K.J. Choi, H.W. Jang, One-dimensional oxide nanostructures as gas-sensing materials: review and issues, Sensors 10 (2010) 4083–4099.

[17] N. Yamazoe, K. Shimanoe, Receptor function and response of semiconductorgas sensor, J. Sens. (2009), 875704

[18] N. Taguchi, UK Patent, 1280809 (1970).

[19] S. Samson, C.G. Fonstad, Defect structure and electronic donor levels in stannic oxide crystals, J. Appl. Phys. 44 (1973) 4618–4621.

[20] P.K. Clifford, D.T. Tuma, Characteristics of semiconductor gas sensors – II. Transient response to temperature change, Sens. Actuators 3 (83) (1982) 255–282.

[21] S.R. Morrison, Semiconductor gas sensors, Sens. Actuators 2 (1982) 329–341.

[22] V. Lantto, P. Romppainen, S. Leppävuori, A study of the temperature dependence of the barrier energy in porous tin dioxide, Sens. Actuators 14 (1988) 149–163.

[23] M.C. Carotta, C. Dallara, G. Martinelli, L. Passari, A. Camanzi, CH_4 thick-film gas sensors: characterization method and theoretical explanation, Sens. Actuators B 3 (1991) 191–196.

[24] S.C. Chang, Oxygen chemisorption on tin oxide: correlation between electrical conductivity and EPR measurements, J. Vac. Sci. Technol. 17 (1980) 366.

[25] N. Yamazoe, Y. Kurokawa, T. Seiyama, Effects of additives on semiconductor gas sensors, Sensors and Actuators 4 (1983) 283 – 289.

[26] K.D. Schierbaum, U.K. Kirner, J.F. Geiger, W. Göpel, Schottky-barrier and conductivity gas sensors based upon Pd/SnO_2 and Pt/SnO_2, Sensors and Actuators B 4 (1991) 87

[27] N. Yamazoe, New approaches for improving semiconductor gas sensors, Sensors and Actuators B 5 (1991) 7–19.

[28] W. Fliegel, G. Behr, J. Werner, G. Krabbes, Preparation, development of microstructure, electrical and gas-sensitive properties of pure and doped SnO_2 powders, Sensors and Actuators B 18–19 (1994) 474–477.

[29] A. Cabot, A. Vilà, J.R. Morante, Analysis of the catalytic activity and electrical characteristics of different modified SnO_2 layers for gas sensors, Sensors and Actuators B 84 (2002) 12–20.

[30] Matthias Batzill, Ulrike Diebold, The surface and materials science of tin oxide, Progress in Surface Science 79 (2005) 47–154.

[31] Noboru Yamazoe, New approaches for improving semiconductor gas sensors, Sensors and Actuators B 5 (1991) 7-19.

[32] Gong Zhang, Meilin Liu, Effect of particle size and dopant on properties of SnO2-based gas sensors, Sensors and Actuators B 69 (2000) 144–152.

[33] C. Malagù, M.C. Carotta, H. Fissan, V. Guidi, M.K. Kennedy, F.E. Kruis, G. Martinelli, T.G.G. Maffeis, G.T. Owen, S.P. Wilks, Evidence of bandbending flattening in 10 nm polycrystalline SnO_2, Sensors and Actuators B, 103 (2004) 50-54.

[34] S. Matsuda and A. Kato, Titanium oxide based catalysts - A review, Applied Catalysis 8 (1983) 149-165.

[35] Amy L. Linsebigler, Guangquan Lu, and John T. Yates, Jr., Photocatalysis on TiO_2 Surfaces: Principles, Mechanisms, and Selected Results, Chemical Reviews 95 (1995) 735-758.

[36] Yaron Paz, Application of TiO_2 photocatalysis for air treatment: Patents' overview, Applied Catalysis B: Environmental 99 (2010) 448–460.

[37] Ulrike Diebold, The surface science of titanium dioxide, Surface Science Reports 48 (2003) 53-229.

[38] T.Y. Tien, H.L. Stagler, E.F. Gibbons, P.J. Zacmanidis, TiO_2 as an air-to-fuel ratio sensor for automobile exhausts, Am. Ceram. Soc. Bull. 54 (1975) 280–282.

[39] A. Takami, Development of titania heated exhaust-gas oxygen sensor, Ceram. Bull. 67 (12) (1988) 1956– 1960.

[40] M.K. Akhtar, S.E. Pratsinis, S.V.R. Mastrangelo, Dopants in vapour phase synthesis of titania powders, J. Am. Ceram. Soc. 75 (1992) 3408–3416.

[41] H. Tang, K. Prasad, R. Sanjines, F. Levy, TiO_2 anatase thin films as gas sensors. Sensors and Actuators B, 26-27 (1995) 71–75.

[42] R.K. Sharma, M.C. Bhatnagar, G.L. Sharma, Effect of Nb metal TiO_2 oxygen gas sensor, Applied Surface Science 92 (1996) 647-650.

[43] M.C. Carotta, M. Ferroni, D. Gnani, V. Guidi, M. Merli, G. Martinelli, M.C. Casale, M. Notaro, Nanostructured pure and Nb-doped TiO_2 as thick film gas sensors for environmental monitoring, Sensors and Actuators B 58 (1999) 310–317.

[44] E. Traversa, M.L. Di Vona, S. Licoccia, M. Sacerdoti, M.C. Carotta, L. Crema, G. Martinelli, Sol–gel processed TiO_2-based nano-sized powders for use in thick film gas sensors for atmospheric pollutant monitoring, J. Sol–Gel Sci. Technol. 22 (2001) 167–179.

[45] A.M. Ruiz, G. Dezanneau, J. Arbiol, A. Cornet, and J.R. Morante, Insights into the Structural and Chemical Modifications of Nb Additive on TiO_2 Nanoparticles, Chem. Mater.16 (2004) 862-871.

[46] M. Sacerdoti, M.C. Dalconi, M.C. Carotta, B. Cavicchi, M. Ferroni, S. Colonna, M.L. Di Vona, XAS investigation of tantalum and niobium in nanostructured TiO_2 anatase, J. Solid State Chem. 177 (2004) 1781–1788.

[47] S. Munnix, M. Schmeits, Origin of defect states on the surface of TiO_2, Physical Review B 31 (1985) 3369-3371.

[48] W. Göpel, U. Kirner, H.D. Wiemhofer, Surface and bulk properties of TiO_2 in relation to sensor applications, Solid State Ionics 28-30 (1988) 1423-1430.

[49] M. Park, T.E. Mitchell, H. Heuer, Subsolidus equilibria in the SnO_2–TiO_2system,J. Am. Ceram. Soc. 58 (1) (1975) 43–47.

[50] T.C. Yuan, A.V. Virkar, Kinetics of spinodal decomposition in the TiO_2–SnO_2system: the effect of aliovalent dopants, J. Am. Ceram. Soc. 71 (1) (1988) 12–21.

[51] M.C. Carotta, S. Gherardi, V. Guidi, C. Malagù, G. Martinelli, B. Vendemiati, M. Sacerdoti, G. Ghiotti, S. Morandi, Electrical and spectroscopic properties of $Ti_{0.2}Sn_{0.8}O_2$ solid solution for gas sensing, Thin Solid Films 517 (2009) 6176–6183.

[52] M.C. Carotta, A. Fioravanti, S. Gherardi, G. Ghiotti, C. Malagù, S. Morandi, and M. Sacerdoti, (Ti, Sn) binary oxides as functional materials for gas sensing, Sensors and Actuators B 194 (2014) 195-205.

[53] J. Bardeen, Surface states and rectification at a metal semi-conductor contact, Phys. Rev. 71 (1947) 717.

CHAPTER 2

THICK FILM PREPARATION AND CHARACTERIZATION

2.1 INTRODUCTION

Thick film deposition normally is carried out through screen-printing, which is one of the oldest forms of graphic art reproduction. Screen-printing is a simple and automated manufacturing technique which allows the production of low-cost and robust chemical sensors with good reproducibility provided that the functional materials and all steps of the process are well controlled.

Thick film technology is known for hybrid circuits production, finding various applications thanks to features such compactness, robustness and, with respect to other technologies, relatively low cost. This technology is today largely applied also in the sensor field both for passive electronic components, like conductors, resistors and dielectric materials, and as primary sensors technology; among these, temperature, radiation, magnetic field, mechanical quantities and chemical sensors, the latter being the subject of this research [1,2]. The mass-production capacity (up to some hundreds of sensors at a time) at low cost with respect to other technologies, combined with devices reliability in harsh operating conditions, makes thick film planar technology particularly suitable for sensors production. Moreover, insofar as our experience is concerned, one of the main advantages of screen-printing technology for production of sensing layers is that the material preparation and film deposition can be optimized as separately. In the following, the methods to prepare and characterize the functional materials, the screen-printing deposition technique and finally the method to electrically characterize the sensing layers will be described.

2.2 PREPARATION AND CHARACTERIZATION OF THE FUNCTIONAL MATERIALS

The major requirement in developing semiconducting metal oxides for thick-film gas sensing devices is related to the control of parameters affecting the electrical properties [3], and in particular the sensitivity, the selectivity or cross sensitivity, meaning that the magnitude of the response to the target

gas is affected by the contemporary presence of other gases, and finally the electrical stability. Over the years, a lot of studies have been indeed addressed to improve the sensing and selectivity properties of chemoresistive gas sensors, while probably not giving the same importance to repeatability. However, thick film gas sensors, among various types of metal oxide gas sensors, are surely the most reliable provided that the base materials are prepared with suitable structural and morphological characteristics. This particular feature, illustrated for a SnO_2 based sensor, is shown in Fig. 2.1, in which the carbon monoxide concentration was alternatingly changed between 5 and 40 ppm.

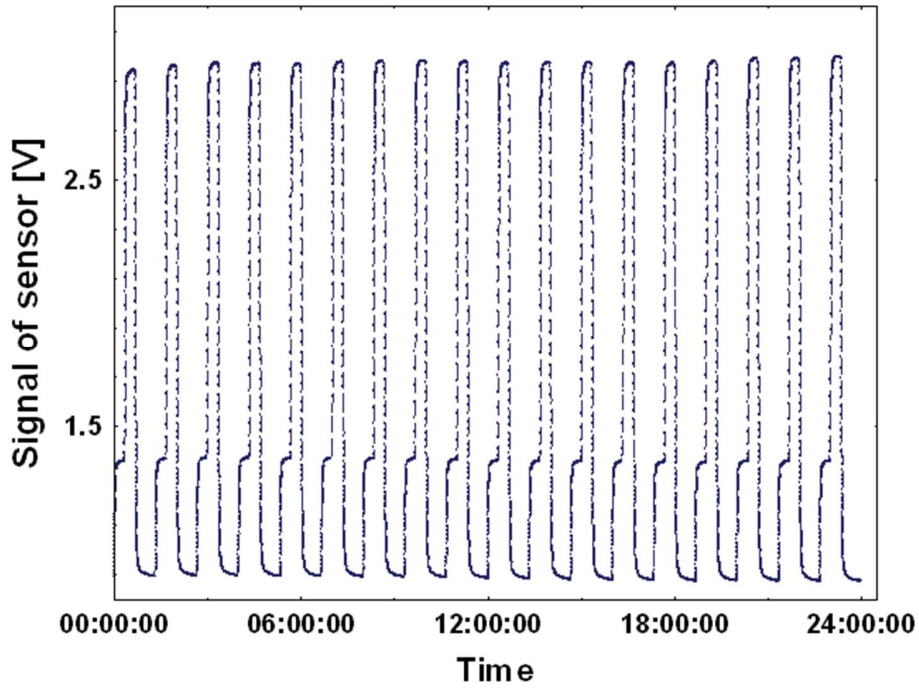

Fig. 2.1. Alternate response of a SnO_2-based thick film sensor to 5 and 40 ppm CO, the duration of a whole response is 1h, the duty cycle is 50%.

Thereby, the key problem of the preparation of a thick film gas sensor is the synthesis of engineered nanopowders constituting the functional materials. The chemistry is the turning point in powder-processing to obtain sensing layers with reproducible morphology (porosity, surface geometry, size of the necks,...) which take part to gas response and transduction phenomena.

Special attention is devoted to development of nanopowders with tailored characteristics via synthetic liquid-solid transformations performed under mild conditions, also called *wet methods*. As for any study concerning nanopowder synthesis, an accurate morphological, compositional and structural characterization of achieved products plays a very important role. Such investigations assist the

synthesis with feedback information toward the realization of material with optimal feature for gas sensing.

2.2.1 Synthesis methodology

Sol-gel methodology is a successful application of colloid science in ceramics development; it has been also chosen for its versatility to add dopants to main network of the oxide precursor. Moreover, it is suitable to prepare solid-solutions with good chemical homogeneity (i.e. non-random distribution of cations in inorganic network to be proved by further structural analyses) achieved by mixing colloidal components at low reaction temperature (T = 25-50 °C).

Two kinds of sol-gel methods can be applied: the first route involves inorganic metal salts (chlorides or nitrates) and the second one metal organic compounds, with general formula M(OR)x (R=alkyl group). Fundamental steps are hydrolysis of the starting materials and further condensation which proceeds by olation (M-(OH)-M bonds) or oxolation (M-O-M bonds) depending on the charge density in the involved species, the metal cations determining and driving the condensation reactions.

In this work, examples of the first route are $LaFeO_3$, WO_3 and ZnO powders preparation, while examples of the second route are SnO_2, TiO_2, $Ti_xSn_{1-x}O_2$ ($0 \leq x \leq 1$), $Sn_xW_{1-x}O_2$ with x = 0.1, 0.2 or 0.3 and $(Ti,Ta,V)O_2$ solid solution.

In Fig. 2.2, a general scheme of a *wet chemistry* process suitable to synthesize nanostructured semiconductor oxides to use as functional materials for gas sensing is reported.

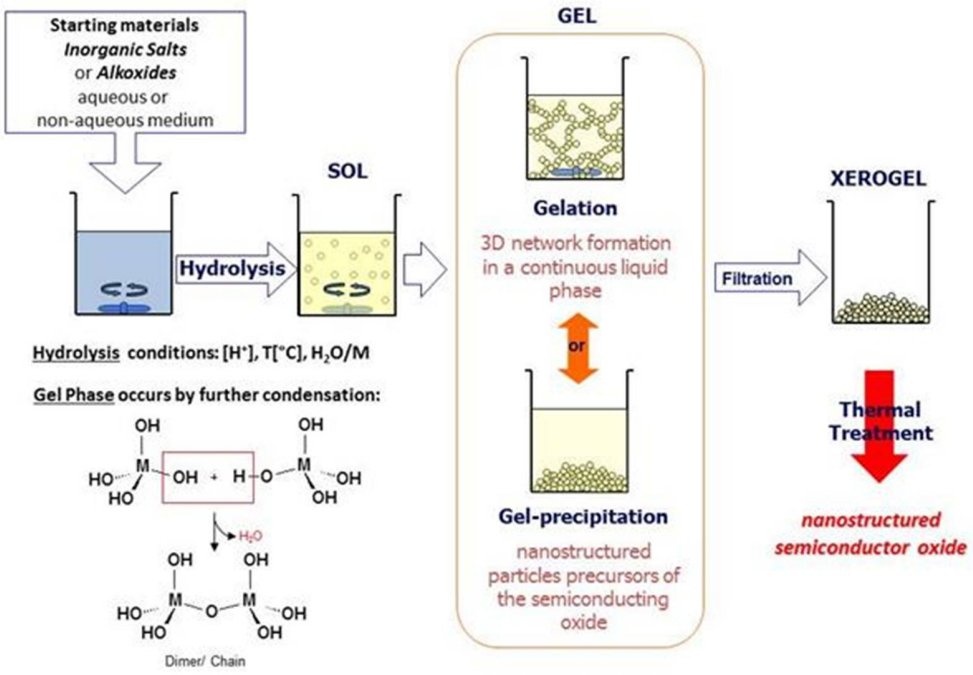

Fig. 2.2. General scheme of a "wet chemistry" process for the synthesis of semiconducting oxide powders

2.2.2 Characterization of the functional materials

X-ray diffraction - Diffraction occurs when the e-m radiation is scattered by a periodic array with long-range order, producing constructive interference at specific angles. The general condition to have diffraction is that the wavelength of the incident radiation must be similar to distance of at least two sources of diffracted waves.

X-ray diffraction (XRD) is based on the coherent elastic scattering of X-rays due to their interaction with the electrons of the material producing interference patterns. In particular, the atoms in a crystal are arranged in a periodic array and their distance is comparable to the wavelength of X-rays.

The most usual description of X-ray diffraction is known as Bragg's model [4]. The phenomenon is described as the selective reflection of monochromatic radiation due to the presence of crystallographic atomic planes, as shown in Fig. 2.3.

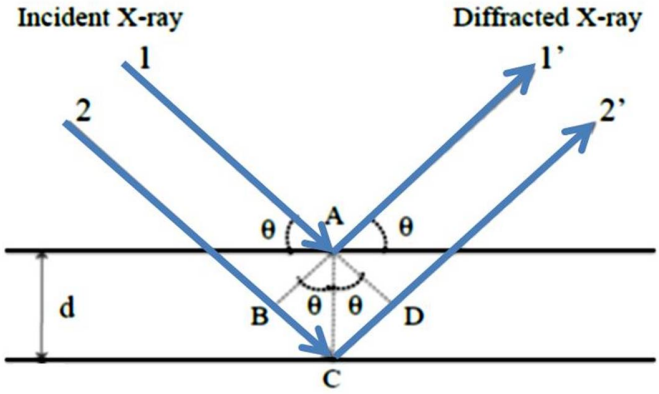

Fig. 2.3. Bragg's law diagram.

The condition for constructive interference of an X-ray photon scattered from parallel atomic planes is described by Bragg's equation:

$$2d_{hkl}sen\theta = n\lambda$$

where λ is the wavelength of the incident beam, d_{hkl} is the spacing between atomic planes that generate the reflection (*hkl* are Miller's indices for the single reflection), θ is the incident angle between the X-ray beam and the lattice plane and *n* represents the diffraction order.

During diffraction measurements the analyzed sample (thin film, powder or mono-crystal) is irradiated with a collimated monochromatic X-ray beam; the diffracted rays from the sample are then collected through a detector. The diffraction signal can be taken at different incident angles depending on the geometry adopted between source-sample-detector.

In this work, XRD analyses were performed using a Philips PW 1830 vertical powder diffractometer with Bregg–Brentano geometry (Cu Kα radiation, 40 kV, 30 mA) provided with a graphite monochromator along the diffracted beam. Diffraction patterns were collected over the range 10–120° (2θ) with steps of 0.02° and 10 s of dwell time.

The XRD pattern contains all the structural information of a crystalline sample (space group) deducible from the angular position, the intensity and the shape of peaks. The angular position is used to determine the inter-planar distances (d_{hkl}) and the crystallographic cell parameters, so to identify the crystalline phase univocally. The intensity of the peaks depends on the chemical composition of the examined material. The peak shape contains information about the degree of crystallinity and the strain of the sample. In general, the width of a peak is inversely proportional to the average size of crystallites along

the direction normal to the plane *hkl* which gives rise to that specific reflection [5]. The crystallites size can be estimated by using Scherrer's equation, as follows:

$$L = \frac{K\lambda}{\beta_{hkl} cos\theta}$$

where β_{hkl} is the full width at half maximum (FWHM) of the peak and *K* is a constant which depends on the shape of the crystallite and whose value ranges from 0.7 to 1.4.
The unit cell parameters of samples, studied in this work, were estimated through the program for Rietveld analysis (structure profile refinement) FullProf (release 2011) [6], while the crystallite size was estimated, according to Scherrer's formula setting the constant K at 0.9.

Scanning Electron Microscopy, SEM - Scanning Electron Microscopy (SEM), provides information on the texture and morphology of the materials' surface (bulk surfaces, powders or films) [7-8]. The resolution of this technique is of the order of nanometers and, when coupled with an X-rays collecting probe, allows a chemical analysis of the material's local composition. In general, a scanning electron microscope consist of an electronic source, a system of electromagnetic lenses to focus the electrons onto the sample, a vacuum system, different detectors and a computer to yield imaging and to manage the instrument. When the electron beam interacts with a material, different types of signal (electrons and X-rays) are generated (scheme in Fig. 2.4) and the image of the sample surface is reconstructed by the electronics that receive the out-coming signals from the different the detectors.

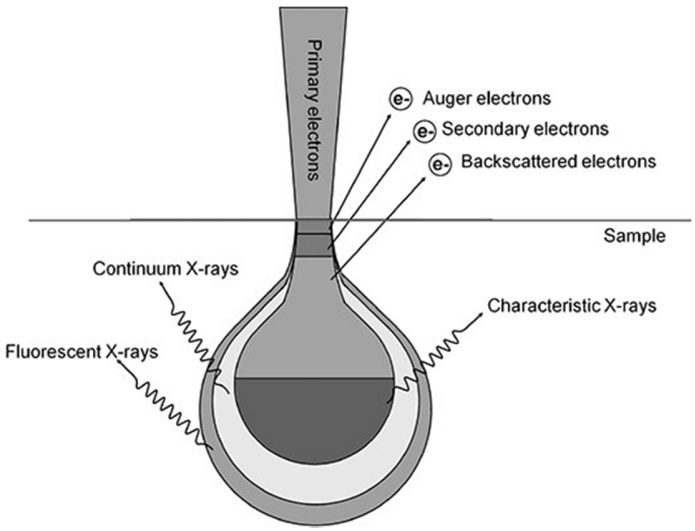

Fig. 2.4. Schematic diagram showing the regions in the interaction volume from which various types of electrons and photons originate upon irradiation with an electron beam. Adapted from [9].

The beam spot has variable size from a few nm to tens of nm and the area of analysis is then raster scanned and the out-coming signals are recorded as a function of the beam position to generate the image. The signals most commonly used to generate images come from secondary electrons (SE) and backscattered electrons (BSE). Secondary electrons are generated from inelastic scattering between the primary electrons (of the in-coming beam) and the electrons (from the core or the outer shells) of atoms in the sample. Such electrons have relatively low energies (< 50 eV), so it is possible to reveal only those generated in the outer layers of the material. On the contrary, all electrons with energies above 50 eV are classified as backscattered, generated as a result of elastic scattering of the electrons with the nuclei of the atoms of the material. Increasing the atomic number Z of the atoms in the sample, the contribution of backscattered electrons is strongly favored over the anelastically scattered ones.

In this work, FE-SEM (Field Emission SEM) measurements are performed using a Zeiss SIGMA (Carl Zeiss NTS GmbH, Oberkochen Germany) microscope (scheme in Fig. 2.5) equipped with a high performance Schottky field emitting source (W/ZrO_2), an electron accelerator (beam booster) to minimize the effects of broadening of the beam and the optics Gemini (with “In-Lens” detector, a very high sensitivity low energy secondary electrons detector). The samples have been coated with a 10 nm layer of platinum-palladium through Ar-plasma sputtering technique to give the suitable conductivity at the samples’ surface (Quorum .Q150T-ES. Quorum Tech. Ltd., Laughton UK)

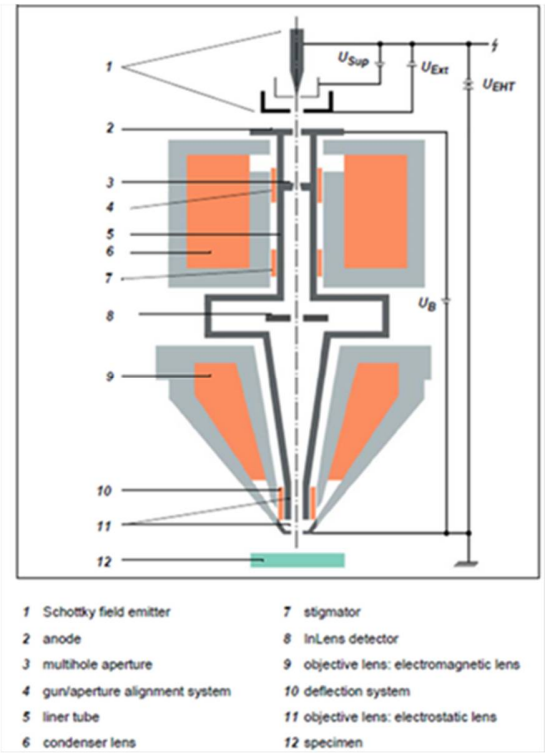

Fig. 2.5. Scheme diagram of the Zeiss SIGMA microscope column used to perform FE-SEM analysis in this work.

The SEM analysis of the samples studied in this work have been performed at ISTEC-CNR in collaboration with Dr. Mauro Mazzocchi.

IR and UV-Vis spectroscopies - IR and UV-Vis spectroscopies are suitable experimental tools to investigate the surface chemistry and the electronic properties of a wide class of metal oxides semiconductors such as those employed in this work to prepare gas sensors [10]. When such oxides are pure and stoichiometric they behave as insulators and are transparent at middle and near infrared (MIR and NIR) radiation as well as in the UV-Visible range until the energy corresponding to the electronic transition from valence band (VB) to conduction band (CB). However, MOX semiconductors are generally characterized by a large variety of impurities and point defects, such as oxygen vacancies, which create electronic levels at different depth in the gap. For n-type semiconductor oxides, electron donor levels with energy between 0.05 and 0.5 eV can be photo-ionized by the MIR radiation (400-4000 cm^{-1}) and the transition from the defect levels to the CB is observable. Donor levels with ionization energy > 0.5 eV correspond to NIR and Vis spectral regions. Steep absorption edge at radiation energy corresponding to the separation between defect level and the conduction band is expected. The density

of the electronic levels in the CB and the transition probability decrease on rising up in energy inside the conduction band: for this reasons, after the edge, the intensity of the absorption gradually decreases on increasing radiation frequency. The absorption edge can be made less steep if the initial level of the transition is a little band of defect levels. Moreover, in the MIR region electronic absorption edge can be modified or hidden by the presence of free electron absorption. Values of ionization energy < 0.05 eV are thermally available already at room temperature and the presence of free electrons in the CB can be revealed by a characteristic monotonic absorption (See Fig. 2.6). Truly "free" electrons cannot absorb a photon, because the requirement of energy and momentum conservation cannot be met simultaneously.

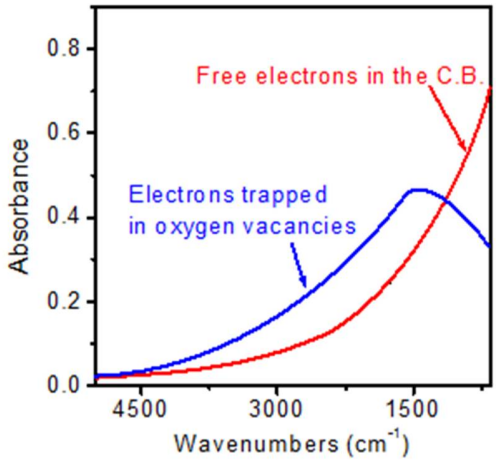

Fig.2.6. Schematic diagram showing the IR absorption bands related to free electrons in the CB (red curve) and to the transition of electrons from mono-ionized oxygen vacancies to the CB (blue curve). Adapted from [11].

The Vis-NIR radiation energy is usually necessary for polaronic transition, which can be described as a transition from a deep electronic level in the band gap to the CB.

Moreover, IR spectroscopy is useful to study surface reactions with gaseous species, detecting the vibrational modes of species in the gas phase or adsorbed on the surface of the sensing materials.

Indeed, in this work, IR spectroscopy has been used to study the sensing mechanism of different ZnO morphologies toward acetone. Absorption/transmission IR spectra were run on a Perkin-Elmer FTIR System 2000 spectrophotometer equipped with a Hg-Cd-Te cryo-detector, working in the range of wavenumbers 7200-580 cm^{-1} at a resolution of 2 cm^{-1}. For IR analysis powder samples were compressed in self-supporting discs (10 mg cm^{-2}) and placed in a commercial heated stainless steel cell (Aabspec) allowing thermal treatments in situ under vacuum or controlled atmosphere and the simultaneous registration of spectra at temperatures up to 600 °C. Before the measurements, the samples were treated

at 400 °C in vacuum and dry oxygen in order to clean the surface from adsorbed species and to maintain ZnO well oxidized. After this activation stage, the samples were cooled down to 50 °C in oxygen and outgassed before the admission of a mixture acetone/O_2 (1:5, p. acetone = 5 mbar). The IR spectra were recorded during the interaction with the mixture at increasing temperature up to 400 °C. The recorded spectra are reported as difference spectra in the figures: the spectrum subtracted is always that recorded after the activation treatment in oxygen at the same temperatures used for studying acetone interaction. In this way the modifications induced by acetone and the surface species formed are put in evidence.

2.2.3 Synthesis processes

In the following, a short description of the synthesis of the above mentioned materials (together with some peculiar morphological and structural characterizations) will be given except ZnO, at which the whole chapter 3 is devoted.

Synthesis of La FeO_3 powders - The heteronuclear complex, $La[Fe(CN)_6]\cdot 5H_2O$, is synthesized at room temperature by mixing equimolar amounts of $La(NO_3)_3\cdot 6H_2O$ and $K_3Fe(CN)_6$ in aqueous solutions under continuous stirring. The resulting reddish-orange precipitate is collected by suction filtration and then washed with water, ethanol, and diethyl ether, before drying in air at 50 °C. The complex is decomposed at selected temperatures, in order to obtain the perovskite-type powders. The temperatures at which the calcination of the complex is performed is selected from the results of the simultaneous thermogravimetric and differential thermal analysis (TG/DTA) of the complex (usually 700 °C). The decomposed powders are prepared by heating the complex in ambient air, up to the selected temperature of which is then held for 30 min [12].

The general scheme of co-precipitation route for $LaFeO_3$ is as follows:

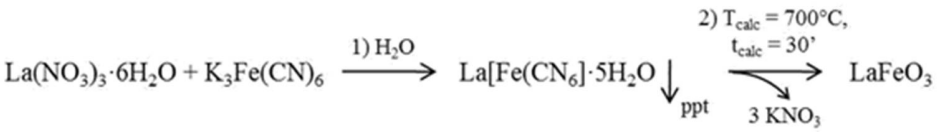

Recently, the preparation of this material has been optimized obtaining a more homogeneous morphology both at microscopic level (Fig. 2.7 A) and in regard to the size of the nanoparticles of which the microscopic agglomerates are constituted (Fig. 2.7 B).

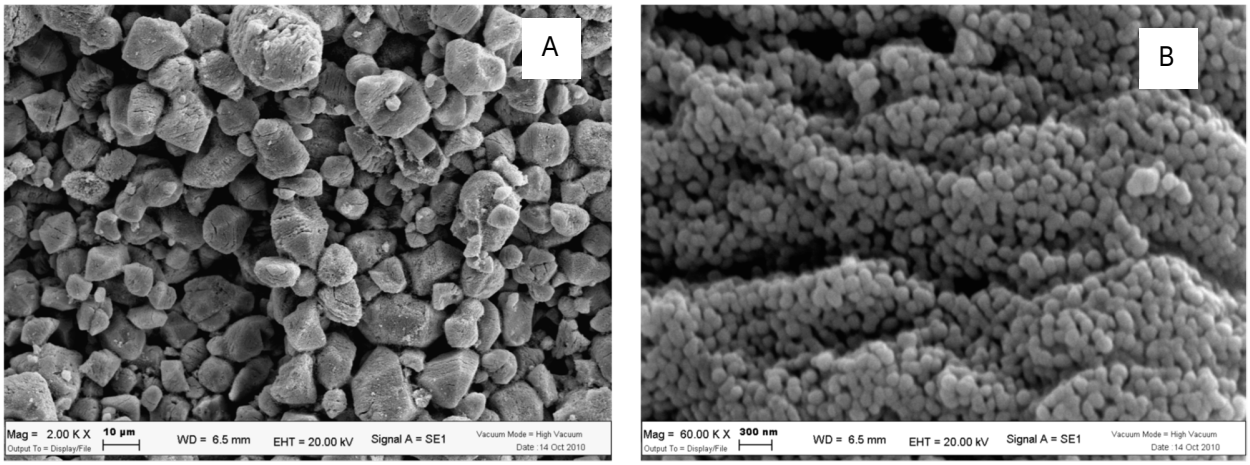

Fig. 2.7. A) SEM micrograph of a $LaFeO_3$ sample; B) after firing, particles of about 70-80 nm are highlighted.

Synthesis of WO_3 powders - Preparation of pure nanometric WO_3 powders are achieved through a partially modified sol–gel route, the modification consists in a variant to the chelation mechanism of tungsten. Room temperature reaction of 8 mmol of WCl_6 with C_2H_5OH abs and 2,4-pentanedione (PTN, 0.08M in C_2H_5OH abs) resulted in a paramagnetic blue W(V) complex. After a warm treatment in a sonic bath, the solution is stationary for 2 h at room temperature and a blue precipitate is formed. The blue precursor is dried, crushed and then annealed at T = 650 ◦C for 2 h. The reaction yields the 96% of yellow WO_3 pure powder. The calcination temperature has been chosen on the basis of the thermal (TG/DTA) and structural (X-Ray diffraction and transmission electronic microscopy-TEM) characterizations. Indeed, the calcination at 650 °C was resulted the better compromise between structural stability and grain size. In the table 2.1, the XRD characterization is reported [13].

Table 2.1. Effect of the temperature on crystallite size,grain dimensions and crystalline phases

T (°C)	Powders			Films
	Crystalline phase	D (nm)	Grain size (nm)	Grain size (nm)
450	β	20	–	–
550	β	23	< 50	–
650	β + γ	60	30–80	125–185
750	γ	100	100–300	400–750
850	γ	105	400–1000	250–380, 1000–1400

The deposition of thick films confirmed the choice of the calcination temperature, indeed, as it is possible to observe in the SEM images (Figs. 2.8 A and B), the film obtained by the powder calcined at 650 °C is characterized by a modest coalescence of grains, homogeneously distributed in size.

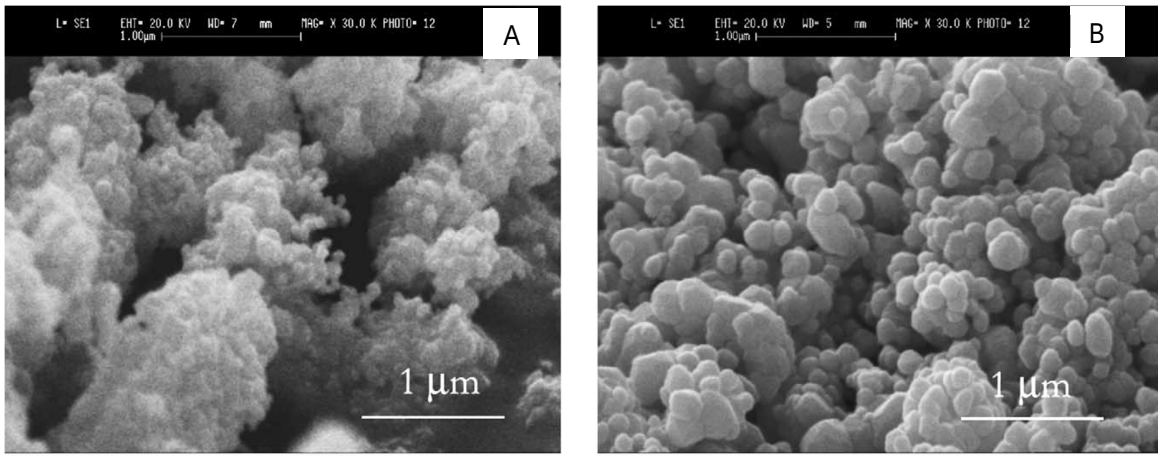

Fig. 2.8. SEM micrographs of WO_3 powder calcined at 650 °C for 2 h (A) and corresponding thick film heated at 650 °C for 1 h (B).

Synthesis of SnO_2 powders - Pure tin oxide powders are prepared according to procedure described in [14]: to a n-butanol solution 0.7 M of Sn(II)2–ethylexanoate a given amount of deionized water is added drop-wise and the mixture is stirred at room temperature during 3 h. The molar ratio of water to Sn must be 4 and the pH of the solution is adjusted to be 1 with HNO_3. The resulting gel is dried overnight at 95°C and subsequently calcined at 550°C for 2 h.

Synthesis of TiO_2 powder - Ti(IV) n-butoxide is dissolved in absolute ethanol (0.23 M) and added drop by drop to a solution of ethanol/ water 1:1 vol under rapid stirring. After stirring, the suspension is filtered to obtain a white precipitate which is dried in air (100°C) for 16 h. Finally, the powders are calcined at 450°C in air for 2 h [15].

Synthesis of $Ti_xSn_{1-x}O_2$ powders - $Ti_xSn_{1-x}O_2$ solid solutions with different molar ratios are obtained by sol-gel route from stoichiometric solutions of their metal-alkoxides precursors, Sn(II)2–ethylexanoate and Ti(IV) n-butoxide. Diluted HNO_3 solution was added drop-by-drop to hydrolyze the metalorganic molecules. The entire process was carried out by maintaining the solution under gentle stirring, to achieve a pale yellow colloid, which played the role of the solid-solution precursor. The colloid and

water-mother were separated by filtration. The resultant xerogel was converted into a binary oxide by calcining at 550°C [16].

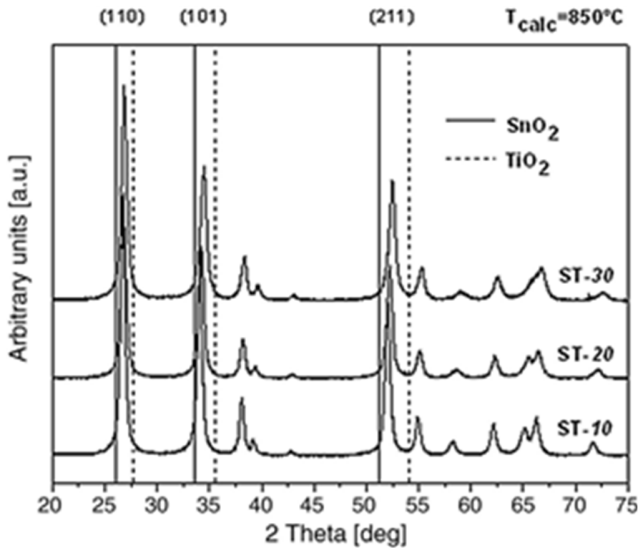

Fig. 2.9. X-ray diffraction pattern of solid solutions with x = 0.1, 0.2 e 0.3, calcined at 550° for 2h. The reflexes lay within the peak positions of pure TiO_2 rutile (dotted line; S.G.: P42/mnm JCPDS 75-1748) and SnO_2 cassiterite (solid line; S.G.: P42/mnm JCPDS 77-0452).

XRD characterizations highlighted on all studied $Ti_xSn_{1-x}O_2$ solid solutions a single rutile type crystalline phase. No lines of pure Ti and Sn single oxides were observed, establishing the formation of the binary solid solutions, as shown in Fig. 2.9 for x = 0.1, 0.2 e 0.3. Microscopic observations showed morphologies consisting in nanoparticles for all powders calcined at 550°C, the nanostructure being maintained also after thermal treatments carried out up to 1050 °C. In Fig. 2.10 A, a TEM image of the powder with x = 0.3 is reported, while in Fig. 2.10 B, a SEM micrograph of a thick film, obtained with x = 0.2 powders and fired at 850 °C, is shown. The particle size distribution for the powders after calcination averaged about 20 nm, while in the films the grain diameter did not exceed 50 nm.

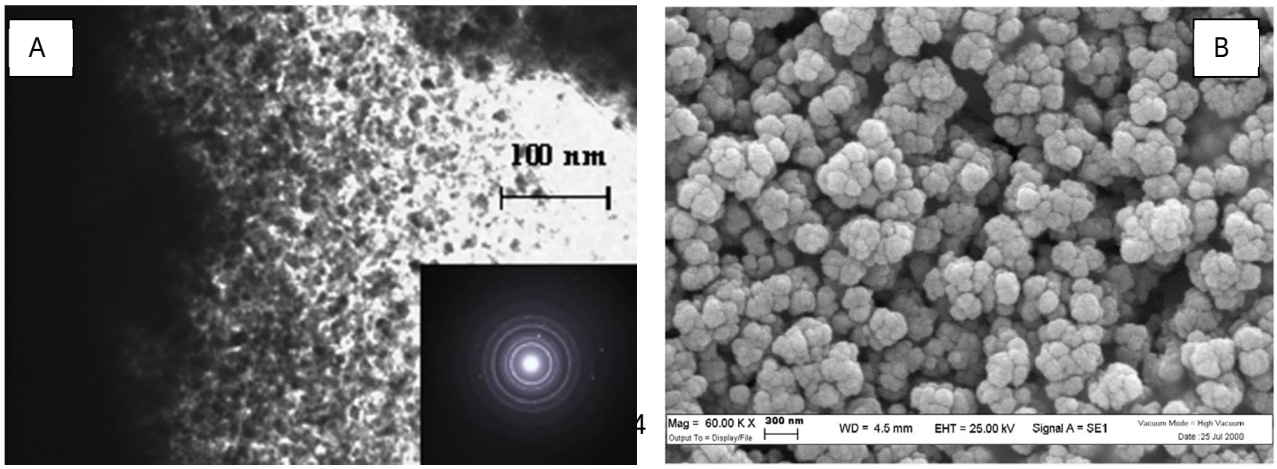

Fig. 2.10. TEM micrographs of a sample with the molar ratio x = 0.3 calcined at 550 °C (A) and a SEM micrograph of a thick film of x = 0.2 sample, fired at 850 °C.

Synthesis of $Sn_xW_{1-x}O_2$. - A solution of Tin(II) 2-ethylhexanoate is dissolved in a minimum amount of 1-butanol added to a 0.2 M solution of WCl_6 in absolute ethanol (Sn:W=10:90, 20:80, 30:70 molar ratio). In order to catalyze the hydrolysis process, 1 ml of water diluted HNO_3 solution (pH=1) is added dropwise under continuous stirring. The solution is kept at 50 °C in an ultrasonic bath for 3 h. The resulting white/yellowish powder (the precursor of the final oxide) is filtered by gravity and washed several times in ethanol. Then the product is dried at 100 °C overnight in an oven and afterwards calcined at 550 °C for 2 h. The yield in the $(W_{0.9}Sn_{0.1})O_{3-x}$ oxide was around 85%. The calcination temperature has been determined by TG/DTA analysis performed at 20 °C/min in natural air flow [17].

Synthesis of (Ti, Ta, V)O_2 solid solution. - The material is based on titanium dioxide modified by tantalum and vanadium. It is well known that the addition of ions with valence 5^+ are most effective in hindering the anatase to rutile phase transition and in inhibition of grain coalescence. This is certainly true for Nb and Ta, but unfortunately vanadium addition facilitates it because of the ionic radius considerably smaller than that of Ti [15,18]. However, this material has been synthesized to merge the positive effects produced by the two additives: addition with Ta to hinder the exaggerated grain growth typical of titania during heating, while V for the useful catalytic and optical properties. In summary, the contemporaneous addition of tantalum and vanadium partially reduces the effect of particle coalescence caused by vanadium as long as the content of vanadium is balanced by tantalum. The suitable proportion resulted Ti:Ta:V as 100:15:5 [19].

2.3 SCREEN-PRINTING PROCESS

Through screen printing technique, the sensing film, interdigitated contact and heater element are deposited on the same substrate (alumina or nitride/oxide membranes onto silicon). To fabricate thick film sensing layers, it is necessary to prepare a viscous paste by adding to the functional material, in form of powder, an organic vehicle consisting of a mixture of rheological agents in volatile solvents. It is a sacrificial ingredient that completely disappears during the thermal processes carried out onto the

films, during which the film microstructure is formed. The amount and composition of the organic media make the paste printable and give to the fired films some electrical properties and the macroscopic appearance (i.e. surface crack-free). The paste contains a third constituent, a small amount of a bonding agent, a glass frit or an oxide, promoting the film adhesion to the substrate. The most common formulation for screen-printable paste is listed in Table 2.2; specific paste compositions are highly proprietary.

Table 2.2. Typical components in screen-printable paste for gas sensing devices (adapted from [2]).

	Action	Component
	Functional material (nanopowder)	• Metal
		• Metal oxide (pure, loaded)
		• Solid solution or mixed oxide
	Powder sintering aid	Glass frit (ex.: lead borosilicate)
Organic vehicle	Organic wetting agent with low volatility	• Terpineol
		• Butyl Carbitol or other glycol ethers
	Binder with high molecular weight (resin)	• Ethylcellulose
		• Acrylic resins
		• Polyvinyl-pyrrolidone
	Surfactant	Lauric acid or other saturated fatty acids
	Catalyst	Noble metals (ex.: Pt, Pd, Au, Ag)
Rheology of the paste		
	Parameter	Range
	Share rate (s^{-1})	100-1000
	Viscosity (mPa)	70000-15000

One of the main steps in the fabrication process is the printing on ceramic substrates. For this process, a patterned woven mesh screen defines the pattern to be printed onto a substrate by a squeegee, a polymeric blade whose stiffness is chosen according to the process to be carried out. The screen is a set of regularly spaced woven anchored on a rigid frame, under calibrated-tension conditions. The diameter and type of the cables depend on the detail required for the pattern, the rheology of the paste, shape and roughness of the substrate and the thickness of the final layer. To print a layer with a specific pattern,

the paste must flow only through the empty areas of the screen; each printed block will merge into a compact film. In Fig. 2.11, a schematic drawing of the screen-printing machine working is shown.

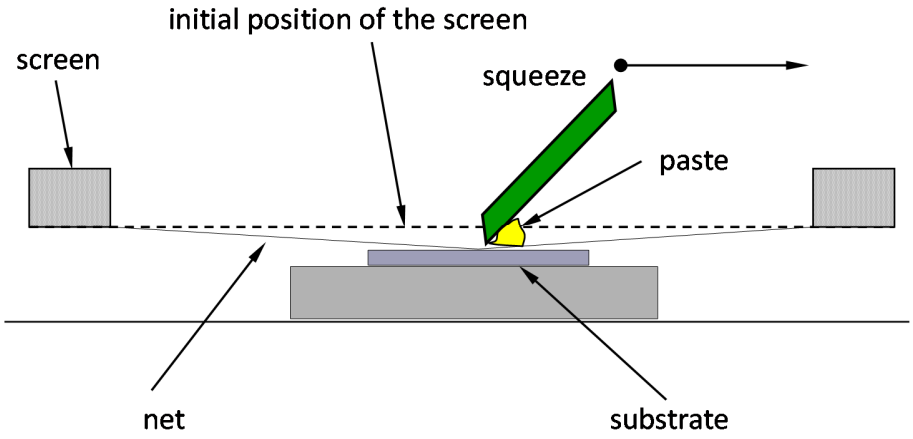

Fig. 2.11. Scheme of the working of a screen-printing machine

The deposited layer, varying from a few to ~30 μm, depends on certain parameters, such as dimension of the particles in the functional phase, paste viscosity, screen mesh number, tension on the wires constituting the screen, hardness and speed of the rubber blade, distance between the screen and the substrate (snap-off). After printing, the drying allows the removal of the volatile components from the paste (100÷200°C). Shrinkage occurs when the liquid between the solid particles is removed and inter-particle separation decreases, this effect being maximized when the grain size distribution of the powders is homogeneous as far as possible.

Drying is the step prior to firing, the thermal process consolidating the shape of the printed layer. Moreover, through physical and chemical transformations, it imparts to the sensing layer the desired electrical and micro-structural properties [20].

Firing is performed in furnaces under ambient atmosphere between 600÷900°C. The oxygen partial pressure drives the content of metals or metalloids with the proper oxidation state, in the functional material; rarely some layers need to be treated in a different atmosphere to tailor the stoichiometry of the material itself.

Firing proceeds into three steps: 1) organics burnout and gaseous by-products elimination; 2) sintering and 3) cooling [21].

The glass frit, in the paste formulation, is essential to improve the adhesion of the printed film onto the substrate. During the sintering it achieves its softening point turning from a solid to a viscous glassy

matrix wetting uniformly the grains. The matrix draws the particles together enabling their sliding and rearrangement into a denser configuration. Rarely more than 1% w/w of glass frit, with respect to the weight of the powder, is required to coat entirely the grains at the softening point. When the frit is non homogeneously distributed within the paste, different rates of densification and grain growth may cause inhomogeneous microstructure and a low average density of the resulting film. In Fig. 2.12 the flow chart of the complete processing is shown.

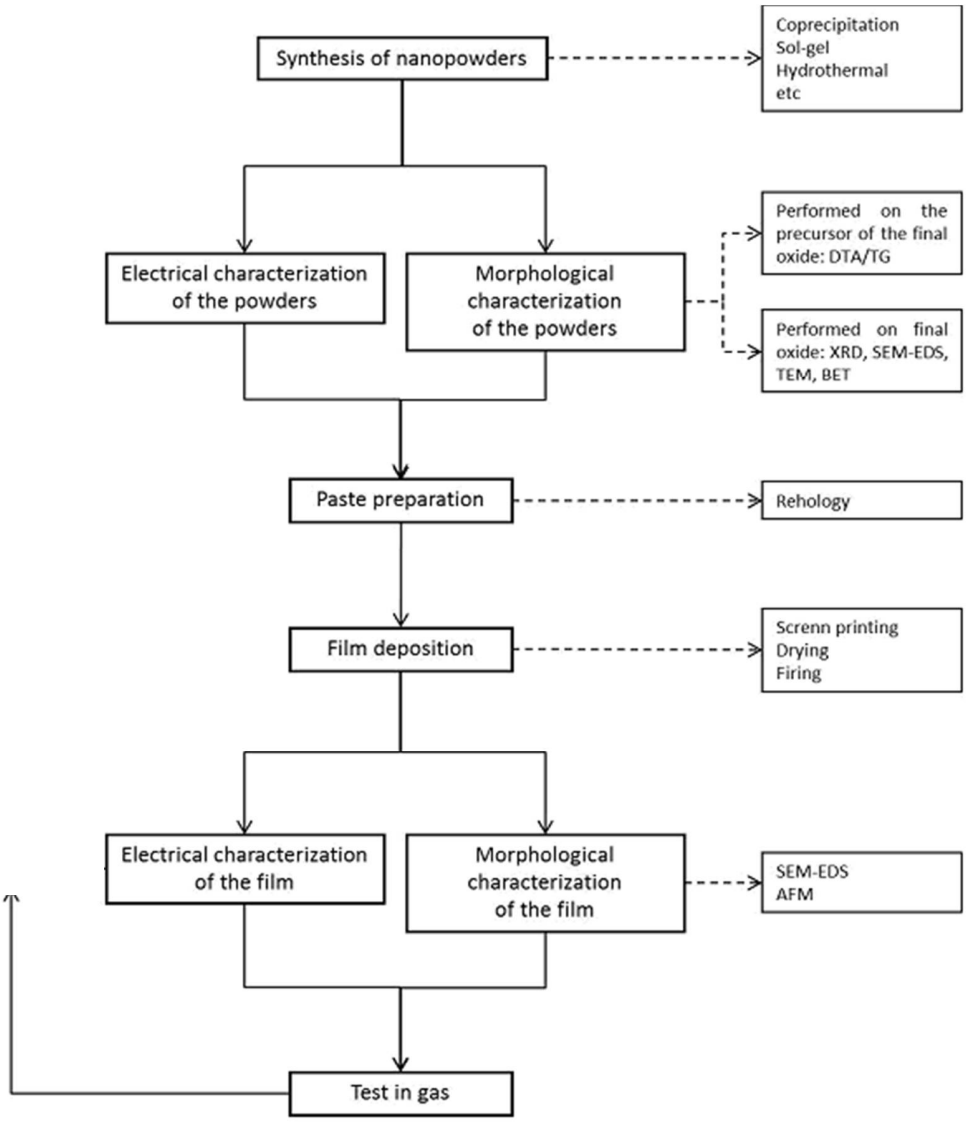

Fig. 2.12. Flow chart of the complete screen-printing process of thick film gas sensors beginning on the synthesis of the nano-powders (from [2]).

In Fig. 2.13, an image of a sensing layer printed on an alumina substrate, a complete sensor and a group of three different sensors are reported.

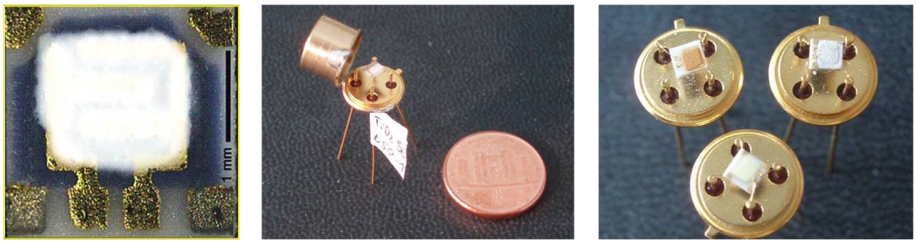

Fig. 2.13. A sensing layer and few sensors based on different functional materials.

2.4 ELECTRICAL LABORATORY CHARACTERIZATIONS

For electrical characterizations the sensors were placed in a sealed test chamber maintained at a fixed ambient temperature of 22 °C. Indeed, as described in a previous work [13–Ch1], the ambient temperature is directly influencing the sensor behavior, even if the working temperature of the sensor is kept almost constant. The flow-through technique was used to test the electrical properties of the sensing layers. The measurement of conductance was carried out maintaining a flow rate of 0.5 L/min using synthetic air as carrier gas in dry or wet (RH = 40%) conditions. Electrical measurements of thick films are carried out to study the sensors both from a fundamental point of view and as functional material for gas sensing. Thereby, conductance measurements are performed to study the semiconductor behavior (Arrhenius plots), the surface barrier potential heights and the gas sensing properties.

The Arrhenius plots are obtained by changing the temperature between 360 and 900 K at the heating rate of 3 K/min, while the direct determination of the height of the surface potential barrier at a fixed temperature is carried out using the method of temperature-stimulated conductance measurements. For this aim the conductance is measured as a function of time, after a change of temperature so fast that it is possible to assume the constancy of the barrier while the conductance changes due to the variation of free carriers. Afterwards, through Morrison's equation [21-Ch1], which factorizes the surface and bulk contributions, the heights of the potential barrier as a function of temperature can be calculated from the measured conductance values of the Arrhenius plot.

The sensing and selectivity properties are studied carrying out dynamical responses of sensing films obtained in presence of mixture of different gases by varying the operating temperature from 350 to 650

°C. The sensor response is defined as ratio between the conductance in presence of the target gas and the conductance in air.

Hereafter, the main electrical measurements to perform in laboratory are listed:

a) Measurements to identify the functional material more sensitive toward a specific gas;

b) Measurements to determine the responses toward different gases for a specific functional material;

c) Measurements to determine the best working temperature for each material and for each gas of interest;

d) Measurements to determine the influence of the water vapour partial pressure on the amplitude of the responses;

e) Measurements to determine the calibration curves for each gas of interest in dry or wet conditions;

f) Measurements to determine the *cross-sensitivity*, i.e. measures in presence of the gas of interest and of possible interfering gases in the context of a specific application;

g) Measurements to select sensors with the same performance toward the gas of interest;

h) Repeatability measurements to determine the reliability of the preparation process of a specific sensor.

REFERENCES

[1] M. Prudenziati, Handbook of Sensors and Actuators: Thick Film Sensors Elsevier, Amsterdam, 1994.

[2] V. Guidi, C. Malagu, B. Vendemiati and M. C. Carotta, Printed semiconducting gas sensors in Printed films: Materials science and applications in sensors, electronics and photonics, M. Prudenziati, J. Hormadaly (Eds.), Woodhead publishing Limited, Cambridge, UK, 2012.

[3] D. Lutic, M. Sanati and A. Lloyd Spetz, Gas Sensors, in J. A. Rodríguez and M. Fernandez García, Synthesis, Properties and Applications of Oxide Nanomaterials, New York, Wiley, 2007, 411-450.

[4] W.L. Bragg, The diffraction of X-rays by crystals, Nobel lecture, September 6, 1922.

[5] H.P. Klug, L.E. Alexander, X-ray Diffraction Procedures for Polycrystalline and Amorphous Materials, J. Wiley & Sons, Chicester UK, 1954.

[6] FullProf has been developed starting from the program of Wiles and Young, J. Appl. Cryst.14 (1981) 149, (DBW3.2S, Versions 8711 and 8804) which, in turn, is also a major modification of the original Rietveld-Hewat program (H.M. Rietveld, Acta Cryst. 22 (1967) 151).

[7] E. Ruska, The Development of the Electron Microscope and of Electron Microscopy, Nobel Lecture, December 8, 1986.

[8] J. Goldstein, D.E. Newbuty, P. Echlin, D.C. Joy, Jr A.D. Romig, C.E. Lyman, C. Fiori, E. Lifshin, Scanning Electron Microscopy and X-ray Microanalysis, 3rd edition, Kluwer Academic, New York, USA, 2003.

[9] Z. Zhang, T. Zhou, M. Lu, A. W. C. Poh and S. N. Piramanayagam, Cobalt Nanomaterials: Synthesis and Characterization, Nanotechnologies for the Life Sciences, Wiley-VCH, 2011.

[10] G. Busca, The use of vibrational spectroscopies in studies of heterogeneous catalysis by metal oxides: an introduction, Catalysis Today 27 (1996) 323-352.

[11] S. Morandi, A. Fioravanti, G. Cerrato, S. Lettieri, M. Sacerdoti, M.C. Carotta, Facile synthesis of ZnO nano-structures: morphology influence on electronic properties, conference presentation at 16th International Meeting on Chemical Sensors (IMCS), Jeju Island, South Korea July 10-14, 2016.

[12] G. Martinelli, M.C. Carotta, M. Ferroni, Y. Sadaoka, E. Traversa, Screen-printed perovskite-type thick films as gas sensors for environmental monitoring, Sens. Actuators B 55 (1999) 99–110.

[13] V. Guidi, M. Blo, M.A. Butturi, M.C. Carotta, S. Galliera, A. Giberti, C. Malagù, G. Martinelli, M. Piga, M. Sacerdoti, B. Vendemiati, Aqueous and alcoholic syntheses of tungsten trioxide powders for NO_2 detection, Sensors and Actuators B 100 (2004) 277–282.

[14] A. Chiorino, G. Ghiotti, F. Prinetto, M.C. Carotta, D. Gnani, G. Martinelli, Preparation and characterization of SnO_2 and MoOx–SnO_2 nanosized powders for thick film gas sensors, Sens. Actuators B 58 (1999) 338–349.

[15] E. Traversa, M.L. Di Vona, S. Licoccia, M. Sacerdoti, M.C. Carotta, L. Crema, G. Martinelli, Sol–gel processed TiO_2-based nano-sized powders for use in thick film gas sensors for atmospheric pollutant monitoring, J. Sol–Gel Sci. Technol.22 (2001) 167–179.

[16] M.C. Carotta, A. Fioravanti, S. Gherardi, G. Ghiotti, C. Malagù, S. Morandi, and M. Sacerdoti, (Ti, Sn) binary oxides as functional materials for gas sensing, Sensors and Actuators B 194 (2014) 195-205.

[17] M.C. Carotta, A. Cervi, A. Fioravanti, S. Gherardi, A. Giberti, B. Vendemiati, D. Vincenzi, and M. Sacerdoti, A novel ozone detection at room temperature through UV-led-assisted ZnO thick film sensors, Thin Solid Films 520 (2011) 939–946.

[18] M.C. Carotta, M. Ferroni, S. Gherardi, V. Guidi, C. Malagù, G. Martinelli, M. Sacerdoti, M.L. Di Vona, S. Licoccia, E. Traversa, Thick film gas sensors based on vanadium-titanium oxide powder prepared by innovative sol-gel synthesis, Journal of the European Ceramics Society, 24 (2004) 1409-1413.

[19] M.C. Carotta, S. Galliera, V. Guidi, C. Malagù, B. Vendemiati, A. Zanni, G. Martinelli, M. Sacerdoti, S. Licoccia, M.L. Di Vona, E. Traversa, Vanadium and Tantalum doped Titanium oxide (TiTaV): a novel material for gas sensing, Sensors and Actuators B 108 (2005) 89-96.

[20] J. S. Reed, Principles of ceramic processing, II Ed., New York, Wiley and Sons Inc., 1995, chap. 27.

[21] J. S. Reed, Principles of ceramic processing, II Ed., New York, Wiley and Sons Inc., 1995, chap. 29.

CHAPTER 3

SYNTHESIS OF ZNO NANOMORPHOLOGIES: STRUCTURAL AND ELECTRONIC PROPERTIES

3.1 INTRODUCTION

Zinc oxide (ZnO) is an inorganic compound that usually appears as a white powder, nearly insoluble in water. It naturally occurs as the rare mineral zincite. The first description and its analysis were given in 1810 from A. Bruce [1]. He discovered zincite in Franklin (New Jersey, USA), now well-known as the bigger deposit in the world; however most of used ZnO is synthetically produced. At the end of the 19th-century ZnO began to be employed as a white pigment in painting and as an active ingredient in antiseptic treatment of wounds. In early 1920s, O. Losev discovered the amplification ability of ZnO crystal to improve the reception and transmission of radio waves. In the 1930s, the first investigation on its physical, structural, photo- and electro-luminescence properties was carried out. At the beginning of semiconductor age (around 1950), ZnO research entered in a "modern rediscovery" where its optical, electronic and catalytic properties were explored. In 1960 the discovery of its piezoelectric properties led to the first surface acoustic devices based on ZnO thin layer. In 1962, *Seiyama et al.* described a new detector for gaseous components using semiconductive thin film based on ZnO [2]. In 1965, ZnO/Au Schottky barriers were formed and in 1967 the first heterojunction LED was demonstrated (Cu_2O was used as the p-type material) [3]. Later it was abandoned, but from 1990 until now, research and development of ZnO nanostructures and relative applications are increasing as shown by the number of publications per year in the Fig 1.

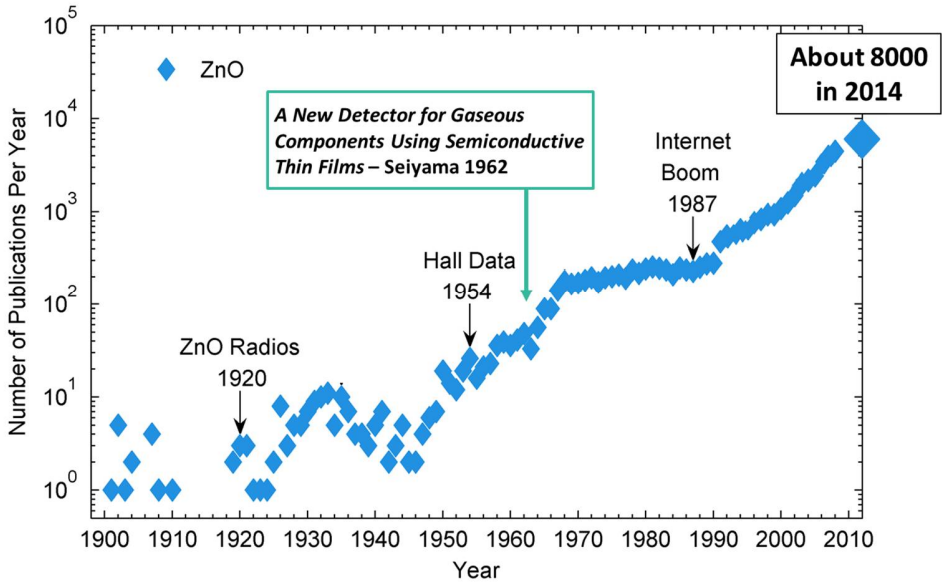

Fig. 3.1. Number of publications per year about ZnO, obtained searching the term "ZnO" in abstract, title, or keywords on www.scopus.com.

The renewed interest for ZnO, in nineteens has been aroused by the discovery of its aptitude for being grown in a wide diversity of nanomorphologies and of different functional properties. Indeed, ZnO can be grown by a great deal of methods, such as vapor deposition, wet chemical methods, etc., obtaining the widest family of unique nanostructures among all known materials. Novel applications resulted in optoelectronics, hybrid solar cells, sensors, biomedical field. It is also widely used as an additive into numerous materials and products such as plastics, ceramics, glass, cement, rubber, lubricants, paints, adhesives, foods, batteries, fire retardants, etc..

3.2 BASIC PROPERTIES

ZnO is a II-VI compound semiconductor whose chemical bond is between covalent and ionic. It is a direct wide band-gap (3.37 eV) compound semiconductor with n-type conductivity due to intrinsic stoichiometric defects (generally oxygen vacancies). It has an high exciton binding energy (60 meV) so it can ensure both an efficient excitonic emission and an ultraviolet (UV) luminescence at room temperature. ZnO is also transparent to visible light and can be made highly conductive by doping. It can crystallize in three different crystal structures: cubic rocksalt (high pressure phase, pressure > 6 GPa), cubic zinc blende, and hexagonal wurtzite (Fig. 3.2). The last one is the most common and stable

phase at ambient conditions belonging to the hexagonal space group $P6_3mc$ with the lattice parameters a = 3.2499 and c = 5.2066 Å. The zinc oxide wurtzite structure consist of alternating planes composed of tetrahedrally coordinated O^{2-} and Zn^{2+} ions, stacked alternately along the c-axis. The tetrahedral coordination in ZnO results in non-centrosymmetric structure and consequently piezoelectric and pyroelectric properties.

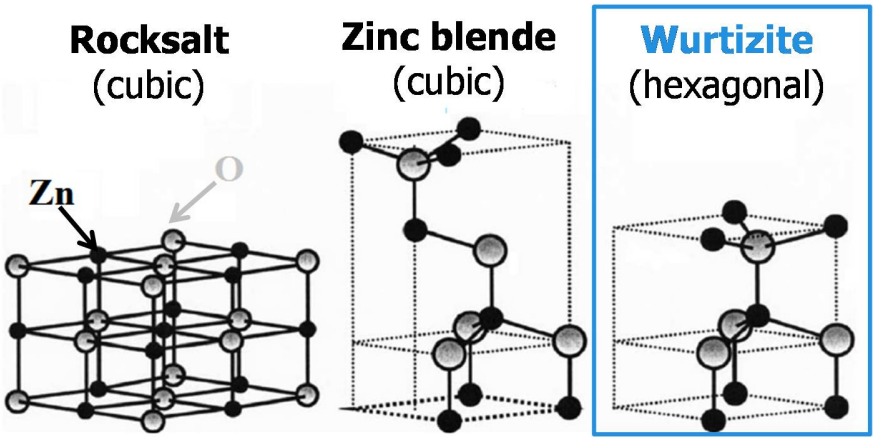

Fig. 3.2. Representation of the three possible ZnO crystal structures: cubic rocksalt, cubic zinc blende, and hexagonal wurtzite. The gray and black spheres denote Zn and O atoms, respectively. Adapted from [4].

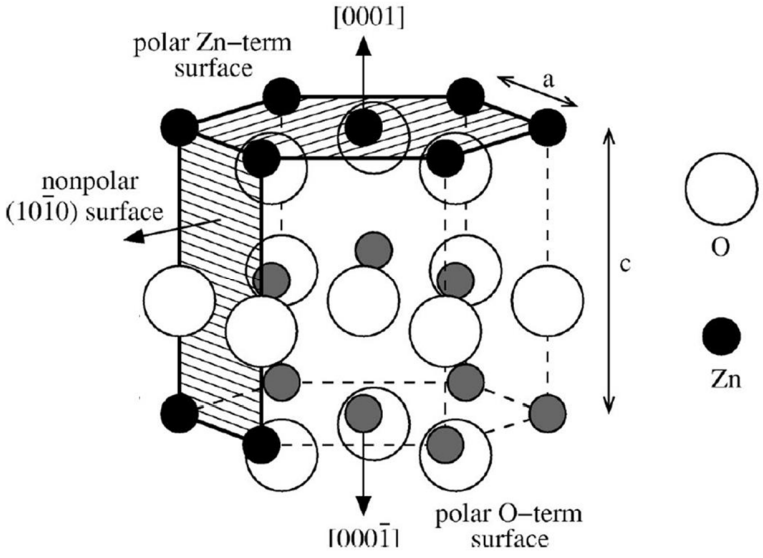

Fig. 3.3. ZnO wurtzite structure with the two polar planes (zinc terminated and oxygen terminated) and the nonpolar $(10\bar{1}0)$ *surfaces. Adapted from [5].*

Polar surfaces are typical of ZnO, being the basal plane the most common. The oppositely charged ions produce positively charged Zn-(0001) and negatively charged O-$(000\bar{1})$ surfaces, resulting in spontaneous polarization along the c-axis as well as a divergence in surface energy (Fig. 3.3). To maintain a stable structure, the polar surfaces generally have facets or exhibit considerable surface reconstructions, but in ZnO they are atomically flat, stable and without reconstruction [5].

The other two most commonly observed facets for ZnO are $\{10\bar{1}0\}$ and $\{11\bar{2}0\}$, which are non-polar surfaces and have lower energy than the {0001} facets [6].

It has been observed, firstly by Laudise [7], that the relationship between the velocities of ZnO crystal growth to different directions is: $v_{[0001]} > v_{[10\bar{1}1]} > v_{[10\bar{1}0]}$.

Together with the polar surfaces, ZnO exhibits a wide range of novel morphologies (such as nanoparticles, nanowires, nanorods, nanosheets, nanoneedles, nanoflowers, etc..) that can be grown by tuning the growth rates along these directions. They can be divided in one- (1D), two- (2D) or three-dimensional (3D) structures depending on the number of dimensions in which the material has nanometric modulations [8]. Macroscopically, a crystal has different kinetic parameters for different crystal planes, which are emphasized under controlled growth conditions. Thus, after an initial period of nucleation and incubation, a crystallite will commonly develop into a three-dimensional object with well-defined, low index crystallographic faces.

Wet chemical methods have been demonstrated to be a powerful and versatile technique for growing ZnO nanostructures [9].

3.3 SYNTHESIS AND MORPHOLOGICAL CHARACTERIZATION OF ZNO NANOMORPHOLOGIES

In this work, ZnO with different nanomorphologies (nanosheets, bisphenoids, nanoflowers, short and long needles, prisms and flowers) has been synthesized by means of the following methods:

- through sol-gel methodology, previously described in section 2.2.1,
- starting from the same precursor, zinc nitrate hexahydrate ($Zn(NO_3)_2$*$6H_2O$, ≥99.0 %, Sigma-Aldrich), in water solution,
- using weak bases (ammonia solution, hexametilenetetramine) to catalyzed the hydrolysis,
- by a rapid crystallization, and

- at low temperatures.

The general and simplified synthesis process in alkali solution can be described as follows [9]:

$$Zn^{2+} + 2OH^- \longleftrightarrow Zn(OH)_2$$

$$Zn(OH)_2 + 2OH^- \longleftrightarrow [Zn(OH)_4]^{2-}$$

$$[Zn(OH)_4]^{2-} \longleftrightarrow ZnO_2^{2-} + 2H_2O$$

$$ZnO_2^{2-} + H_2O \longleftrightarrow ZnO + 2OH^-$$

$$ZnO + OH^- \longleftrightarrow ZnOOH^-$$

Nanosheets (NS) - Nanosheets were prepared adding a proper amount of ammonium hydroxide (28%, Carlo Erba Reagents) to a water solution 0.05 M of $Zn(NO_3)_2*6H_2O$, bringing the solution pH to 10. After 1 hour the precipitate was filtered, washed several times with water and diethyl ether, then dried at 100 °C in air overnight and calcined at 450 °C for 2 h.

The SEM images of NS powders highlighted sheets of rhombic shape, which longer diagonal is about 6 μm in size, while the shorter diagonal is about 3 μm long. However, the fine structure is given by nanoparticles of about 60-70 nm sized (Fig. 3.4)

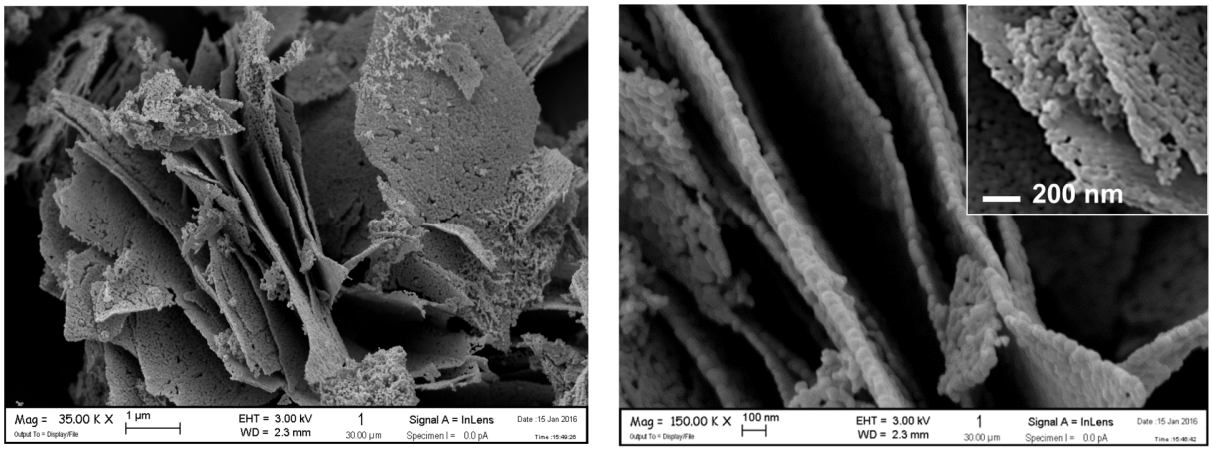

Fig. 3.4. SEM micrographs of a ZnO nanoparticles assembled in form of rhombic sheets.

Bisphenoidal nanoaggregates (BP) - Bisphenoidal nanoaggregates were prepared adding a proper amount of ammonium hydroxide (28%, Carlo Erba Reagents) to a water solution 0.05 M of $Zn(NO_3)_2*6H_2O$, to reach a pH of 10. A small amount of polyethyleneglycol (PEG, MW = 400) was

next added after mixing. After 1 hour of ultrasonic treatment at RT, the precipitate was filtered, washed several times with water and diethyl ether, then dried at 100 °C in air overnight and calcined at 450 °C for 2 h.

SEM micrograph of bisphenoids showed nanoparticles aggregates which z axis is about 10 µm and the fine structure is constituted by nanoparticles only slightly lower than those of the NS powders (see Fig. 3.5).

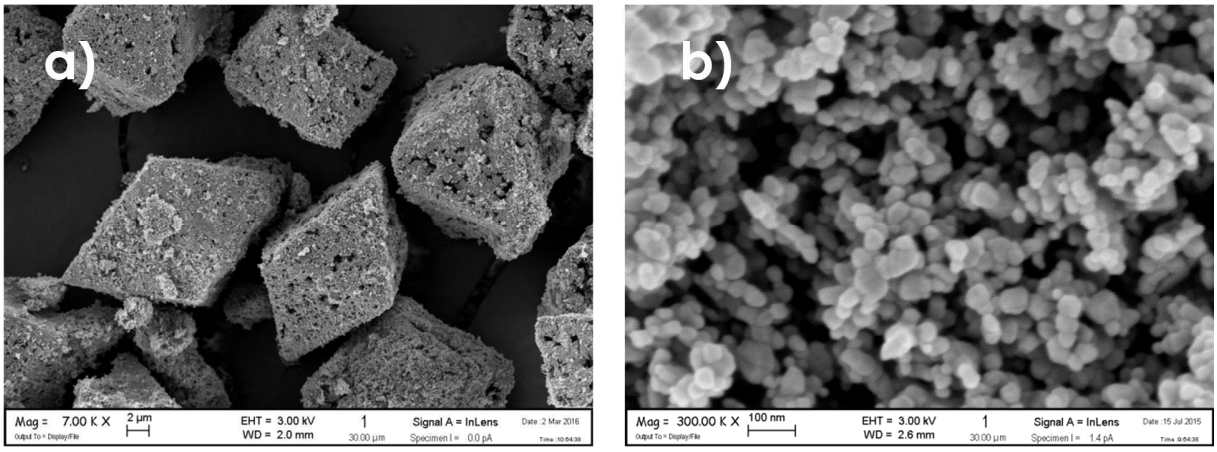

Fig. 3.5. SEM micrograph of the bisphenoidal nanoparticles aggregates (a). Magnification of the surface of a bisphenoid (b).

Nanoflowers (NF) - This particular morphology were prepared heating a water solution 0.05 M of $Zn(NO_3)_2*6H_2O$ at 60 °C then adding a proper amount of ammonium hydroxide (28%, Carlo Erba Reagents) to reach a pH of 10. After 30 min of thermal treatment at 60 °C, the ZnO precipitate was filtered, washed several times with water and diethyl ether, then dried at 100 °C in air overnight.

SEM analysis showed NF powders composed of grains about 30 nm in size in a flower structure which diameter is about 1 µm (Fig 3.6).

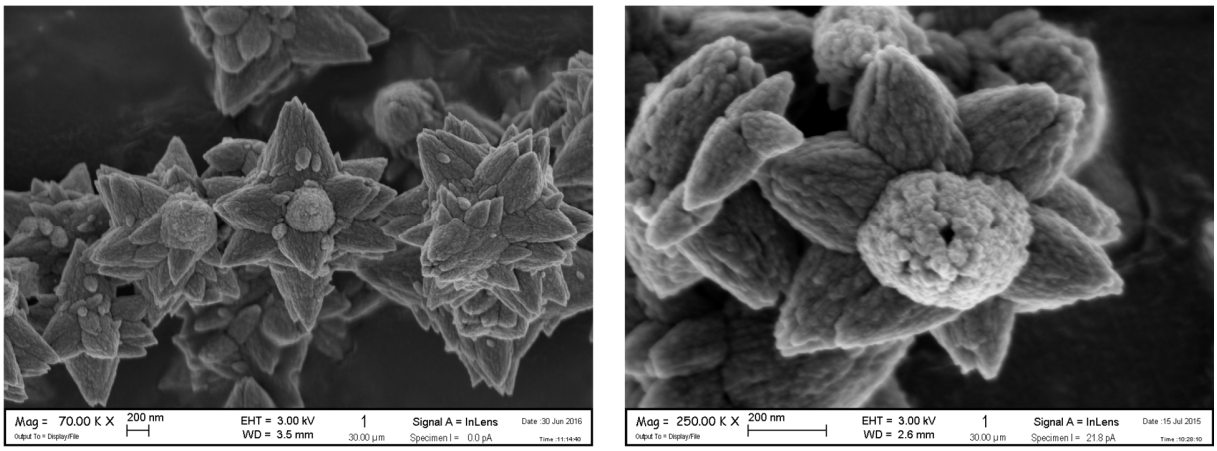

Fig. 3.6. SEM micrographs of ZnO nanoflower aggregates.

<u>*Short and long needles (SN and LN)*</u> - Needles were prepared adding a proper amount of ammonium hydroxide (28%, Carlo Erba Reagents) to a water solution 0.05 M of $Zn(NO_3)_2*6H_2O$, bringing the solution pH to 10. The mixture was then kept at the temperature of 95 °C for 7 hours in a muffle furnace to obtain short needles and in a ultrasonic bath in the case of long needles. The precipitate was filtered by gravity, washed several times with water and diethyl ether, before drying at 100 °C in air overnight in oven.

Fig. 3.7 a highlights SN morphology constituted by an homogeneous distribution of needles 200-300 nm wide and about 3-4 μm long, while LN needles are about 100 nm wide and 7-8 μm long (see Fig. 3.7 b).

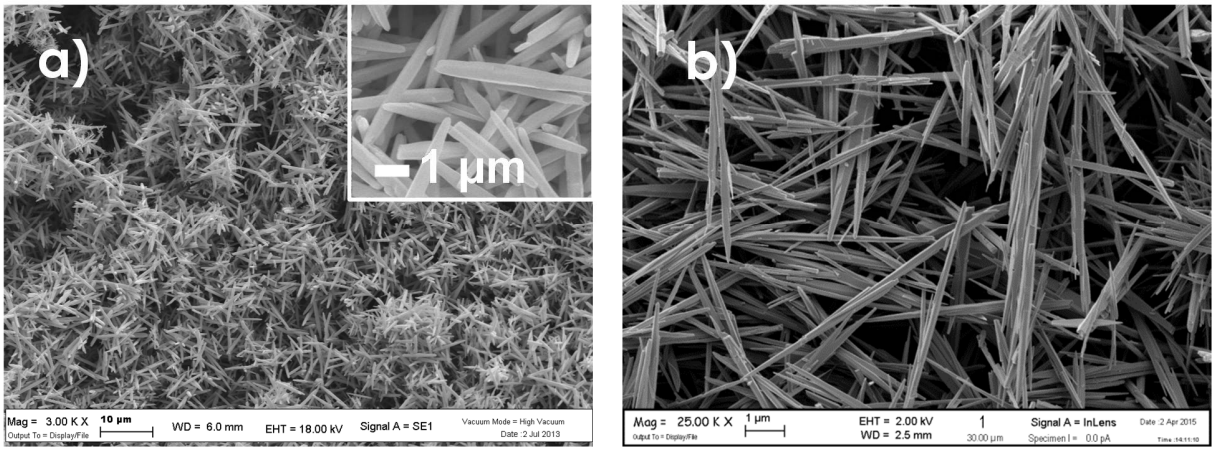

Fig. 3.7. SEM micrograph of short (a) and long needles (b).

An in-depth study about the effect of ultrasonic treatment onto the morphology and homogeneity of long needles has been carry out. Indeed, changing the time of the ultrasonic treatment, the aspect ratio as well as the homogeneity of the needles change.

The Fig. 3.8 shows a series of SEM images of as many samples thus obtained: the first five samples (up to 1 h of ultrasonic treatment) were obtained quenching the reaction by placing one drop of the reaction mixture on blotting paper to examine the morphology via SEM before to start the ultrasonic treatment, within 1 min, 5 min, 15 min, 60 min of ultrasonic treatment and finally the other samples were obtained after 3, 5, 7 or 9 h of ultrasonic treatment. The aim of this work has been to understand how the crystals start to grow in addition to the obtained best morphology. The result has been that the solid precursor was dissolved in the solution and contemporaneously ZnO in form of nano-needle precipitated. Indeed, it is possible to observe in the image referring to 5 min of treatment is the contemporaneous presence of

the precursor and of the nanocrystal of ZnO. Moreover, the best morphology was obtained for 7 h of treatment; this is a positive result, because an high aspect ratio has been obtained with the employment of ultrasonic starting from a solution without the aid of seems or growth substrates.

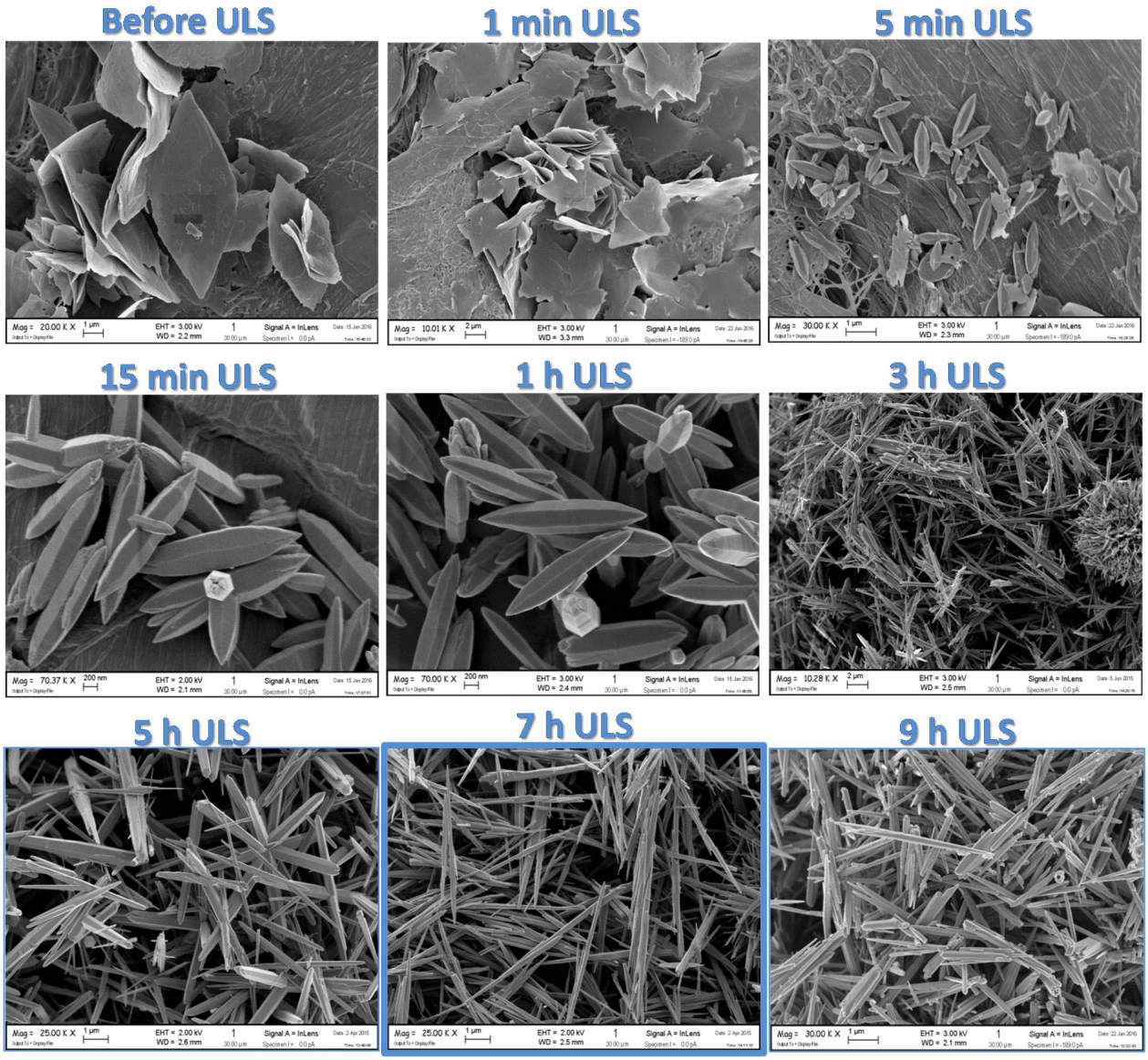

Fig. 3.8. Series of SEM micrographs showing the different stage of ultrasonic treatment to obtain long needles.

Prisms and flowers (EP and FL) - For the preparation of both morphologies, a water solution 0.1 M of $Zn(NO_3)_2 \cdot 6H_2O$ and one 0.05 M of hexamethylenetetramine (HMTA) were prepared and mixed under continuous stirring. A small amount (0.1 mol% with respect to $Zn(NO_3)_2 \cdot 6H_2O$) of polyethyleneglycol (PEG, MW = 400) was next added after mixing. The mixture was then kept at the temperature of 95 °C

for 7 hours in a muffle furnace to obtain flowers and in a ultrasonic bath in the case of prisms. The precipitate was filtered by gravity, washed several times with water and diethyl ether, before drying at 100 °C in air overnight in oven.

SEM analysis showed (Fig. 3.9 a) EP samples with aggregates of nanocrystals in shape of hexagonal prisms about 100 nm wide, while FL samples were characterized by micro flowers with petals shaped as hexagonal prisms, about 300-400 nm wide and 5-6 μm long (Fig. 3.9 b).

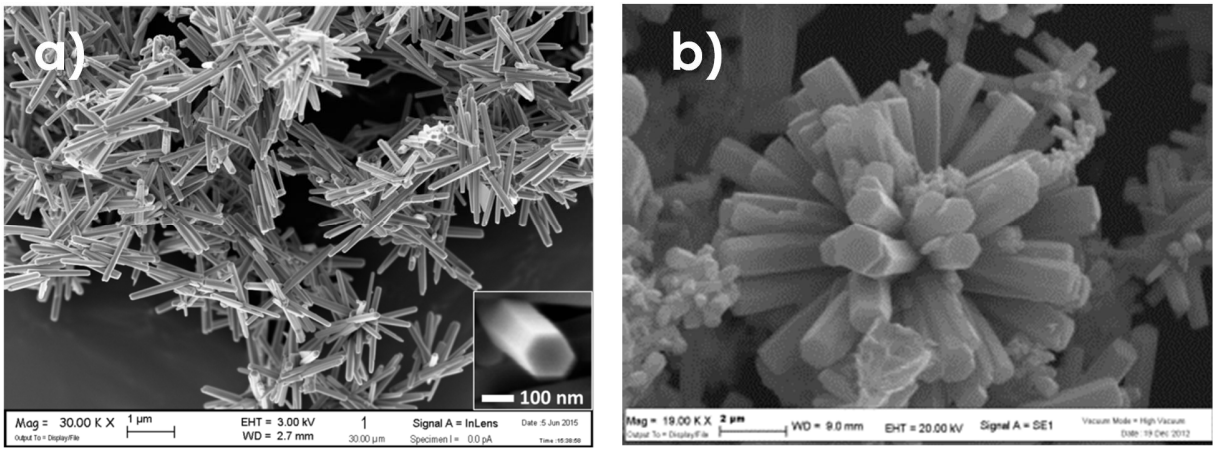

Fig. 3.9. SEM micrograph of the hexagonal prisms (a) and of the flower-like structures.

The growth of the flower-like structures could be explained taking into account a possible twinning plane $(80\bar{8}9)$, that is practically the plane $(10\bar{1}1)$. The $(80\bar{8}9)$ twinning plane in zincite was firstly reported in Dana's Series of Mineralogies [10].

3.3.1 Morphological dependence on ZnO-precursor

In the cases of nanosheets and bisphenoids, it must be highlighted a particularly important topic: they exhibit a crystalline solid precursor as intermediate synthesis product. Nanosheets and bisphenoids solid precursor, as confirmed by SEM (Fig. 3.10) and XRD analysis, crystallize as orthorhombic ε-$Zn(OH)_2$, space group $P2_12_12_1$ and parametric units cell a = 4.90500 Å, b = 5.14300 Å, c = 8.47300 Å. During the calcination process, the solid precursor changes into ZnO nanoparticles releasing hydroxide ions (OH^-) but maintaining the original shape and dimensions: ZnO in these cases behaves as a pseudomorphic material. The existence of a mineral with outward crystal form of another mineral species is known as "pseudomorphism" [10]. If a crystal of a mineral is altered so that the internal structure or chemical composition is changed but the external form is preserved, it is called a pseudomorph. Pseudomorph usually are further defined according the manner in which they were formed, as by substitution,

encrustation or alteration (partial addition or partial removal of original material). The ZnO pseudomorphism occurs for alteration as well as for example for $CaSO_4$ that becomes $CaSO_4*2H_2O$.

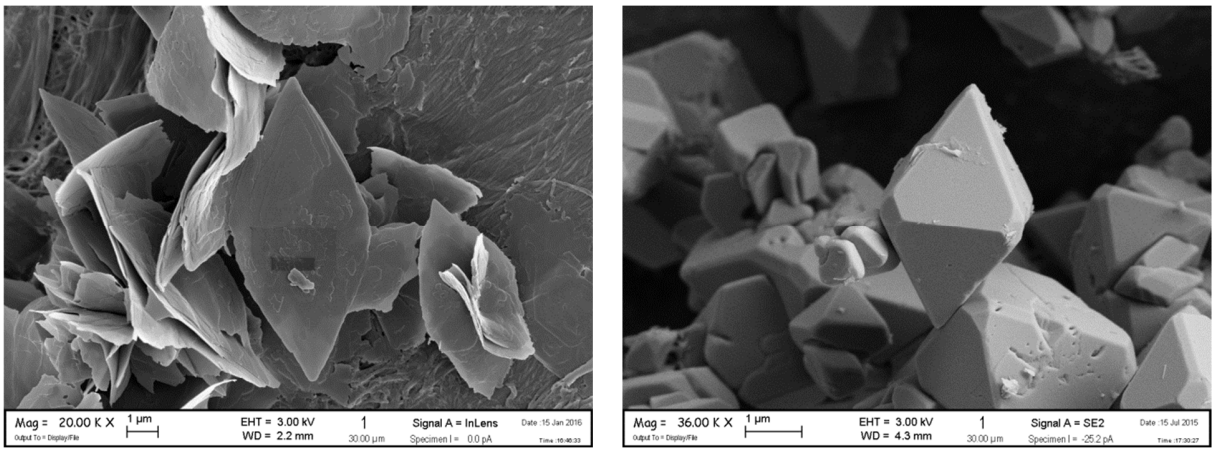

Fig. 3.10. SEM images of ZnO solid precursor for nanonosheets (a) and bisphenoids (b).

3.3.2 Structural characterization

All synthesized materials exhibited hexagonal wurtzite structure (space group $P6_3mc$) irrespective both on the synthesis method and the particle morphology, as shown in the XRD patterns (Fig. 3.11).

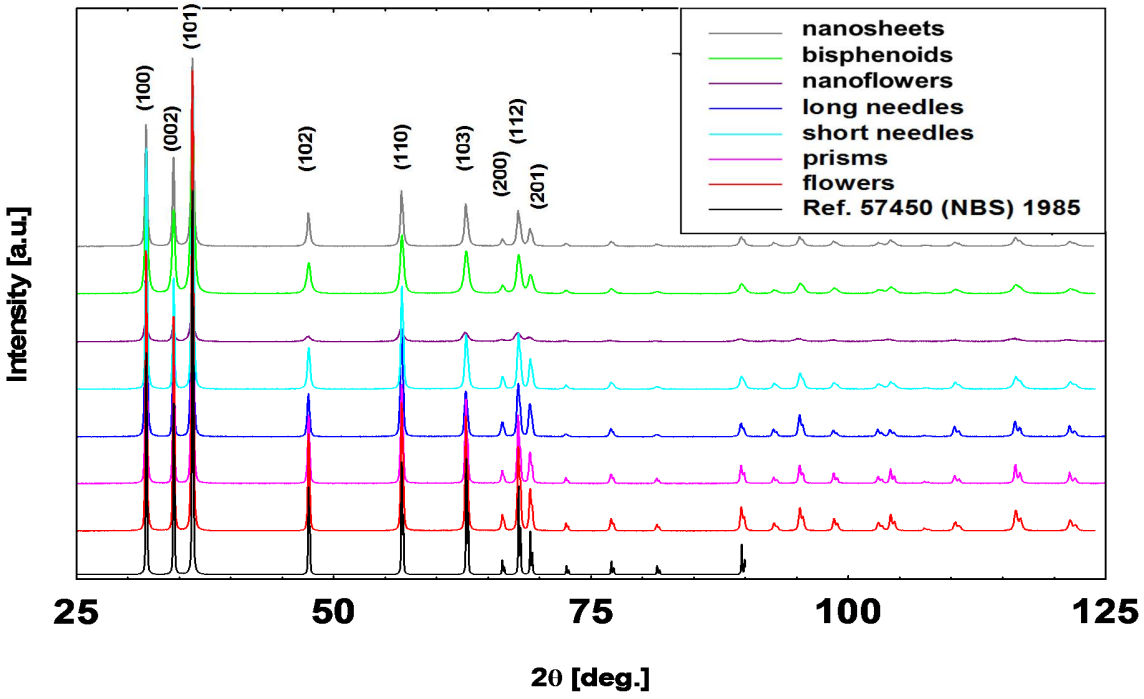

Fig. 3.11. X-ray diffraction pattern of all synthesized ZnO powders

In the table 3.1 the unit cell parameters, the volumes, the Bragg R factors and the grain sizes, evaluated by the Debye–Scherrer formula, are summarized. However, the crystallite sizes highlighted some differences. There is an apparent disagreement between the average crystallite size calculated by the Scherrer's formula and the SEM observations reporting images of monocrystals of several hundreds of nanometers. However, it must be taken into account that the estimation of the crystallite length through Scherrer's formula is the length of the almost perfect crystal. In fact, the rapid crystallization of the sample EP is usually accompanied by different defects, such as dislocations, stacking faults, etc. in a large quantity. Thereby, the average crystallite size can be considered as an average distance between the growth defects due to the rapid crystallization implied in the specific synthesis method.

Table 3.1 Values of the unit cell parameters: a, c, volume, Bragg R factor and grain size. In parentheses, estimated standard deviations to refer to the last digit.

Sample	Structure	a (Å)	c (Å)	Vol (Å^3)	R_B	(100)x(002) crystallite size (nm)	SEM image
Nanosheets NS	Wurtzite ($P6_3mc$)	3.2503(1)	5.2089(2)	47.66(1)	4.9	24 x 28	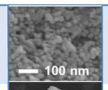
Bipyramds BP	Wurtzite ($P6_3mc$)	3.2502(1)	5.2082(1)	47.65(1)	2.2	28 x 21	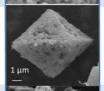
Nanoflower NF	Wurtzite ($P6_3mc$)	3.2548(1)	5.2143(3)	47.84(1)	10.9	23 x 34	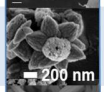
Short Needles SN	Wurtzite ($P6_3mc$)	3.2500(1)	5.2091(1)	47.65(1)	9.1	48 x 48	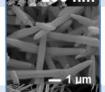
Long Needles LN	Wurtzite ($P6_3mc$)	3.2507(1)	5.2092(1)	47.67(1)	20	36 x 41	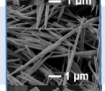
Flowers FL	Wurtzite ($P6_3mc$)	3.2499(1)	5.2062(1)	47.62(1)	3.1	49 x 49	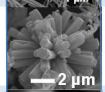
Prisms EP	Wurtzite ($P6_3mc$)	3.2533(1)	5.2123(1)	47.78(1)	5.6	46 x 52	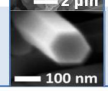

3.3.3 Spectroscopic characterization

The spectroscopic characterizations have been performed onto samples NS (nanosheets), LN (long needles) and EP (hexagonal prisms) because of they are representative of all studied samples. Indeed, NS, among the nanoparticle aggregates, exhibits particles with the lowest grain radius; LN, among the

bi-dimensional nanocrystals, shows smoothed borders, while the sample EP is composed of nanocrystals with highly defined surfaces.

Passing to the results, for sample EP (Fig. 3.12 b) the interaction with acetone causes the formation of the absorption related to free electrons in the CB. The band related to the photo-ionization of mono-ionized oxygen vacancies is not observed. This behavior distinguishes sample EP from the other samples, for which both the absorption related to free electrons and the band related to mono-ionized oxygen vacancies are observed (Figs. 3.12 a and c). The reason for the observed difference can be understood in the different morphologies of the samples: the presence of intrinsic surface defects, such as oxygen vacancies able to trap electrons, is guaranteed by materials showing badly defined crystallites with indented borders, such as samples NS and LN [11]. The highly defined mono-crystals of sample EP do not guarantee a sufficient amount of surface oxygen vacancies for IR detection.

Looking at samples NS and LN, the ratio between the intensity of the absorption related to free electrons and of the band related to mono-ionized oxygen vacancies is much higher in NS than in LN. For sample NS the band associated to oxygen vacancies is dominant, in agreement with SEM analysis that shows the presence of smaller and, as a consequence, more defective particles for this specimen. Moreover, observing the integrated intensity of the electronic absorptions, samples EP and NS exhibit higher values with respect to samples LN, in agreement with electrical measurements that reveal higher response to acetone for samples EP and NS, as reported below. Moreover, sample LN show the lowest electronic absorption intensity, well in agreement with the worst sensitivity to acetone (vide infra).

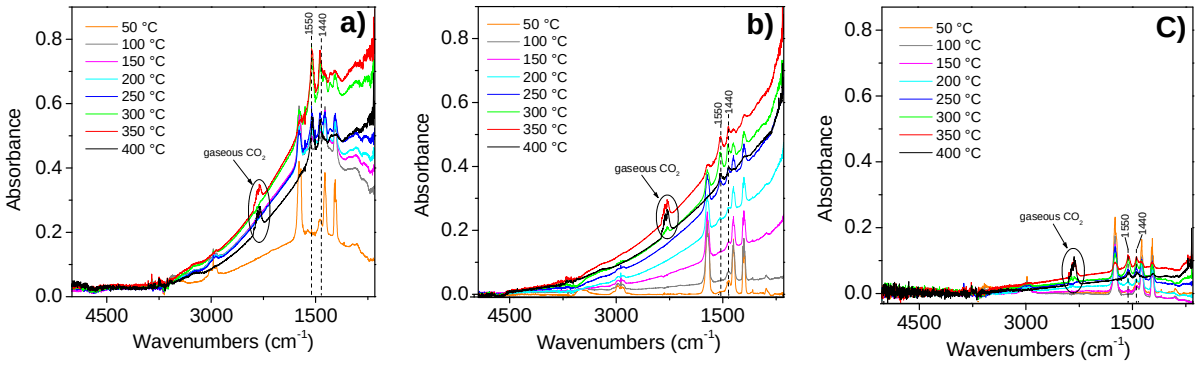

Fig. 3.12. FT-IR spectra of NS (a), EP (b) and LN (c) samples during interaction with a mixture acetone/O_2 (1:5, $p_{acetone}$ = 5 mbar) at increasing temperature up to 400 °C.

3.3.4 Electrical characterization

The Arrhenius plots, reported in the Fig. 3.13 A, evidence that all samples exhibit a n-type semiconductor-like behavior modulated by the Schottky barrier formation at gas-semiconductor interface, generally attributed to a negative surface charge accumulation, typically O_2^- and O^- ions. As regards the conductivity values, no particular difference between them can be found. However, a difference situation is offered by the measures of the height of the energy barrier in air and its trend as a function of temperature (Fig. 3.13 B). In fact, looking at the two types of morphologies separately, while the sample NS exhibits high energy barrier and high responses to reducing gases (see below), as usually happens in the Schottky barrier model, different is the situation of the samples EP and LN, for which this order is not observed. Indeed, although both samples are constituted by elongated nano-crystals, the energy barrier of EP sample is much lower and different in shape than the one of LN sample, being however the responses to reducing gases higher for the sample characterized by a lower barrier.

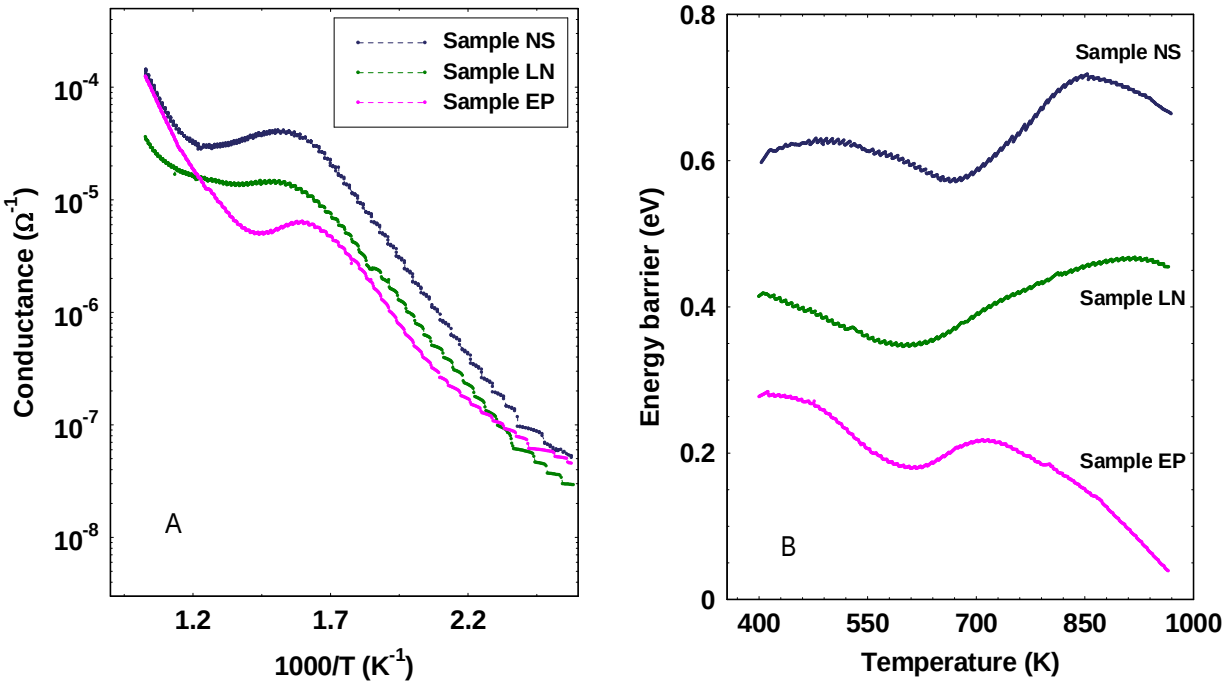

Fig. 3.13. Arrhenius plot (A) and energy barrier vs. temperature (B) for NS, LN and EP samples.

This fact can be also observed in the Fig. 3.14, where the comparison between the energy barriers in air and in 10 ppm of acetone is reported. In the figure, the difference between the height of the energy barrier measured in acetone and in air of the sample NS, is much wider than in the two samples

characterized by nano-crystal morphologies. It means that, in the sample characterized by nano-particle morphology, a great amount of electrons participates to the detection process, thus promoting the gas response. Looking at the behavior of the samples EP and LN, the sample EP, characterized by elongated nano-crystals in form of hexagonal prisms, exhibits a much wider difference between the energy barriers in air and in acetone than the sample LN, thus confirming what observed above. However, on the basis of the described results and on the Schottky barrier model, the differences between the barriers of the samples EP and LN are not explainable.

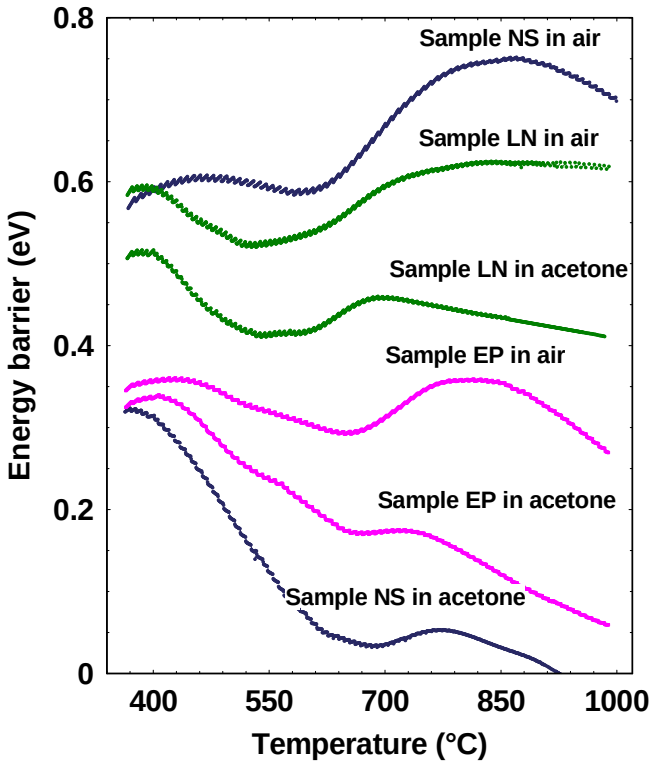

Fig. 3. 14. Comparison between the energy barrier dependence on temperature in dry air and in a mixture of dry air and acetone (10 ppm).

Observing the barrier of the sample EP, at first sight one might ascribe its low height to the effect of band-bending flattening [12-Ch.1]. However, the hexagonal prism size is certainly larger than the characteristic width of the depletion layer. The low energy barrier could instead be related to a low density of surface states, in particular due to a poor amount of surface oxygen vacancies. In fact, the hexagonal prisms of which the sample EP is constituted, exhibit highly crystalline surfaces that do not favor atomic adsorption. On the other hand, in FTIR measurements the interaction with acetone doesn't cause the formation of the band related to the photo-ionization of mono-ionized oxygen vacancies, but

only the absorption related to free electrons in the CB. This is probably the cause of the different behavior between the sample EP and the sample LN. Effectively, although both samples are formed by elongated nano-crystals, the needles of sample LN exhibit crystalline surfaces less defined and borders much less regular of the ones of the sample EP.

3.3.6 Sensing properties

Breath gas analysis has recently attracted much attention as a non-invasive detection of diseases in the evaluation of human health [12]. Detection and measurement of breath compounds have been obtained through several conventional techniques eg, mass spectrometry, gas chromatography-mass spectrometry (GC-MS), infrared (IR) spectroscopy, etc. However, low cost and easy to use devices such as solid state gas sensors should be an alternative to analytical techniques for analyzing the exhaled breath in real-time [13].

With this aim in view, all sensing films have been tested with respect to many gases, mainly versus acetone and other VOCs related to the breath gas analysis. Among them, formaldehyde, acetaldehyde, acetone, ethanol, toluene, isoprene and ammonia were the gases toward which the ZnO materials, synthesized for this work, showed the best performances.

In Fig. 3.15, the responses to 10 ppm of acetone, acetaldehyde, isoprene and toluene in dry air at the temperature of 450 °C are reported. Firstly, it can be noted that acetone is the gas to which all sensors exhibited the best responses. Moreover, for all gases, BP and NS sensors showed the best results, being they constituted by two different forms of nanoparticle aggregates: bisphenoids and nanosheets. Concerning the third (NF) of the nanoaggregate materials, its responses to all tested gases turned out much lower than those of NS and BP sensors. Effectively, the height and the trend versus temperature of the surface potential barrier (measure not reported here) were substantially different from the other nanoaggregates. On this sample, a specific surface area (SSA) was determined by applying the Brunauer-Emmett-Teller (BET) method to understand if the hierarchical structure remained inside the whole sample. It resulted SSA = 2.6 m^2/g, while for the sample NS, SSA = 19 m^2/g. it means that the sample NF is constituted of nanoparticle aggregates, however the particles are not separated between them, but forming a “crystallographic continuum”.

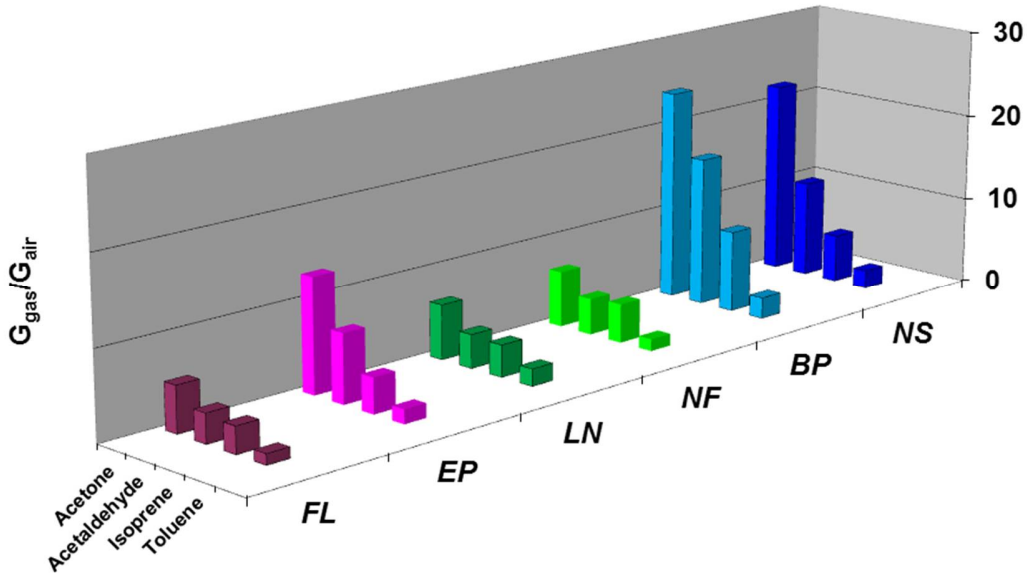

Fig. 3.15. Comparison of the responses to 10 ppm of acetone, acetaldehyde, isoprene and toluene in dry air at the temperature of 450 °C for all tested samples.

Moving to the acetone characterization, the responses of all sensors at all tested working temperatures are reported in Fig. 3.16. Again, it must be highlighted the difference of performance between the sensors in which the functional material is constituted of aggregates of nanoparticles and the sensors based on bidimensional nanocrystals.

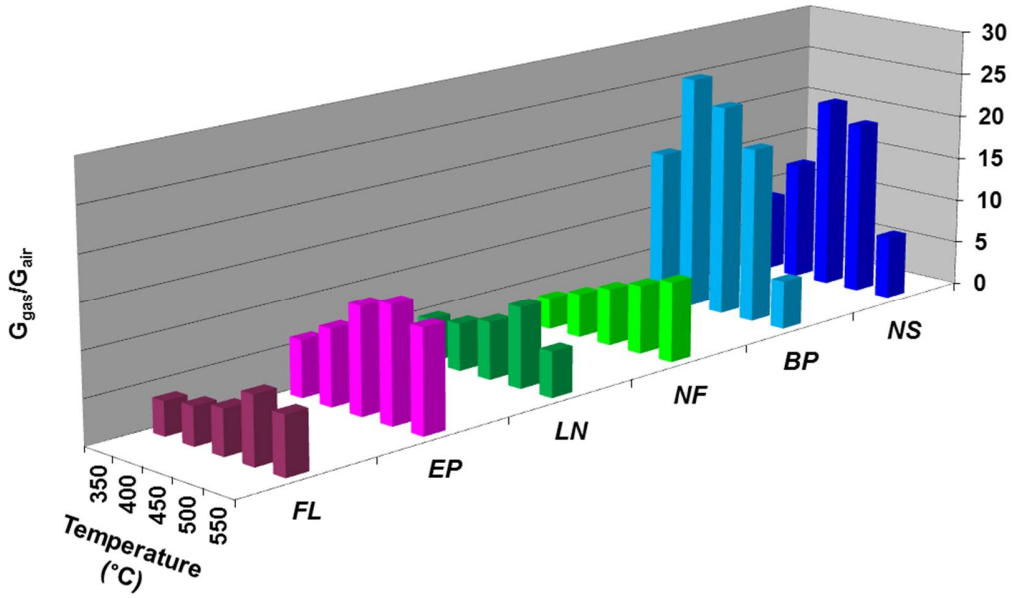

Fig.3.16. Responses to 10 ppm of acetone in dry air as a function of the working temperature.

In Fig. 3.17, a series of responses to 1 ppm of acetone in dry air at the operating temperature of 450 °C for BP, LN, NF and FL sensors is reported. This result allows to consider ZnO nanoparticle aggregates as functional materials suitable to detect acetone at sub-ppm level.

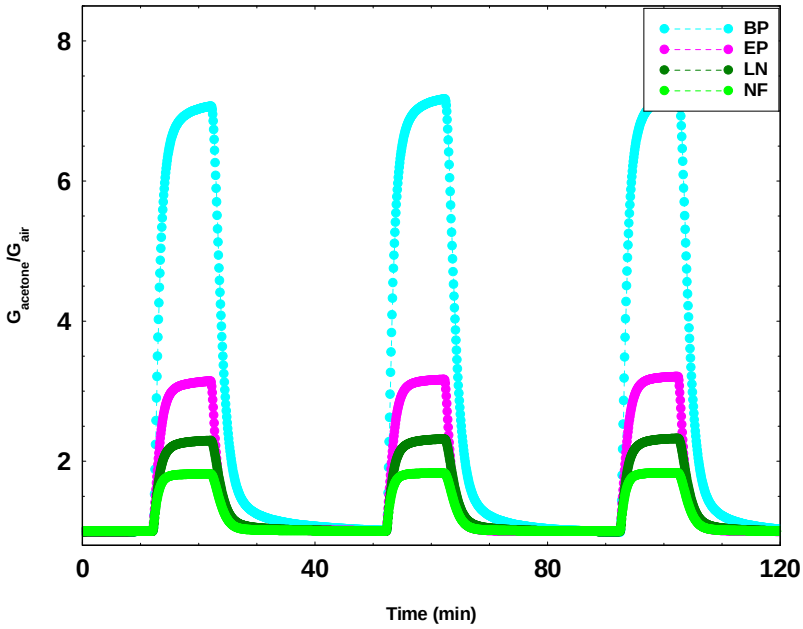

Fig. 3.17. Series of responses to 1 ppm of acetone in dry air at the operating temperature of 450 °C for BP, LN, NF and FL thick films.

To verify that the sensors are able to detect acetone at sub-ppm level, calibration curves have been performed at acetone concentrations ranging between 0.1 and 2 ppm. In Fig. 3.18, such calibration has been carried out for BP sample resulting that acetone can be detected at concentrations down to 20 ppb.

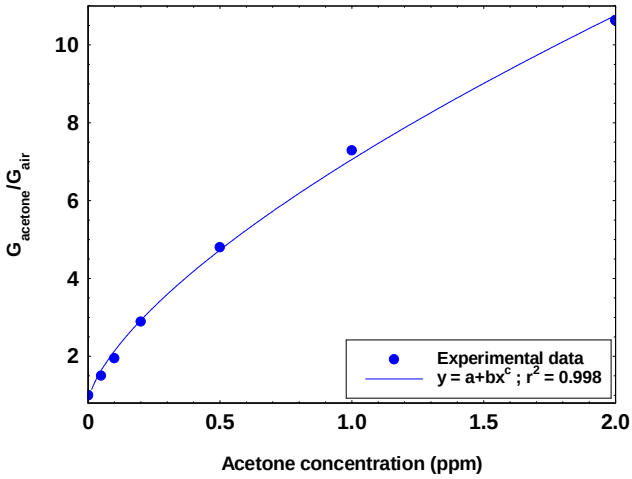

Fig. 3.18. Acetone calibration curves for the all tested sensors

Moreover, response and recovery times (RRTs) are a crucial point to realize an effective device with optimal performances; in this respect, few test chambers in series with different volumes have been used, resulting that RRTs are more dependent on the chamber volume than the sensor characteristics. Indeed, more the test chamber volume is reduced, more the RRTs resulted lowered, as shown in the Fig. 3.19 for BP sensor measured in the test chambers with the largest and smallest volumes. In particular the RRTs in the largest chamber resulted 182 and 240 s, respectively, while in the smallest chamber RRTs resulted 40 and 80 s.

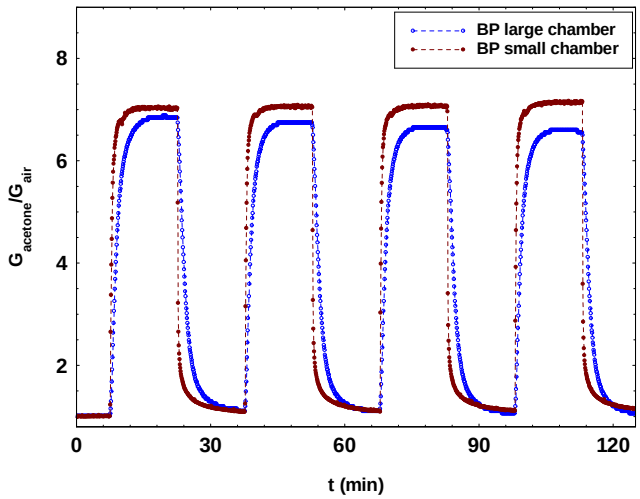

Fig. 3.19. Comparison between the response of the BP sensor in the test chambers with the largest and smallest volumes.

REFERENCES

[1] United states geological survey, *Series A, Economic geology*, 24, Bulletin 213, (1902).

[2] T. Seiyama, A. Kato, K. Fulishi, M. Nagatani, (1962), *Anal. Chem.*, 34, 1502-1503.

[3] I. T. Drapak, *Semiconductors*, vol.2, pp. 624–625, 1968.

[4] Ü. Özgür et al., *J. Appl. Phys*. 98, 041301 (2005).

[5] B. Meyer, D. Marx, *Phys. Rev. B* 67 035403 (2003).

[6] Z. L. Wang, *J. Phys.: Condens. Matter*, 16, R829 (2004).

[7] W.-J. Li et al., *Journal of Crystal Growth* 203 (1999) 186-196.

[8] C. Suryanarayana, C.C. Koch, *Hyperfine Interact.* 130 (2000) 5–44.

[9] Sheng Xu, Zhong Lin Wang, *Nanoresearch* 11(2011) 1013-1098.

[10] C. Klein and C. S. Hurlbut jr., Manual of Mineralogy (after J.D. Dana) 1999 – 21° edition John Wiley and Sons, Inc.

[11] A. Chiorino, G. Ghiotti, F. Prinetto, M.C. Carotta, G. Martinelli, M. Merli, Characterization of SnO_2-based gas sensors. A spectroscopic and electrical study of thick films from commercial and laboratory-prepared samples, Sens. Actuators B: Chem. 44(1-3) (1997) 474-482.

[12] K.-H. Kim, Shamin Ara Jahan, Ehsanul Kabir, A review of breath analysis for diagnosis of human health, Trends in Analytical Chemistry 33 (2012) 1-8.

[13] Il-Doo Kim, Seon-Jin Choi, Sang-Joon Kim and Ji-Su Jang (2015): Exhaled Breath Sensors. In: C.-M. Kyung (ed.), Smart Sensors for Health and Environment Monitoring, KAIST Research Series, DOI 10.1007/978-94-017-9981-2_2.

CHAPTER 4

NOVEL METODOLOGIES FOR ON-LINE MONITORING THE HYDRAULIC OIL AGEING

4.1 INTRODUCTION

This innovative research (currently on patent stage) is concerning the use of a new methodology for the continuous monitoring of hydraulic oil aging the based on its vapor analysis by using MOX sensors. In this contest, also a novel employment of organic electrochemical transistors has been studied with the aim to develop a new device for the monitoring of the hydraulic oil on-board in real time.

In the frame of the fluid power system, the fluid must be considered as a real extended component, that closely interacts with the others and carry out two important task: the lubrication and the power transmission. The liquid, commonly employed in the fluid power system, is an oil derived from a mineral source and supplemented with suitable additives (antioxidants, anti-rust, anti-foam, etc.) to improve its characteristics. The main cause of failure in fluid power systems or machines is the degradation of the hydraulic oil caused by temperature, friction, contaminated by particles and presence of water. A failure involves a drop in machine reliability, an injection in the ambient of pollutant material (leakage of hydraulic oil) and a not planned stop machine.

Nowadays, there aren't sensor devices on-board for the monitoring the ageing of the hydraulic oil in real time. In general, oil samples are collected on-site from the machine and analyzed through portable systems or in an external laboratory using conventional methods and instrumentation (Brookfield viscometer, Karl Fischer method, spectroscopy (FTIR), thermal analysis (DSC), micro-analysis of particulate, analytical ferrography, etc.). The hydraulic oil is a complex system and it is characterized by a large number of necessary chemical-physical properties (viscosity, density, dielectric constant, oxidation level, acid grade, additives concentration, color, etc.) which change simultaneously with the oil ageing. For this reason, the monitor of oil degradation is a difficult and indirect procedure through the measure of at least one of these quantities.

The monitoring of the fluid conditions in hydraulic circuits is certainly a theme continuously evolving and of significant interest, as the European project SuperSkySense [2] demonstrate.

The market offers a series of sensors based on the measure of traditional oil related quantities (generally, motor or hydraulic oil) which can be implemented on-line with aiming to monitor the oil conditions. Some examples of these sensors are:

- Oil Quality Sensor (OQS) sold by RMF Systems (measure of the electrical constant) [3],
- HYDACLab® Oil condition sensor sold by HYDAC (measure simultaneously the presence of water, the electrical constant, and the temperature) [4],
- Oil Condition Sensor OCS sold by STAUFF (measure the presence of water, and the oxidation) [5],
- Fluid Property Sensor - FPS2810B12C4 sold by TE Measurement Specialties (measure simultaneously the viscosity, the density, the electrical constant, and the temperature) [6],
- LDP100 sold by IFM ELECTRONIC [7] as an example of particles counter (based on optical measure).

Furthermore, a compact, on-line and in real time monitoring device, MONITOIL [8], is commercially available sold by MECOIL. MONITOIL is based on traditional sensors (pressure, humidity, density, etc.) and it can be employed occasionally because of their complexity and the price range. This innovative research (currently on patent stage) is concerning the use of novel methodologies for monitoring on-board in real time the aging of the hydraulic oil based on its vapor analysis by using innovative sensors (MOX and Textile-OETCs).

4.2 HYDRAULIC OIL SAMPLE COLLECTION: TEST BENCH

The oil samples, (oil type: JOHN DEERE – HY-GARD JDM J20C) have been aged and collected using an hydraulic test bench developed at IMAMOTER (see Fig 4.1) and directly in a John Deere agrimotor. The hydraulic test bench, shown in Fig 4.1, is composed of the following parts: an electronic control, an electric motor, a pump, a heat exchanger, a 30 liters tank, a temperature sensor and a level one. The test bench has been realized to work continuously, rapidly ageing the oil, under controlled conditions also excluding the external agents contamination. The sampling of the oil has been carried out for the agrimotor from 0 to 1500 hours (steps of 250 h), while from 0 to 3000 hours (steps of 250 h) with the test bench to better understand the changes of the oil properties as a function of ageing. It has been chosen 1500 hours as highest ageing because it corresponds to oil change specifications reported in operating manual of the John Deere agrimotor.

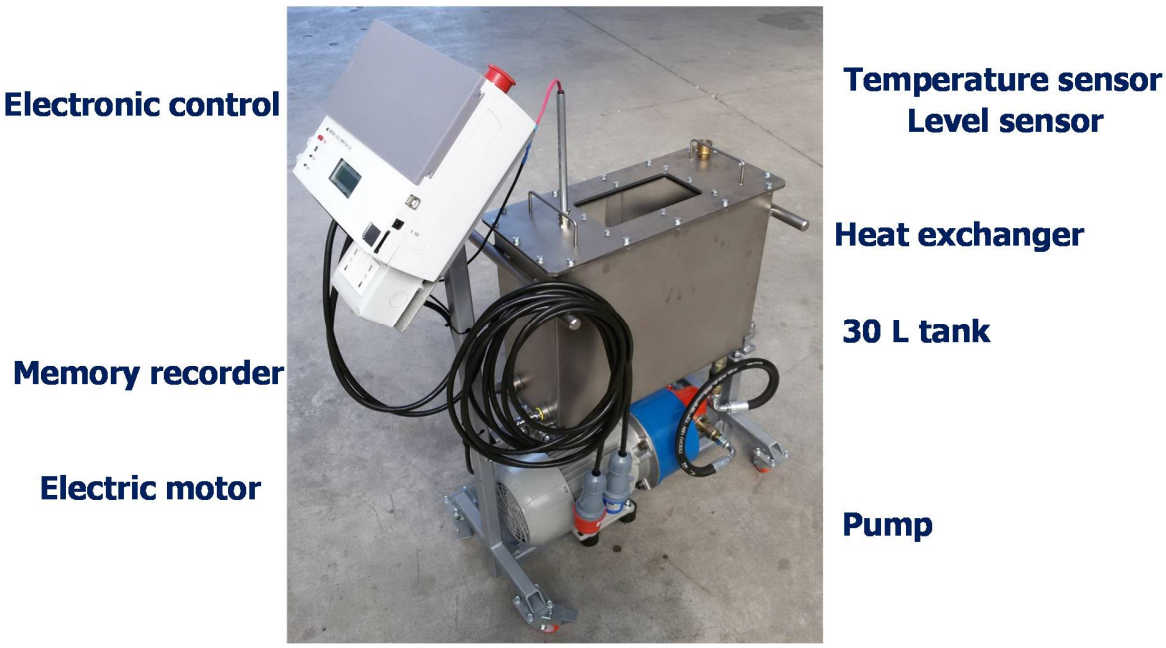

Fig. 4.1. Hydraulic test bench to age oil.

4.3 GAS CHROMATOGRAPHIC ANALYSIS

The gas chromatographic analysis has been carry out at University of Parma in collaboration with Prof. Federica Bianchi. The analysis of volatile compounds has been performed by using a gas-chromatograph HP 6890 Series Plus, Agilent Technologies (Milano, Italia) and a mass spectrometer MSD 5973 Agilent Technologies as detector. The chromatograms have been obtained after extraction of volatile fraction through static head space using GC-MS technique which separates and identifies the single volatile compounds. The identification has been performed comparing the mass spectrum of each pick of the chromatogram with the mass spectra in data base Wiley 275. It resulted that both compound with greater polarity such as aldehydes, ketones and alcohols, and with not polar compounds such aliphatic hydrocarbons. The number of compounds was twelve, reported in the table 4.1 with their ritention time (RT).

It has been observed a decreasing of the identified volatile compounds, increasing the oil aging; in particular, this is evident in the responses relating to light alcohols, such as 2-metil-1-propanol and 2-metil-1-butanol and also 1-pentanol and toluene.

Table 4.1 Analytes in headspace of hydraulic oil.

RT (min)	Analyte
2,24 (variable 2)	2-methyl-1-propanol
4,32 (variable 3)	2-methyl-1-butanol
5,11 (variable 4)	toluene
5,22 (variable 5)	1-pentanol
11,66 (variable 6)	2-ethylhexanal
12,51 (variable 7)	phenol
13,11 (variable 8)	decane
13,77 (variable 9)	4-methyldecane
13,98 (variable 10)	2-ethyl1-hexanol
16,00 (variable 11)	undecane
18,63 (variable 12)	dodecane
22,84 (variable 13)	camphene

A second phase was devoted to the principal component analysis (PCA) to verify the presence of clusters between the various samples. The first two components have been able to explain the 97% of the variance. In the Figs. 4.2 and 4.3 the score plot and the loading plot obtained through the analysis of hydraulic oil samples obtained from the test bench in the range 0 – 3000 h of aging.

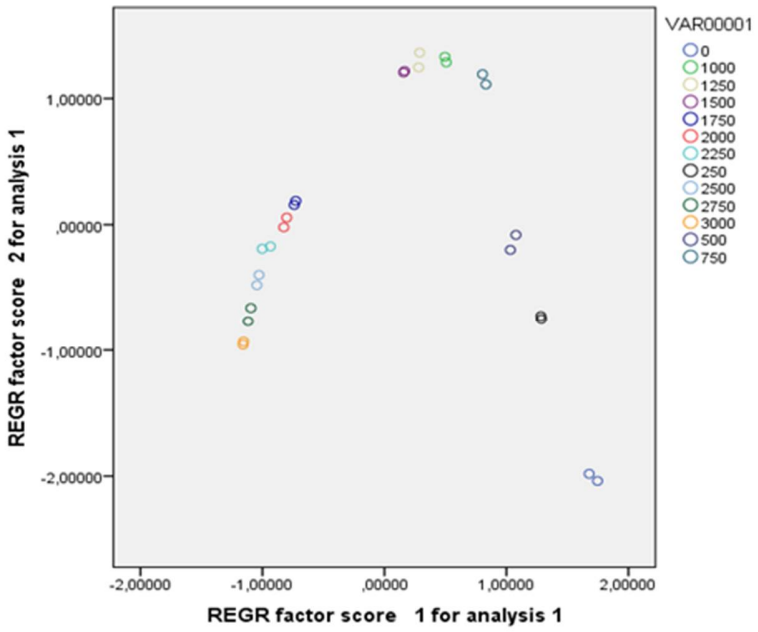

Fig. 4.2. Score plot

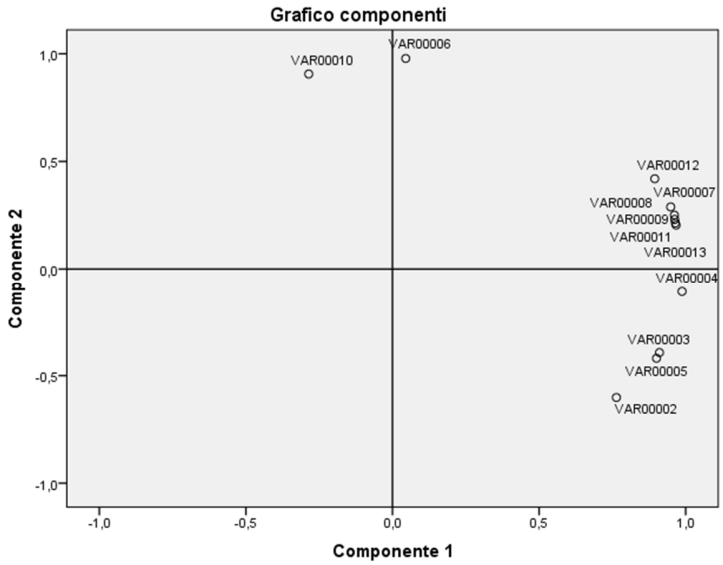

Fig.4.3. Loading plot

The loading plot reported in Fig. 4.3 represents the distribution of the volatile compounds (variables from 2 to 13) in the space of the principal components. It resulted that all variables , except 6 and 10, corresponding to 2-ethylhexanal e 2-ethyl-1-hexanol are more present in medium aged samples, while more aged samples (>1750h) are characterized by a low content of all variables.

4.4 MOX SENSORS SYSTEM

It is well-know that hydraulic oil exhibits a strong and characteristic odor that becomes sour and putrid with the ageing. The basic idea is the research of a correlation between the variation of the oil headspace and their ageing by using an indirect, easy and versatile technique based on thick film gas sensors. In literature are present some research related to this methodology: sensors for on-line monitoring [9], water sensors in hydraulic oils [10], instruments (for example gas chromatograph, electronic nose) to analyze the headspace of lubricant oils [11], MOX sensors to detect diesel oil in lubrican oils [12], etc.. However there aren't research works focused on the correlation between the headspace di of hydraulic oil and their ageing detected by using MOX sensors.

The methodological innovation, the laboratory system and the miniaturized device are aimed to the a continuous monitoring, on board of every machine, of the hydraulic oil aging through the vapor

analysis. This is made by a system of thick film gas sensors based on nanostructured semiconductor metal oxides. To carry out the laboratory tests, a system based on an array of nanostructured semiconductor oxide gas sensors was expressly realized for this aim. The laboratory system is constituted of a box to lodge the sensors(in Fig. 4.4 the MOX sensors monitoring unit used for this research in which are lodged three sensors), the electronic circuitry of each sensor, the main electronic control unit, the firmware, the software to record the sensor electrical signals in addition to a system to carry the vapor oil through the sensor box (schematic diagram in Fig. 4.2 and laboratory system realized Fig. 4.3).

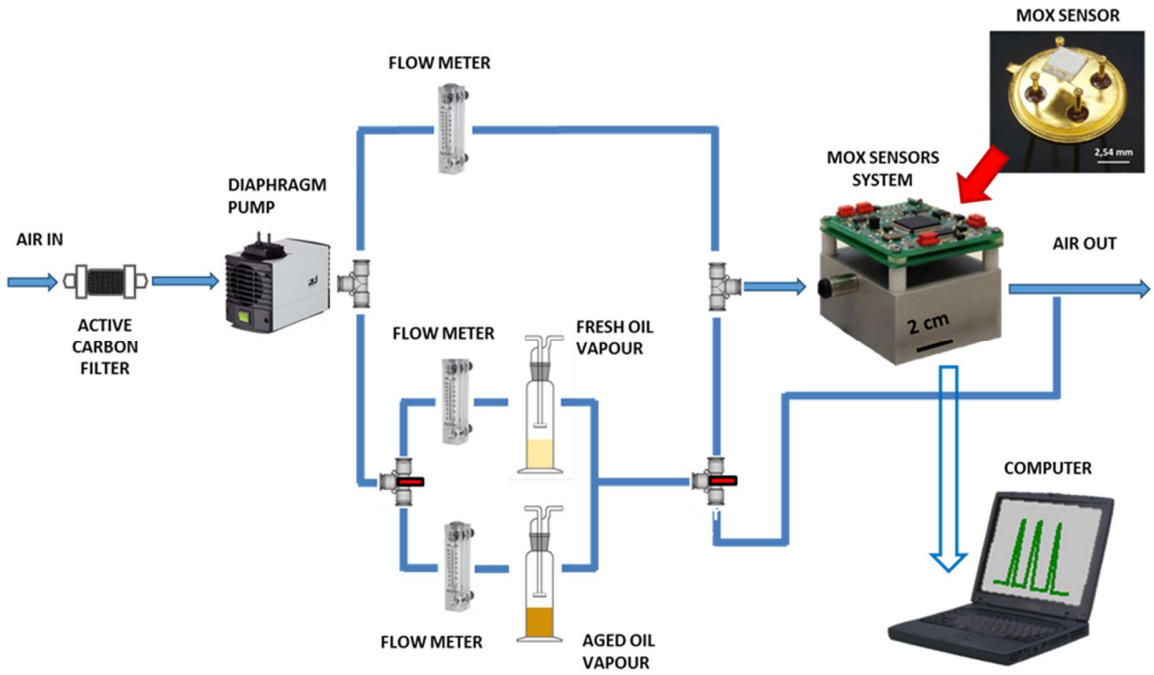

Fig. 4.2: Schematic diagram of laboratory MOX sensors system.

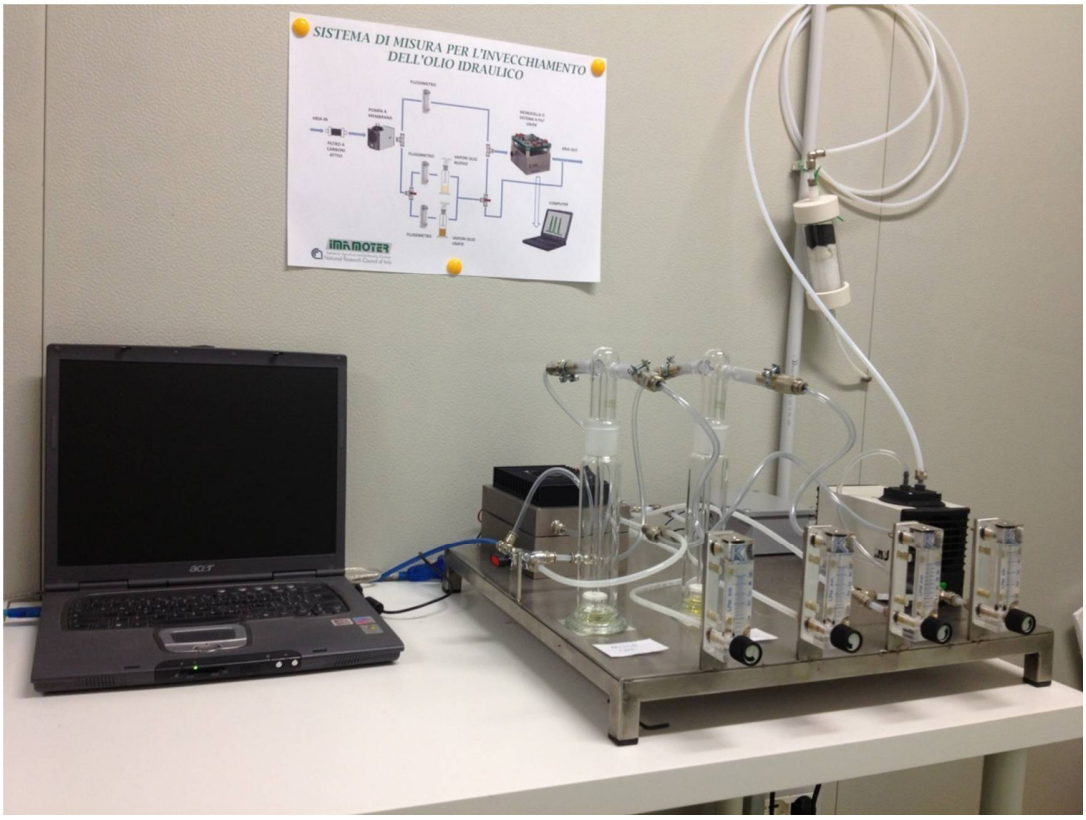

Fig. 4.3: Laboratory system realized at CNR-IMAMOTER for the monitoring of hydraulic oil ageing.

Fig. 4.4. MOX sensors monitoring unit in with are lodged three sensors.

The sensor response is defined as ratio between the conductance in presence of the target gas (in this case the oil vapor) and the conductance in air. An example of dynamic response is reported in the Fig. 4.5 A. The sensor response can be correlated with the aging of the oil carrying out a proper calibration using the laboratory system. In particular, the sensor responses are obtained testing a series of oil

samples at different degree of aging, namely at different number of working hours (from 0 to 3000 h with steps of 250 h).

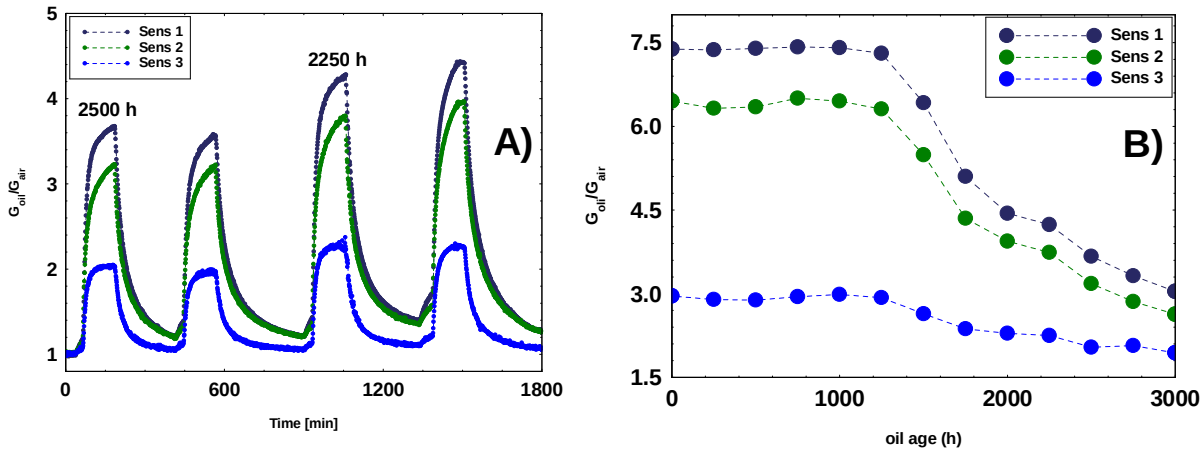

Fig. 4.5. Dinamical rensponses of three sensors based on different functional materials toward the same type of oil aged 2500 and 2250 hours respectively (A). Responses to a series of oil samples aged from 0 to 3000 h (step 250 h) for the same three sensors (B).

For all sensors the response to fresh oil vapor is higher than the response to aged oil vapour in agreement the less concentrations of analytes in the more aged samples, as shown in Fig. 4.5 B. At about 1500 hours of ageing a sudden decreasing of sensors response occurs. This is in agreement with oil change specifications reported in operating manual.

This type of correlation shall be used directly on the machine. Until now, the measurements have been carried out using oil samples at ambient temperature. In these test conditions, the sensor response values were in the range 1 – 10. Since the oil, in the usual working conditions, reaches an average temperature of 90°, the tests will be also performed on the heated oil samples with the aim to have responses more separated between fresh and aged oil.

The field of application is wide, mainly devoted to mobile machines (agricultural earthmoving machines). However, it can be extended through appropriate adjustments to automotive one for engine oil check.

4.5 ORGANIC ELECTROCHEMICAL TRANSISTORS (OETCs)

Organic electrochemical transistors (OECTs) are emerging as a possible solution in biosensing or chemical sensing applications thanks to their low cost, flexible, small dimensions, non-invasive and easy to read features. So far OECTs have been applied as sensors both for simple analytes such as hydrogen peroxide [13] and ions [14] and with more complex bio-structures such as micelles [15], liposomes [16] and DNA [17]. Recently, innovative approaches for the functionalization of materials of industrial interest have been improved in different applications. In particular textile cotton yarns substrates (natural cellulose) have been used to realize conductive fibers, which have been applied as innovative textile-integrated sensing devices. The peculiar properties of the textile, allow a simple and economic integration of the device in different industrial systems, and furthermore to naturally absorb water based fluids. The output characteristics of Textile-OECT have been demonstrated for the first time using a solid or gel electrolyte for ionic exchange, successively a direct application in liquid solutions detection has been realized [18].

A Textile-OECT is generally made of a thin film of conducting polymer, deposited on a textile fiber, in contact with an electrolyte and a gate electrode immersed in it. The most used polymer is p-type conductive poly(3,4-ethylenedioxythiophene) doped with poly(styrene sulfonate) (PEDOT:PSS), a degenerately doped p-type conductive polymer. The drain current (I_{ds}) is generated by the application of a source–drain voltage (V_{ds}) at channel terminals, which drives holes along the polymer backbone. The OECT channel is defined by the region where the electrolyte overlaps the PEDOT:PSS film, so that ionic interchange between the electrolyte and the polymer may take place (Fig. 4.7).

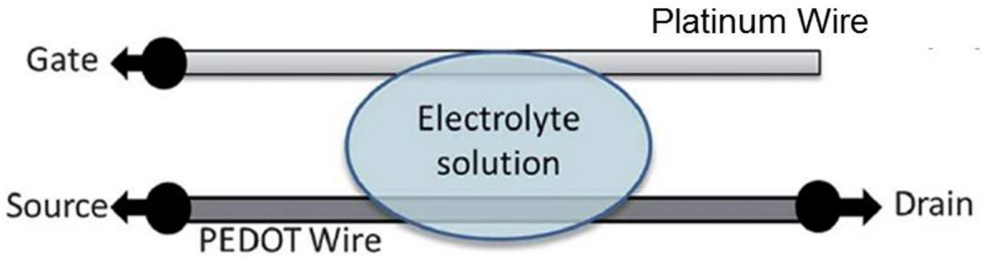

Fig. 4.7. Diagram of a cotton-OECT (adapted from [18]). The overlapping between the liquid electrolyte and the PEDOT:PSS wire defines the OECT channel while the platinum wire in contact with the electrolyte acts as the gate.

The gate electrode could be realized by a metal wire immersed in the electrolyte, for example silver (it gives sensitivity only to ions) or platinum (it gives sensitivity also to organic molecules). Upon application of a positive gate voltage (V_g), cations in the electrolyte are forced toward the PEDOT:PSS film, drift in the polymer and de-dope it according to the following equation:

$$PEDOT^+:PSS^- + M^+ + e^- \leftrightarrow PEDOT + M^+:PSS^-$$

where M^+ represents the cations. This will deplete the number of available carriers and hence, as a consequence, the source–drain current (I_{ds}) decreases.

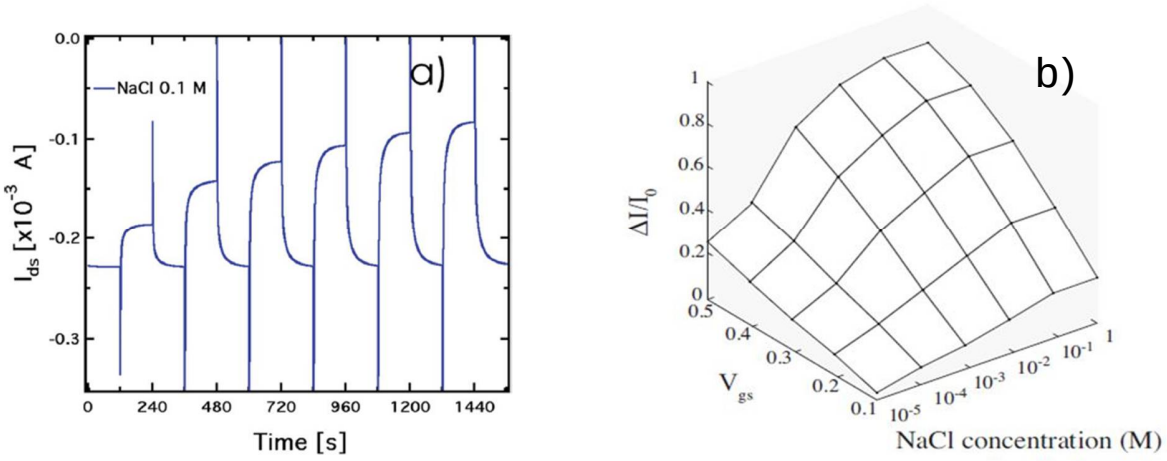

Fig. 4.8. Plot of the drain current (I_{ds}) modulation in a cotton-OECT using a 0.1M NaCl electrolyte solution and pulsing the gate voltage between 0 V and 0.4 V with 0.05 V steps (a). Adapted from [18]. Plot of the normalized response ($\Delta I_{ds}/I_0$) of the transistor as a function of the salt concentration at different gate voltage (b).

Fig. 4.8 a shows an example of the modulation of the drain current (I_{ds}) in a cotton-OECT using a 0.1M NaCl electrolyte solution and pulsing the gate voltage between 0 V and 0.4 V with 0.05 V steps. In Fig. 4.8 b it is reported the normalized response ($\Delta I_{ds}/I_0$) of the transistor as a function of the salt concentration in the range 0.1–100 mM at different gate voltage. Therefore, the response of the sensor depends both from the ionic concentration of the electrolyte solution and from the value of V_g.

Textile-OECTs monitoring the hydraulic oil ageing - In this work a novel employment of Textile-OECTs has been studied. The basic idea is the monitoring of the hydraulic oil ageing in real time and on-board through the organic electrochemical transistors because of their advantageous properties: low cost, small dimensions, easy to read, long term stability and reversible use. The textile structure of the

device could be used to absorb spontaneously the fluids and measure their electrochemical properties, in simple and direct way without the employment of a microfluidics system.

The hydraulic oils, being non-polar fluids, cannot work as an electrolyte solution. For this reason, a new challenging procedure has been developed and tested to extract from the oil, small molecules with an hydrophilic behavior. The extraction process consists of:

- the addition of a proper amount of distilled water to the oil sample,
- the mixing of the two liquids,
- the rest of the emulsion, and
- the sampling of the water in which molecules are moved from the oil.

The analysis of the water extracted enables the monitoring of the hydraulic oil ageing through the organic electrochemical transistors. The developed device can prevent the breakdown in hydraulic machines, a direct consequence of the hydraulic oil degradation, providing a new solution for the predictive maintenance.

Cotton-OECT preparation and characterization – The cotton-OECT device, used in this work, has been fabricated at CNR-IMEM. The cotton fiber (the yarn) (Fig. 4.9 a, b) has been functionalized by a simple soaking process: the yarn was immersed into an aqueous solution of PEDOT:PSS (Clevios PH500, Starck GmbH) for 5 min, followed by baking on a hot plate at 150 °C for 3 hours (Fig. 4.9 c, d).

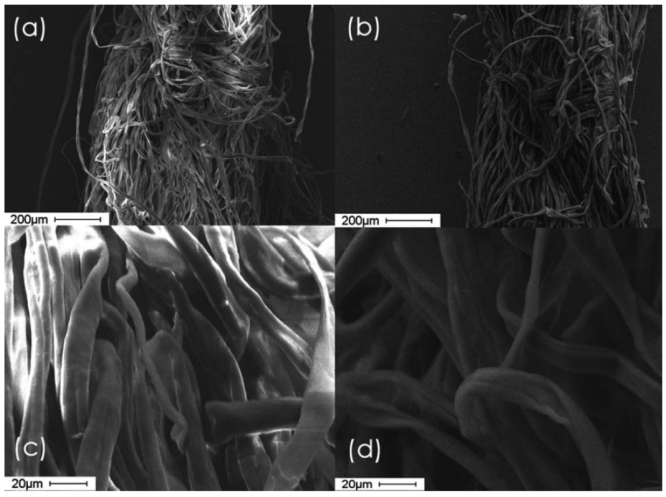

Fig. 4.9. SEM images of the natural cotton thread acquired by a scanning electron microscope (a) at 75 X and (c) at 600 X; and images after PEDOT:PSS functionalization (b) at 75 X and (d) at 600 X (adapted from [18]).

The PEDOT:PSS solution was previously modified with addition of ethylene glycol (20%) and dodecyl benzene sulfonic acid (DBSA) surfactant (5 %) in order to increase electrical conductivity and decrease solubility in water. The measured electrical resistance of the as-prepared yarn was 430 Ohm over a linear length of 1 cm; this value allows the use of voltages in the mV range. The gate electrode is realized by using a platinum spiral wire to increase the surface available for the sensing. The device was typically operated with a maximum gate voltage of 1 V to avoid water electrolysis.
The transistor characteristics were evaluated using a 2 channel source/measure precision unit Agilent B2902A, controlled by a LabView software developed at CNR-IMEM.

Samples preparation - Four oils (type: John Deere – Hy-Gard JDM J20C) at different hours of ageing (0, 250, 500 and 1000 hours) have been choose, among the oils collected during the agrimotor work, to test the device. A particular attention has been paid to prepare the samples because hydraulic oils are non-polar fluids and hence they don't work as an electrolyte solution, as stated before. To carry out oils characterization by means of fiber OETCs, oil-ultrapure water (1:3) emulsions was prepared through different procedures:

1) stirring at RT for 20 min,
2) performing an ultrasonic treatment for 20 min at RT,
3) stirring for 20 min, then performing an ultrasonic treatment for 20 min both at RT,
4) adding a small amount of cetyltrimethylammonium bromide surfactant and shaking for 30 s.

After the treatments, the waters have been extracted with the aim to study the analytes moved from oil to water during the mixing process. The better preparation method resulted the third and the obtained emulsions are shown in Fig. 4.10.

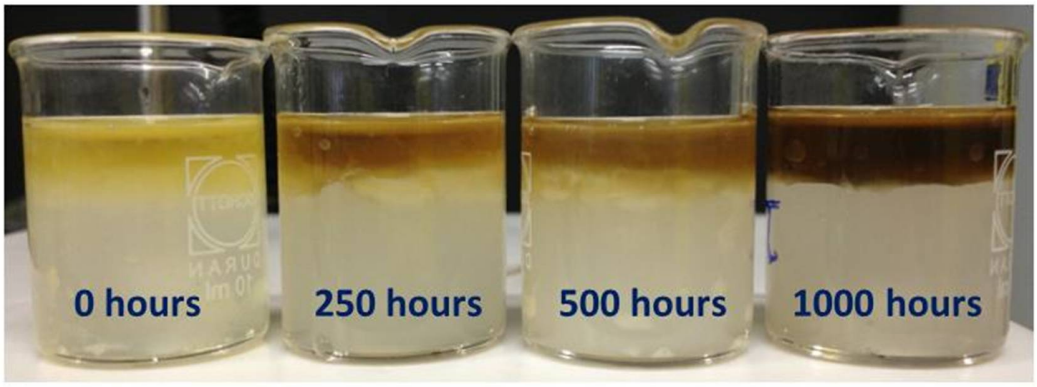

Fig. 4.10. Oil-water (1:3) emulsions of the selected 4 oils at different hours of ageing (0, 250, 500 and 1000 hours).

4.5.1 Experimental results

The following characterizations have been carry out using the samples prepared following the third procedure (stirring for 20 min, then performing an ultrasonic treatment for 20 min both at RT).
The extracted waters have been firstly analyzed trough gas-chromatography to verify the presence of substances moved from oil to water and their chemical nature. To perform the analysis, the water has been extracted further with heptane from the samples. The same chromatographic profile resulted for all samples, for which only few analytes have been found (see Table 1).

RITENTION TIME (min)	ANALYTE
3.6	Heptane (residual)
11.8	Phenol
14.0	2-Ethyl-1-hexanol
16.6	2-Ethylhexanoic acid

Table 1: List of analytes detect from moved from oil to water during the mixing process.

The characterization trough cotton-OECT has been realized by measuring source–drain current (I_{ds}) *versus* time at a constant drain voltage (V_{ds} = -0.5 V) while varying the gate voltage between 0 V and 1.0 V (V_{gs} step of 0.2 V). The measure has been performed firstly for ultrapure water (Water i), then for the waters extracted from the emulsions (0, 250, 500 and 1000 hours) and finally for ultrapure water (Water f) again. In Figure 4.11 a is reported the plot of the drain current (I_{ds}) modulation for the water mixed with oil at 500 h of work, as an example. The OECT responses, expressed as the ratio $(I - I_0)/I_0$, where I is the *off* current (for gate voltages, Vg ≠ 0 V) and I_0 is the *on* current (for Vg = 0 V), were calculated and reported in Fig. 4.11 b.

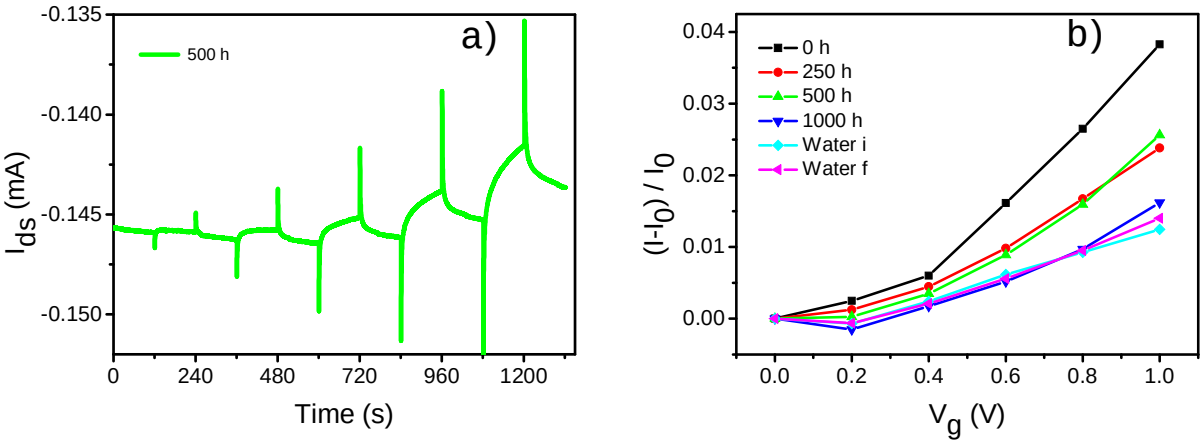

Fig. 4.11. Plot of the drain current (I_{ds}) modulation in a cotton-OECT for the water mixed with oil at 500 h of work and pulsing the gate voltage between 0 V and 1 V with 0.05 V steps (a). Plot of the normalized response ($\Delta I_{ds}/I_0$) of the transistor at different gate voltage for all waters (b).

The responses decreasing coherently with the increase of the age of the oil in agreement with the metal oxides gas sensors experiment previous described. It can be note also that the OECT responses for the ultrapure water is the same before and after the analysis of the waters extracted from the emulsions. The analysis of the waters extracted from the emulsions didn't damage or pollute the device and hence series of measures are allowed by using the same sensor. Concluding, it is successfully developed a new methodology to study and monitor the ageing of hydraulic oil with textile-OETCs sensors.

REFERENCES

[1] http://www.mondomacchina.it/it/la-manutenzione-dei-sistemi-oleodinamici-c1377.

[2] http://cordis.europa.eu/result/rcn/47157_en.html.

[3] http://www.rmffilter.com/products/condition-monitoring/oil-quality-sensor/.

[4] http://www.hydac.com/de-en/service/fluid-engineering/condition-monitoring/product-program/sensors.html.

[5] http://www.stauff.com/index.php?id=6871.

[6] http://www.te.com/content/dam/te-com/documents/sensors/global/FPC012_M_FPS2800B12C4%20Data%20Sheet.pdf.

[7] http://www.ifm.com/ifmit/web/news/pnews_9d7jvb.html.

[8] http://www.mecoil.net/monitoil-online-machine-tutor/.

[9] A. Mujahid, Monitoring automotive oil degradation: analytical tools and onboard sensing technologies, Anal Bioanal Chem (2012) 404:1197–1209..

[10] Zebing Mao, Distilling determination of water content in hydraulic oil with a ZnO/glass surface acoustic wave device, Microsyst Technol 2016, DOI 10.1007/s00542-016-2922-3.

[11] K. Sepcic, Diagnosis of used engine oil based on gas phase analysis, Analyst, 2004, 129, 1070 – 1075.

[12] S. Capone, Metal oxide gas sensor array for the detection of diesel fuel in engine oil, Sensors and Actuators B 131 (2008) 125–133.

[13] Z. T. Zhu, J. T. Mabeck, C. Zhu, N. C. Cady, C. A. Batt and G. G. Malliaras, Chem. Commun., 2004, 1556–1557.

[14] G. Tarabella, C. Santato, S. Y. Yang, S. Iannotta, G. G. Malliaras and F. Cicoira, Appl. Phys. Lett., 2010, 97, 123304.

[15] G. Tarabella, G. Nanda, M. Villani, N. Coppede, R. Mosca, G. G. Malliaras, C. Santato, S. Iannotta and F. Cicoira, Chem. Sci., 2012, 3, 3432–3435.

[16] G. Tarabella, A. G. Balducci, N. Coppedè, S. Marasso, P. D'Angelo, S. Barbieri, M. Cocuzza, P. Colombo, F. Sonvico, R. Mosca and S. Iannotta, Biochim. Biophys. Acta, Gen. Subj., 2013, 1830, 4374–4380.

[17] P. Lin, X. T. Luo, I. M. Hsing and F. Yan, Adv. Mater., 2011, 23, 4035–4040..

[18] G. Tarabella, M. Villani, D. Calestani, R. Mosca, S. Iannotta, A. Zappettini and N. Coppedè, A single cotton fiber organic electrochemical transistor for liquid electrolyte saline sensing, J. Mater. Chem., 2012, 22, 23830

CHAPTER 5

MONITORING OF THE ATMOSPHERIC POLLUTANTS GASES

5.1 INTRODUCTION

The atmospheric pollution is still a topical problem in most cities. Indeed, more than 90% of world population lives in urban areas where the pollutant concentrations often exceed the fixed limits. A study carried out by the World Health Organization estimated (2012 data) one million of deaths a year in China due to air pollution, six-hundred- thousand in India and 140000 in Russia [1]. Also in Europe, the situation is serious; Italy is one of the more pollutant country with twenty-one-thousand deaths a year, only preceded by Poland and Germany. Among the mortality factors more important in Europe, it has been pointed out pollution due to vehicular traffic, above all because of aged diesel vehicle fleet, having a negative effect both on particulate and nitrogen oxides. Globally, 3 million deaths were attributable to ambient air pollution (AAP) in 2012. In Fig. 5.1, the disability-adjusted life year (DALY) duo to AAP is reported, by country.

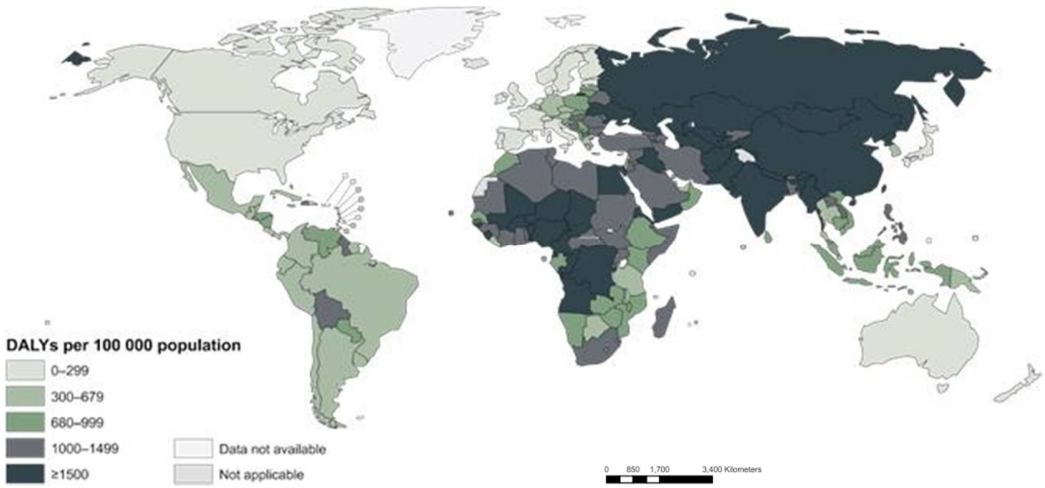

Fig. 5.1. Age-standardized DALYs per 100000 capita attributable to AAP in 2012, by country[1].

Road traffic and fuel combustion utilities strongly influence the air quality in urban atmosphere. The exhaust fumes released from motor vehicles, domestic and industrial flues are the cause of the atmospheric pollutants such as carbon monoxide, nitrogen oxides, sulphur dioxide, ozone, benzene, etc., greatly harmful to the human health and detrimental to monuments and historical buildings as well as ornamental materials.

In urban areas, the air quality can be considered as resulting from the overlapping of three different pollution components: regional background, urban background and hot spot events. For these last, the pollutants quickly reach very high concentration peaks, but they decrease just as much. Among the three components, the region and urban pollution affect the human health as well as the ecosystems conservation, being responsible of toxicity mechanisms connected to chronic exposure. Therefore, the continuous monitoring of these components is of a critical importance. In particular, the ability to separate the regional, urban and hot spot components is the key to define reduction actions of atmospheric pollution linked to the related sources and therefore, really effective.

Nowadays, monitoring is usually performed in few fixed stations, and trough mobile stations (where the conventional equipment is installed on vehicles) for temporary measurement campaigns or occasional environmental impact estimations. The equipment used in these stations is often complex, expensive and difficult to deploy, requiring controlled environmental conditions and frequent maintenance and calibrations.

In this frame, the technology of thick film gas sensors is an optimal candidate to be implemented in a portable, low cost, small-sized and versatile equipment to monitor diffusely pollutant. Recently, developments in the European legislation have caused a general change in the management of air quality assessment, making proposable the use of reliable solid state gas sensors to add to cumbersome spectrophotometric devices [2].

Such a monitoring technique would constitute an advantageous solution for a wide range of situations, as for example along the roads of city centers or along heavy traffic roads, or in historic centers where fixed monitoring stations cannot be used due to their large size.

The instrument developed for this work is a stand-alone system based on an array of metal oxide gas sensors (MOX) prepared via screen-printing technique. It has been realized to have low requirements in terms of power, consumables, maintenance and installation costs, including control electronics, firmware and interface software for the acquisition, processing and wireless transmission of the data, providing them in real time. The array of MOX sensors has been designed and realized to monitor the main atmospheric pollutants such as carbon monoxide, nitrogen dioxide, ozone and benzene.

5.2 REALIZATION AND CHARACTERIZATION OF THE MOX SENSOR ARRAY

To monitor traces of gases in atmosphere, not only the sensors must exhibit sensitivity and selectivity comparable to those of the conventional devices, but they also have to be highly stable, repetitive and reliable [3]. In order to validate the sensor responses, high repeatability of working conditions has to be attained; this task implies a careful co-ordination of all the different processes involved, such as functional material preparation and its morphological and structural characterization, deposition of sensing layers, fabrication of optimal substrates, and electronics engineering. Moreover, standardization of testing procedure, such as flow through technique is of paramount importance for a reproducible data processing [3].
The selection of the appropriate functional materials to detect the gases above mentioned has been made on the basis of many laboratory characterizations and of previous in-field monitoring experiments.

Here below, the different sensors prepared and characterized for this application are listed:

a) A solid solution $(Ti,Sn)O_2$ to detect carbon monoxide and named TS;

b) $LaFeO_3$ as functional material to detect nitrogen dioxide and named LF;

c) Tungsten trioxide (WO_3) for ozone detection and named W1;

d) A solid solution of titanium, tantalum and vanadium as functional material to detect BTX and named TTV.

The synthesis methods of the materials used to prepare the sensors have been described in chapter 2, while peculiar characteristics of ST sensor have been described in chapter 1. Hereafter, few electrical characterizations will be reported to highlight the specific properties toward the gases of interest.

Carbon monoxide detection - In Figs. 5.2 and 5.3, an example of measurement to determine the response to different CO concentrations as a function of some humidity concentrations and the relative dynamic measurement are reported. It can be observed that ST sensors are not particularly influenced by humidity; in fact, they are able to detect very low concentrations of carbon monoxide, down to 200 ppb and even less, also in presence of noticeable values of humidity. However, in very harsh ambient conditions, the sensors could need a compensation caused by an overestimation of CO by the action of humidity. In fact, the main interfering gas for MOX sensors, is the water vapor partial pressure. To take into account of this effect, it is necessary to determine calibration surfaces rather than 2D-curves. Indeed, it can be experimentally demonstrated that the conductance can be fitted with an equation,

representing an analytical surface and containing three terms: two of them are perfectly fitted by power law equations with proper parameters, while the third is an interaction term which is proportional to $p_{H_2O}^{\alpha}[CO]^{\gamma}$, α and γ being the same exponents as those in the single power laws. The constant parameters must be derived from a fit of the experimental values, obtained injecting different CO concentrations under different partial pressures of water vapor [4,5].

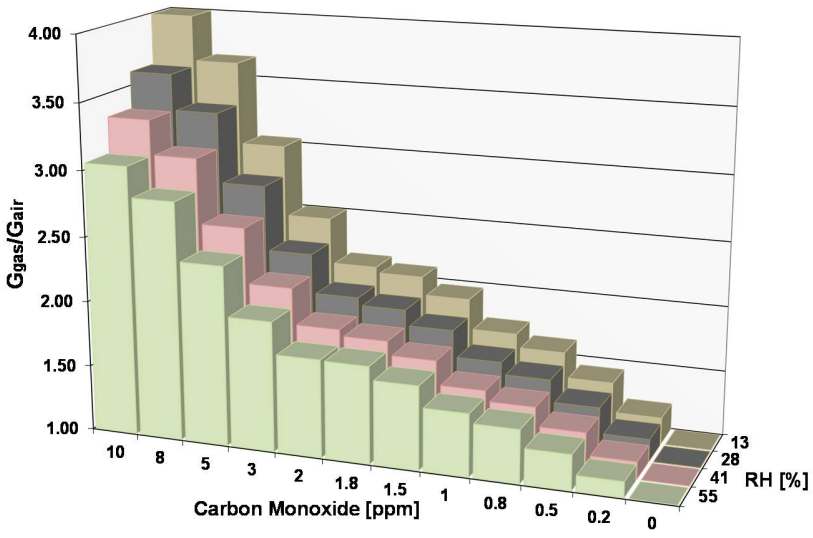

Fig. 5.2. Responses of a TS sensor in different conditions of relative humidity (from 13 to 55%) to carbon monoxide ranging to 0.2 to 10 ppm.

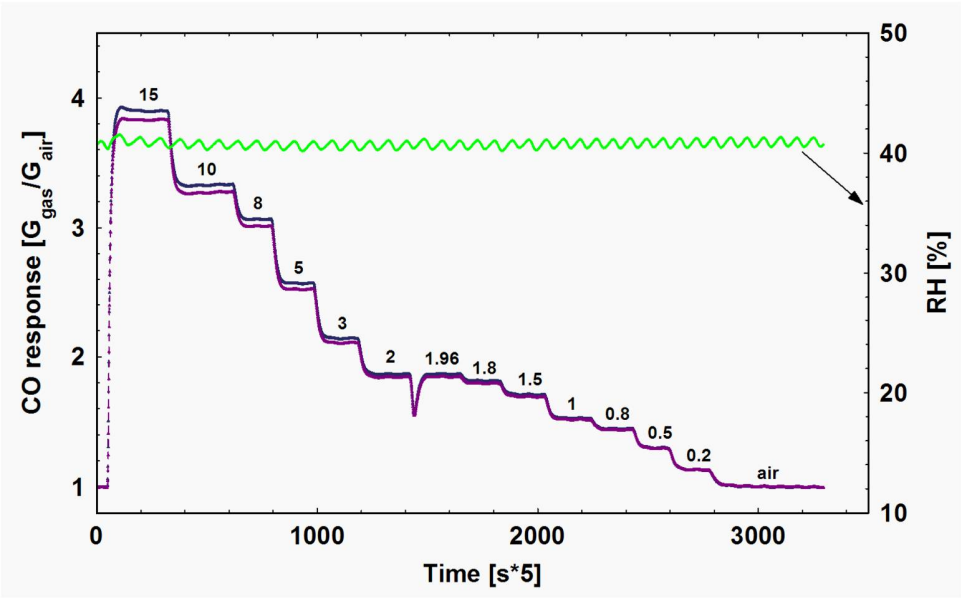

Fig. 5.3. Dynamic responses of two TS sensors at different CO concentrations carried at 41 % of relative humidity. *Nitrogen dioxide detection* - For nitrogen dioxide detection, the sensor has been prepared using

iron lanthanum oxide. Among the functional characteristics of this sensor, a good sensitivity to nitrogen oxides is accompanied by a low sensitivity to carbon monoxide, although not inconsiderable. In Fig. 5.4, an interference test shows that, at concentrations lower than 1 ppm of NO_2, 100 ppm of CO can invalidate the measure. However, in atmospheric environment such a situation cannot occur; thereby an interference by CO can lead up an underestimation for NO_2. Despite such defects, LF sensor is preferable with respect to other sensors, such as WO_3, which is more sensitive to NO_2, but, at the same time, it is also particularly sensitive to ozone. The result is that, during summer, in which photochemical pollution is prevalent, WO_3 sensor is able to detect ozone but not NO_2. In fact, the interference from ozone in atmospheric environment is a drawback with respect to NO_2 detection.

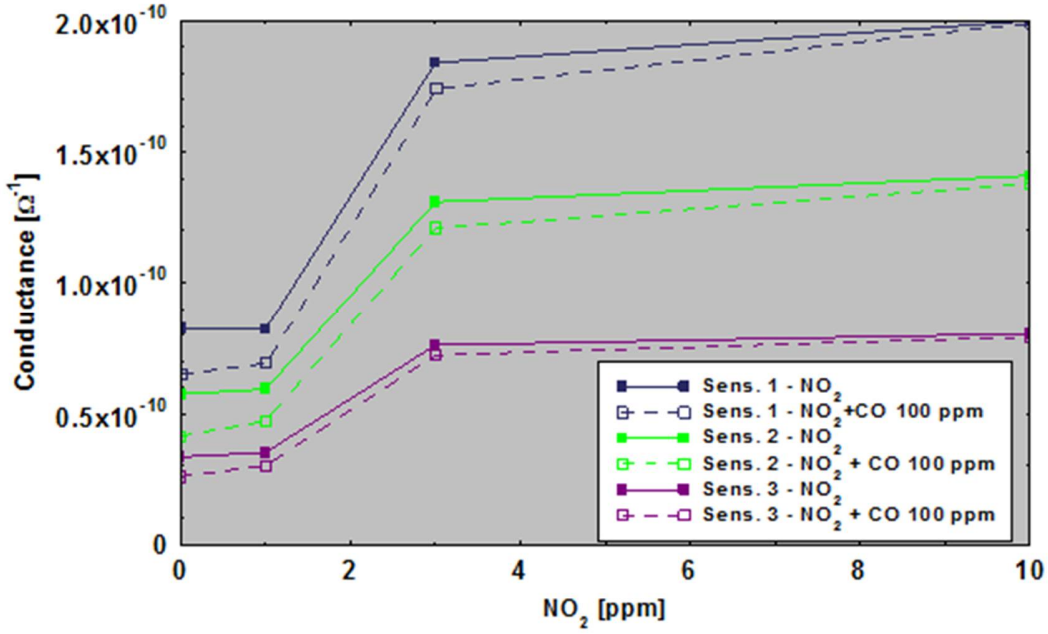

Fig. 5.4. Interference test performed injecting 100 ppm of CO in a mixture of 1, 3 or 10 ppm of NO_2 in air from for three LF sensors, nominally identical.

Ozone detection – As above described, the sensing characteristics of WO_3 sensor, much more devoted to oxidizing gases like NO_2 and O_3 rather than LF sensor, suggested us to test in field WO_3 based sensor as ozone sensor, while LF sensor toward NO and NO_2 right for lower interference from ozone particularly intense in summertime.

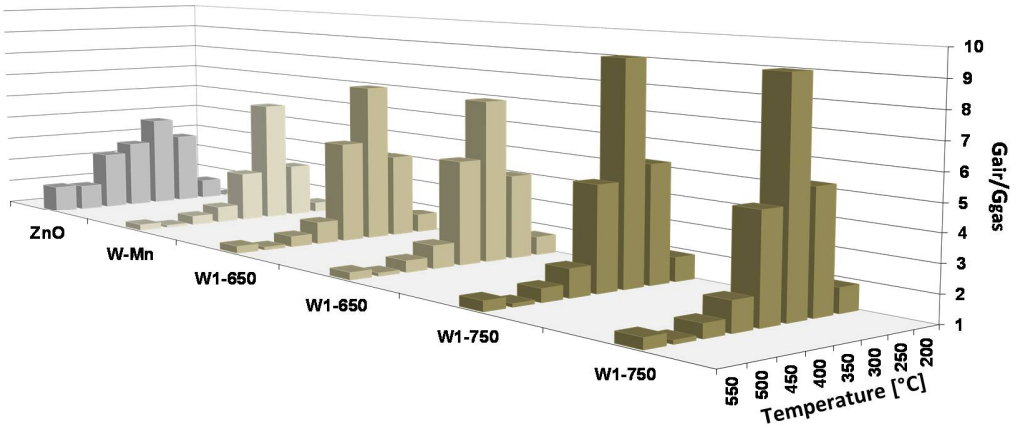

Fig. 5.5. Responses to 50 ppb of ozone for different sensors at working temperature ranging from 200 to 550°C.

In Fig. 5.5, a test to select the appropriate functional material to detect ozone in addition to the appropriate firing temperature and the best working temperature is shown. It can be noted that the sensors with lower firing temperature are more sensitive to ozone. It means that, being the oxidizing gases like NO_2 and O_3 strongly reactive on the semiconductor surface, the grain size is not so crucial as in the case of reducing gases for which, instead, the ratio between the surface area and the volume must be maximized.

BTX detection – To detect aromatic hydrocarbons, a solid solution of titanium, tantalum and vanadium has been used as functional material. The electrical characteristics of this sensor, named TTV, are very attractive due to a very low response to carbon monoxide compared to the response to aromatic hydrocarbons, like benzene and toluene. The Figs. 5.6 A and B highlight this feature; indeed the bars of gray color are relating to TTV sensors, while the other bars represent the responses of other functional materials.

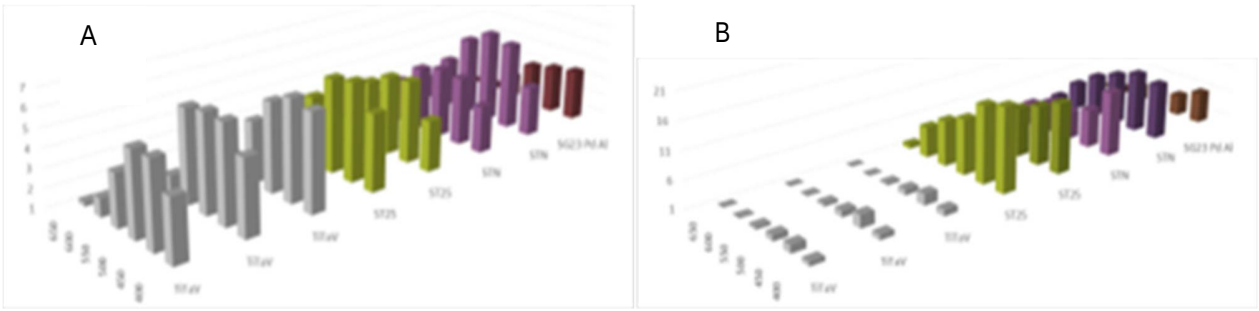

Fig. 5. 6. Response to 2 ppm of benzene (A) and to 50 ppm of carbon monoxide (B) for TTV sensors (gray color).

5.3 THE MONITORING UNIT

Arrays of semiconductor oxides thick film gas sensors, assembled in small remotely controlled units, have been used for on-site tests. A monitoring unit consists in a small box to lodge the sensors, the electronic circuitry related to each sensor and a main electronic control unit provided with serial connection. The electronics is consisting of a system for measuring the sensors' signal and of a circuit to control the working temperature of each sensor and an analogic/digital converter. The microprocessor of the main electronic control unit, through an appropriate firmware, operates all operations: acquires the vales measured by the analogic section; records the data in a data logger converting them in gas concentration through appropriate algorithms; finally it transfers the data through a serial connection to a GSM module which sends them to an input data server, on request. The analogic section is mainly constituted of the two circuits reported in Figs. 5.7 A and B for sensing film resistance measurement and control of resistance heater.

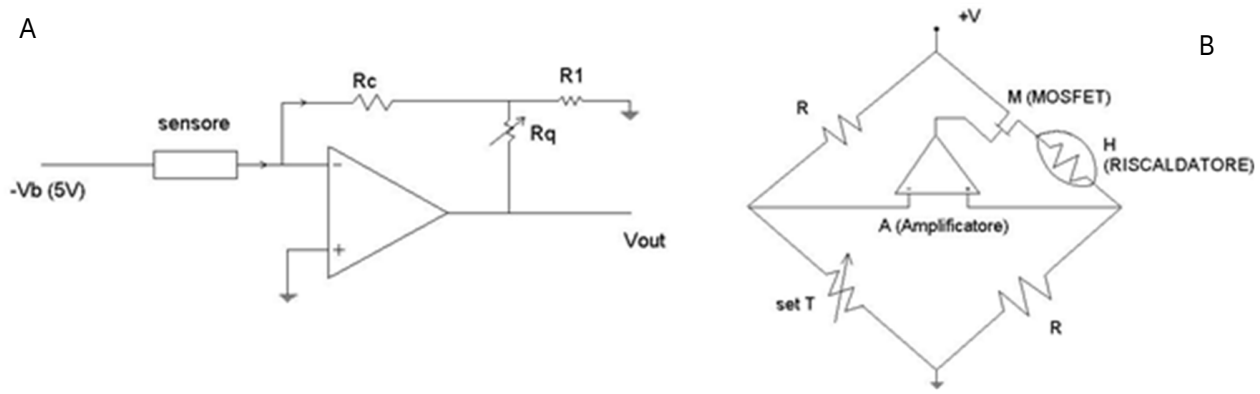

Fig. 5. 7. Circuit for sensing film resistance measurement (A); circuit for working temperature control (B).

To measure sensor resistance (Fig. 5.6 A), a temperature compensated tension generator gives a supply voltage of 5 V. An electrometric operational amplifier converts current in tension. The conversion ratio can be changed in the range 1 – 100 of the base value through a digital potentiometer. The operating temperature circuit works on the base of the value of the heater resistance (Fig. 5.6 B). To obtain temperature stability, the circuit works by means of a Wheatstone bridge, in which the heater is a branch of the bridge. The opposite branch contains the digital potentiometer, which selects the desired temperature, the other two branches containing two fixed resistances. If a disequilibrium is revealed by the amplifier, a MOSFET changes the current of the heater to balance the current trough the bridge.

In Fig. 5.8 A an image of a monitoring unit realized for this work (A) is reported, while in Fig. 5.8 B the block containing the four sensor modules is highlighted.

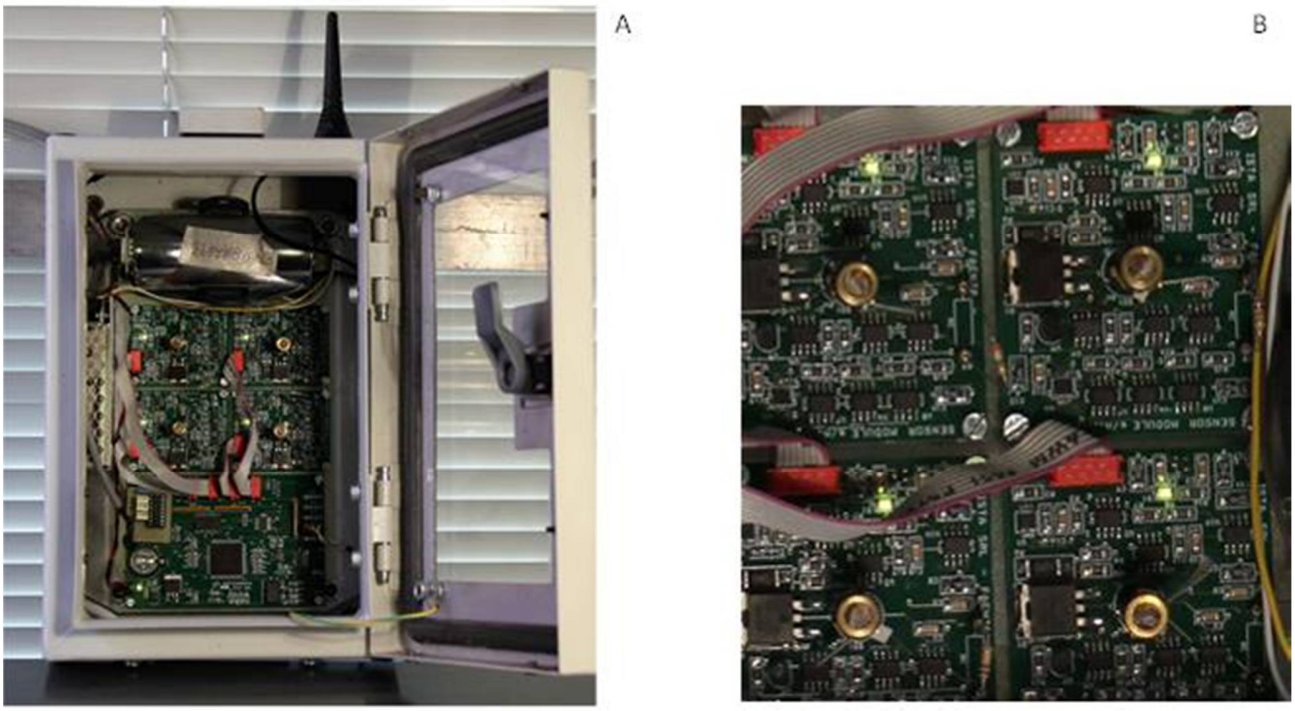

Fig. 5.8. Image of the monitoring unit (A); the block containg the four sensor modules (B).

A software in Labview environment has been developed. It allows to remotely control the monitoring unit, permitting to change the working temperature of the sensors, to adjust their base line and to download the data. Moreover, it is possible to apply the conversion algorithms to display the sensor signals in the appropriate measures the gas concentrations.

5.4 TEST IN FIELD THROUGH THE MONITORING UNITS

First of all, few units have been exposed to the real atmosphere beside a fixed-site monitoring station for air quality control with the aim to validate the values of gas concentrations obtained through the array of MOX sensors. For this aim, the temporal evolution of the conductivity changes of the sensors (expressed as G_{gas}/G_{air}) have been studied in comparison with the concentrations of CO, C_6H_6, NO, NO_2, and O_3 in the atmosphere as measured by the analytical instruments. In particular, IR

spectrophotometer for carbon monoxide, UV spectrophotometer for ozone, chemiluminescence analyzer for NOx and finally, gas chromatograph for BTX.

CO monitoring – It has been observed that the water vapor partial pressure is the main interfering gas for MOX sensors, especially for carbon monoxide detected through a tin oxide sensor. However, TS sensor is based on a functional material with poor water vapor adsorbability, so it can be used in almost every situation without to do compensation for humidity. As mentioned above, For particularly severe conditions, for example in presence of very low carbon monoxide concentrations in an environment with high content of water vapor partial pressure, could became necessary to apply the compensation algorithm.

In Figs. 5. 9 A and B, a comparison between the responses of TS sensor exposed to real atmosphere and the values of CO concentrations as measured by IR analyzer are reported. It can be observed that the best fit calculated from the two comparisons gave rise to the same curve (a straight line) with the same values of the parameter *b*, although the values of CO concentrations were very different during the two periods of monitoring. Indeed, in the first case CO concentration ranged between 0.2 and 3.5 mg/m^3, while in the second period of monitoring CO concentration did not exceed 1.2 mg/m^3.

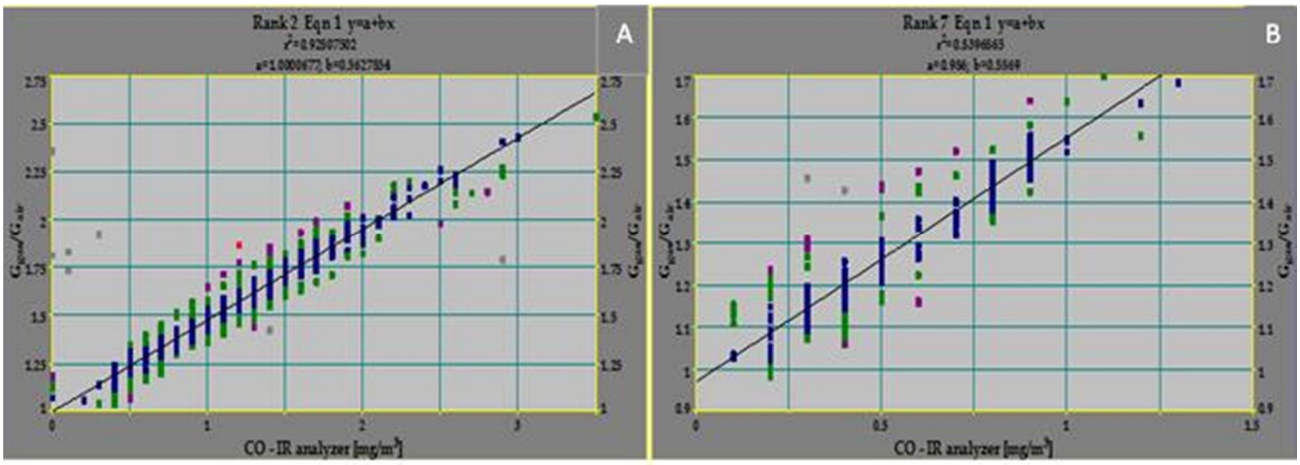

Fig. 5.9. Comparison between the measurements of the sensor unit and the IR-spectrophotometer in two periods of monitoring with: (A) very high and (B) very low concentrations of carbon monoxide.

Using the calibration curve of the Fig. 5.9, obtained comparing the responses of the sensor with the values of carbon monoxide (considered as true values) measured through an IR analyzer, a forty days of continuous monitoring has been carried out. The monitoring was performed in Ferrara in winter time beside a fixed monitoring station at a traffic site. In Fig. 5.10, the carbon monoxide concentrations

measured through TS sensor are reported. The comparison with the conventional analyzer resulted in very good agreement.

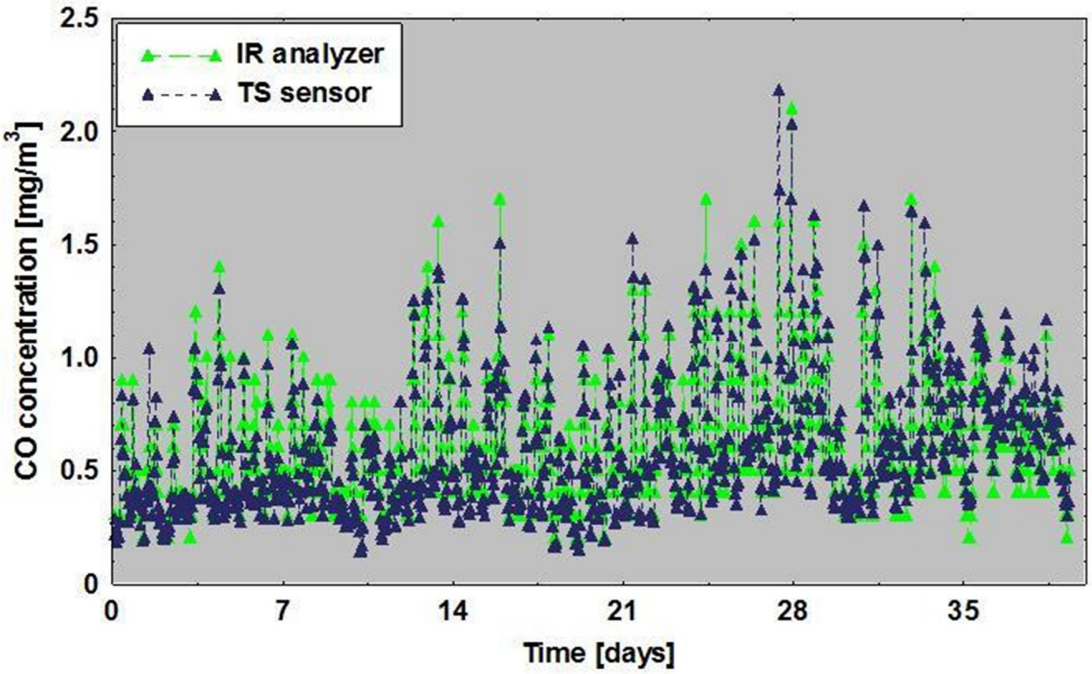

Fig. 5.10. Forty days monitoring of carbon monoxide through TS sensor carried out in winter time in Ferrara.

NO_2 monitoring - To monitor nitrogen dioxide, a sensor based on iron lanthanum oxide as functional material has been used, as above described. Unfortunately, such material needs a certain activation time, on the other hand it is less affected by the presence of ozone, with respect to other materials like WO_3. In the diagram of Fig. 5.11 a monitoring of NO, NO_2 and NOx is reported, compared with the signal of $LAFeO_3$ sensor. An observation regards the direction of increase of the signal, opposite to the increasing of gas concentration. This is correct because $LAFeO_3$ is a semiconductor of p type, in which the majority carriers are holes and not electrons. Moreover, since NO_2 is a secondary pollutant, the concentration curve appears flattened with respect to the NO one, being this last a primary pollutant. The LF response is slower than the NO trend, while quite well replying the NO_2 trend. In Figs. 5.12 A and B, the two different observed trends are reflected in the two calibration curves obtained comparing the sensor response with the concentrations of NO_2 and NOx as measured through a chemiluminescence analyzer. Indeed, in both cases the fit equation is correctly a power law; in the case of NO_2 the exponent *c* is equal to *1*, while for NOx, *c* is *0.5*.

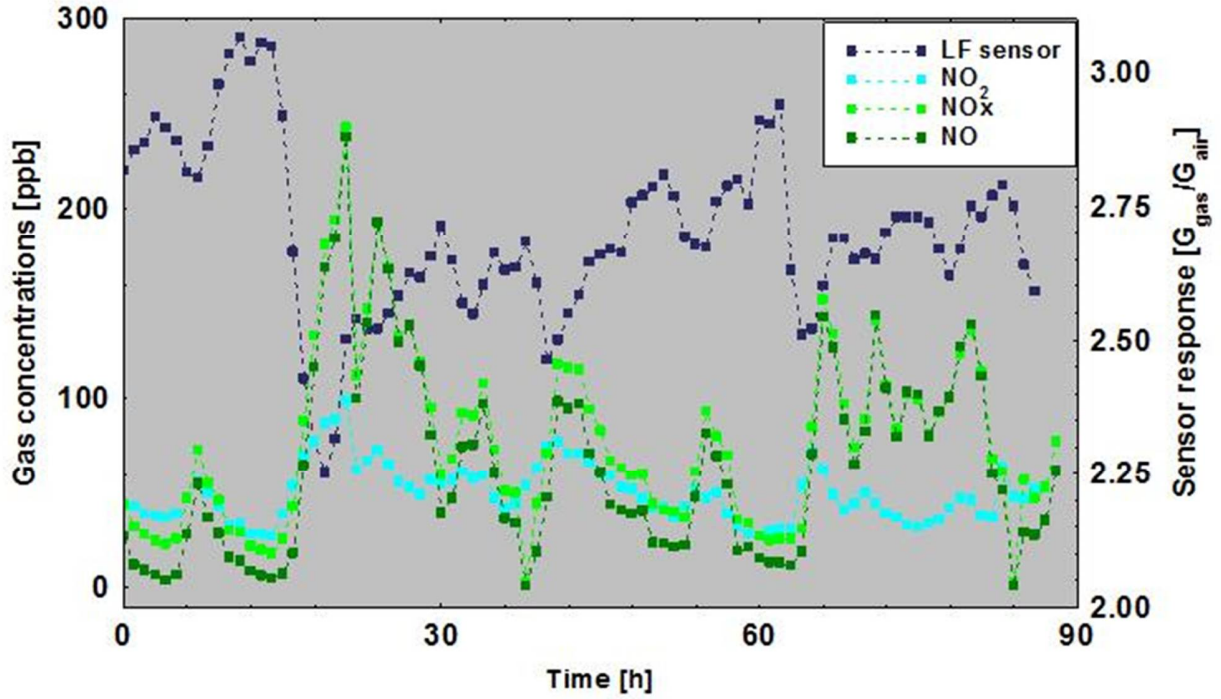

Fig. 5.11. Dynamic responses of LF sensor to the mixture of nitrogen oxides compared with the concentrations of NO,NO_2 and NOx as measured through a chemiluminescence analyzer.

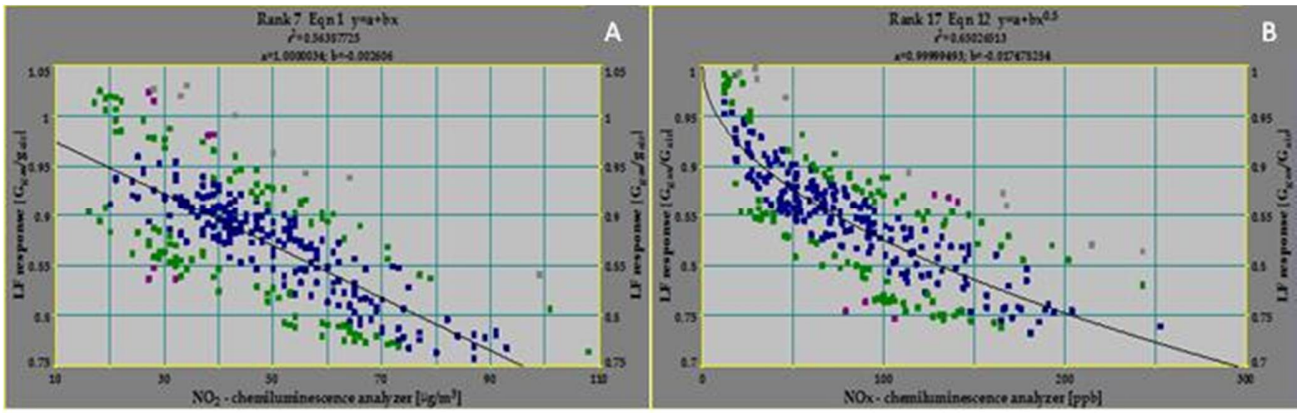

Fig. 5.12. Monitoring of one month performed through a LF sensor in comparison with a chemiluminescence analyzer to verify the calibration curve in real atmosphere for NO_2 (A) and for NOx (B).

Recently, two units like that of Fig. 5.8 have been placed at Physics Department of University of Naples "Federico II" and at monumental site "Maschio Angioino" (leaning out of an arterial road of heavy traffic close to docklands) monitoring the air quality for six months. In Fig. 5.13, a comparison between NO_2 concentration in the two monitoring sites (from 10th to 28th of November 2016) is shown.

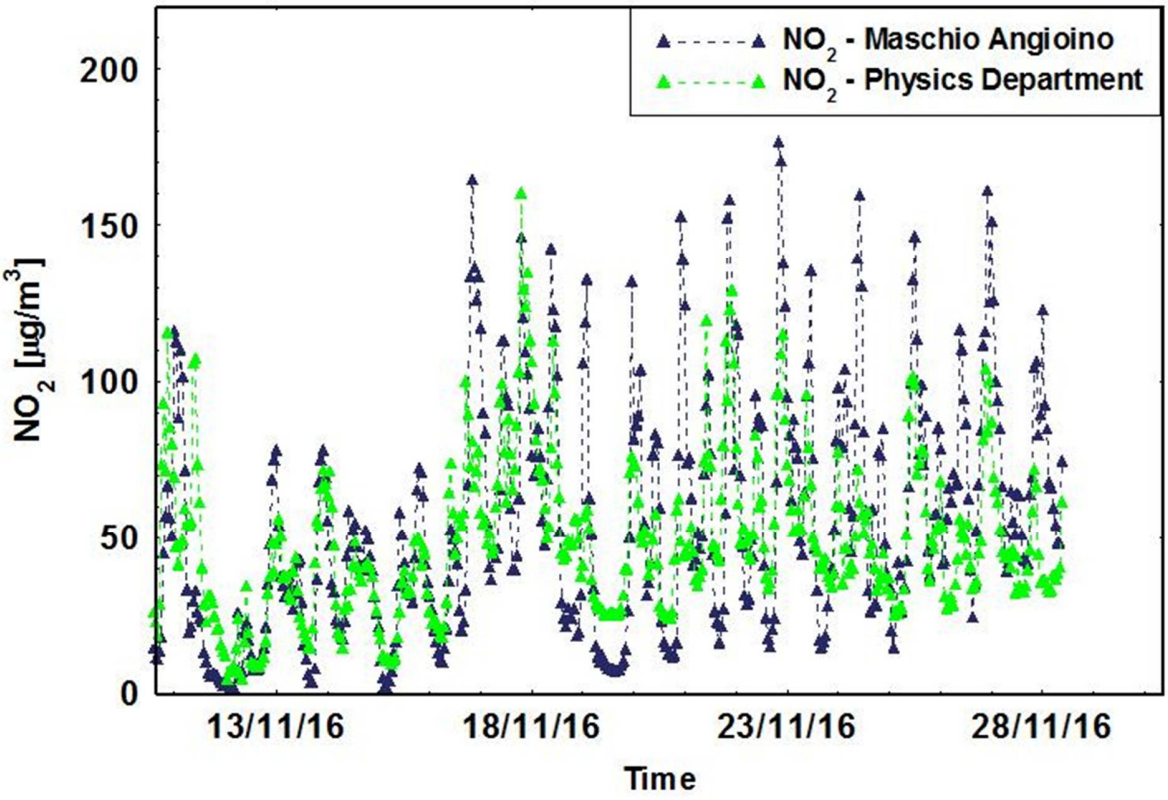

Fig. 5.13. A comparison between the NO_2 concentrations measured through LF sensors in two sites in Naples: monumental site "Maschio Angioino" and Physics Department of the University of Naples "Federico II".

O_3 monitoring – as previously described, WO_3 sensing characteristics, much more addressed to oxidizing gases than $LaFeO_3$ such as NO_2 or O_3, suggested to test in field the WO_3 based sensor, named W1, as ozone sensor. As mentioned above, to be able to detect gases with similar physicochemical properties, like NO_2 and ozone, great attention to select and synthesize the functional materials must be paid. $LaFeO_3$ and WO_3 exhibit similar properties versus the two gases of interest. However, there are evidences to consider WO_3 the best candidate to detect ozone and $LaFeO_3$ for NO and NO_2. In Fig. 5.14, two different comparisons between the W1 responses and a UV-spectrophotometer as conventional analyzer are reports. The two comparisons are referred to different environment situations, both as regards the season and the city. A good agreement has been highlighted between W1 sensor and UV analyzer, resulting in both cases a straight line as calibration curve with very similar values of the parameter *b* [6].

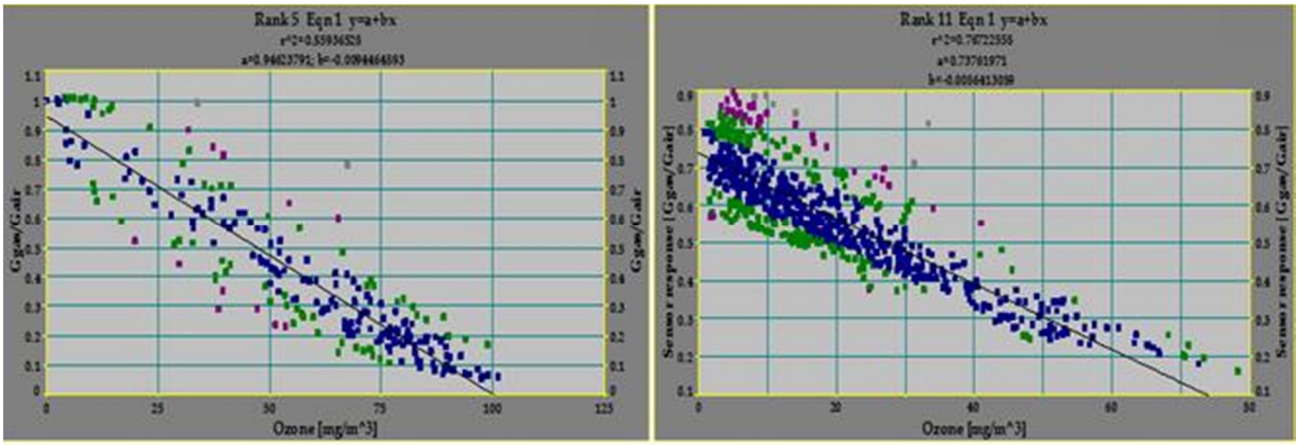

Fig. 5.14. Comparisons between the responses of WO_3 sensors to ozone and the O_3 concentrations as measured through an UV spectrophotometer.

In Fig. 5.15, the dynamic responses of a WO_3 sensor compared with the ozone concentrations as measured trough a conventional analyzer are reported. The data are expressed in both cases as hourly average obtaining an agreement quite good. The graph is relating to one month of monitoring, while, in the inset, a zoom on few days is shown.

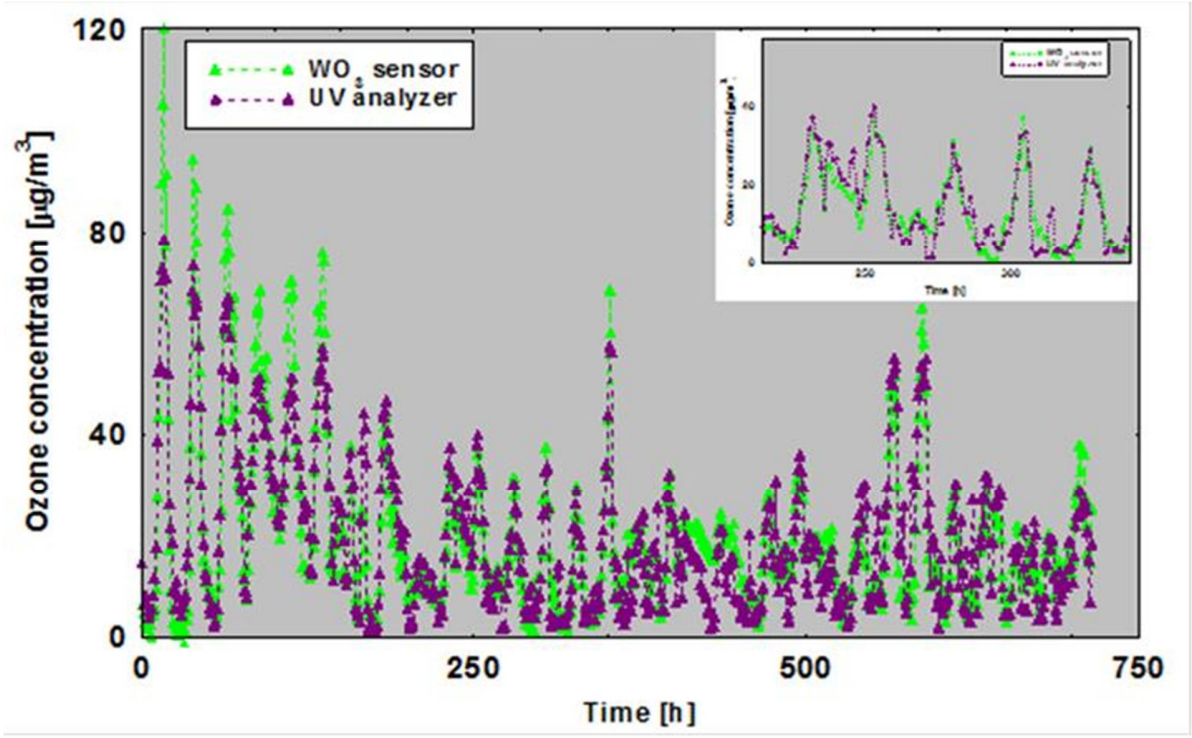

Fig. 5.15. Dynamic responses of a WO_3 sensor compared with the ozone concentrations as measured trough a conventional analyzer; in the inset a four-day detail of the monitoring.

BTX monitoring – In the monitoring of the Fig. 5.16, the responses of two TTV sensors, nominally identical, lodged in two different monitoring units are reported. The monitoring was about four months long. It can be observed the same trend for the two sensors maintained for the entire monitoring. Only a small difference in response can be observed, no necessarily due to sensors, but also to electronics. It can be also observed the same trend of the gas-chromatograph, highlighted in Fig. 5.17 where seven days of monitoring are reported.

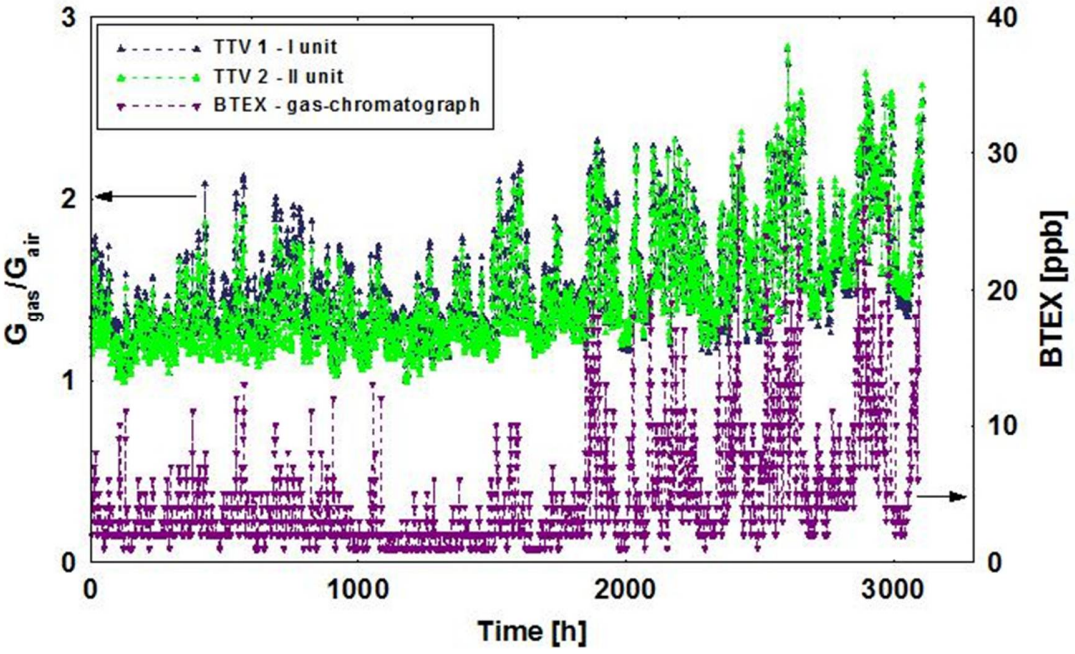

Fig. 5.16. Comparison of two monitoring units (TTV sensors) in a monitoring four months long.

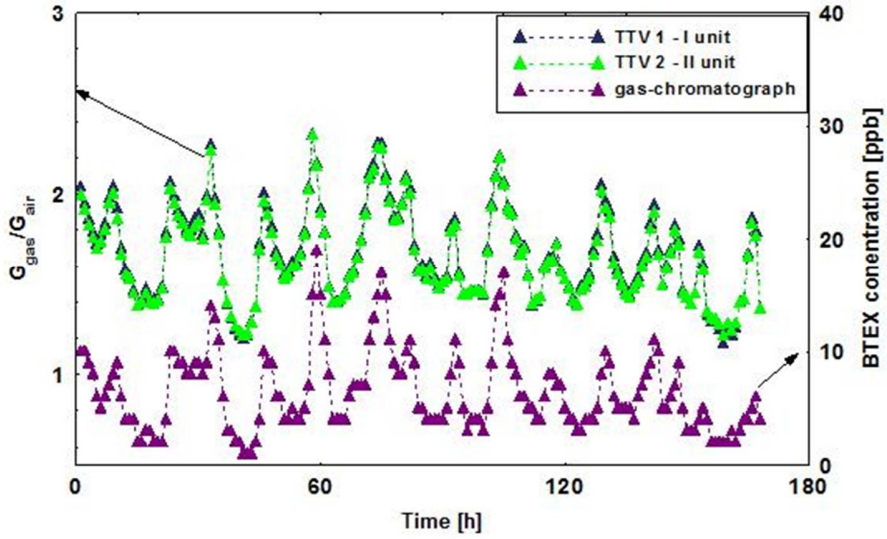

Fig. 5.17. Detail of the Fig. 5.16

As described above, a unit like that of Fig. 5.8 have been placed at Physics Department of University of Naples "Federico II". As an example of the complete data output provided by the monitoring unit, in Fig. 5.18 it is reported a monitoring carried out from 14 - 22 August, 2016.

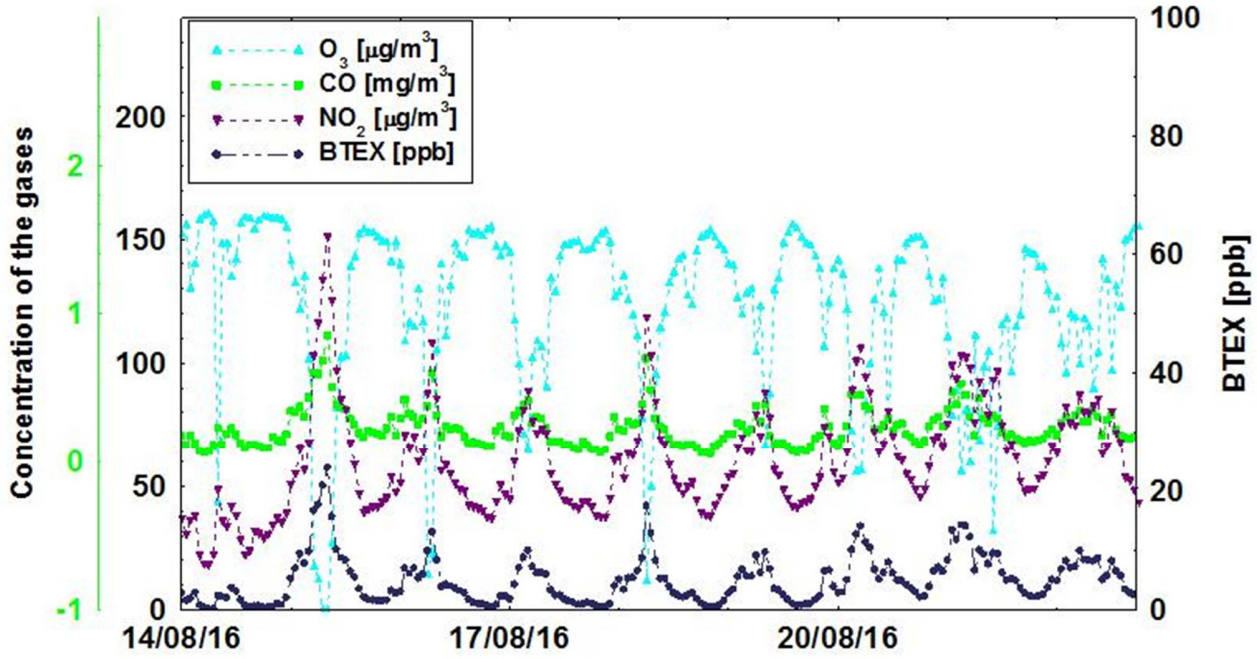

Fig. 5.18. Output of the array of thick-film sensors during field tests on August 14-22, 2016.

REFERENCES

[1] Ambient air pollution: a global assessment of exposure and burden of disease, @World Health Organization 2016.

[2] DIRECTIVE 2008/50/EC on ambient air quality and cleaner air for Europe.

[3] M. C. Carotta, M. Benetti, E. Ferrari, A. Giberti, C. Malagù, M. Nagliati, B. Vendemiati, G. Martinelli, Basic interpretation of thick film gas sensors for atmospheric application, Sensors and Actuators B 126 (2007) 672–677.

[4] C. Malagù, M. Benetti, M.C. Carotta, A. Giberti, V. Guidi, L. Milano, G. Martinelli, Investigation of the humidity effects on SnO_2-based sensors in CO detection, Proc. MRS 2006—Spring Meeting, Symposium R.

[5] A. Fioravanti, A. Bonanno, S. Gherardi, M. C. Carotta and A. N. Skouloudis, A portable air-quality station based on thick film gas sensors for real time detection of traces of atmospheric pollutants, IOP Conference Series: IOP Conf. Series: Materials Science and Engineering 108 (2016) 012005.

[6] M. C. Carotta, C. Malagù, A. Cervi, S. Gherardi, A. Giberti, G. Martinelli, S. Zampolli, I. Elmi, E. Cozzani, F. Mancarella, L. Masini, G. C. Cardinali, A portable integrated air quality monitoring station for real-time quantification of BTEX, CO, NOx and O_3, Ecomondo 2009.

CONCLUSIONS

This work has been devoted to the development, study and innovative applications of nanostructured metal oxides as well as gas sensors prepared through screen-printing technique.

Among the functional materials prepared, a great attention has been focused onto ZnO nanomorphologis (Chapter 3). In spite of many years of investigation, some of the basic properties, behaviors and growth mechanisms of nano-ZnO still remain unclear. On the other hand, zinc oxide is certainly an appealing material because of its aptitude for being grown by a great deal of methods in a wide diversity of morphologies obtaining the widest family of unique nanostructures among all known materials. It also exhibits a wide range of properties such for example the fact to be a wide band gap semiconductor oxide that makes it a suitable material to prepare metal oxide gas sensors. The first step of this study was devoted to the rapid synthesis of several nanomorphologies (nanoparticle aggregates in form of rhombic sheets and bisphenoids, short and long needles, nano and micro flowers and hexagonal prisms) with a controlled and homogenous distribution in size, for all samples. A great detailed description of the influence of various synthesis parameters (presence of solid precursor, synthesis temperature, sonication treatment, etc.) onto the obtained morphology was also reported, highlighting some new aspects not present on literature. To better understand the effect of different morphologies onto the zinc oxide nanomaterial properties, their electrical and spectroscopic behavior were examined. Moreover, ZnO gas sensors have been tested toward several reducing gases (acetone, isoprene, ethanol, ammonia, etc.) typically of the exhaled human breath with the aim to use them in breath gas analysis for diagnosis of metabolic diseases. It turned out that all sensors based onto different ZnO nanomorphologies are mainly sensitive to acetone, the films constituted of nanoparticle aggregates detecting acetone concentrations down to few tens of ppb. For this application, a dedicated system with a very small test chamber (in which only one sensor is lodged) has been realized, strongly decreasing the response and recovery time and allowing the breath monitoring in near real time.

A second concrete and challenging implementation in industrial framework of the thick film gas sensors realized has been concerning the monitoring of the hydraulic oil aging (Chapter 4). The main cause of failure in fluid power systems or machines is the degradation of the hydraulic oil caused by temperature, friction, contaminated by particles and presence of water. A failure involves a drop in machine

reliability, an injection in the ambient of pollutant material (leakage of hydraulic oil) and a not planned stop machine. This is a novel approach (currently in patent stage) to the monitoring the hydraulic oil status in real time and on-board both from a methodological and instrumental standpoint. The same type of hydraulic oil was aged and collected using an hydraulic test bench developed at IMAMOTER-CNR and directly in a agrimotor. The oil samples were characterized by means of gas chromatography and of a laboratory system, based on MOX sensors, specifically prepared for this aim. Both characterizations showed a lower analytes concentration in the more aged samples. It was therefore highlighted a correlation between the hydraulic oil aging and the composition of their vapors.

For this application, oil samples were also analyzed through organic electrochemical transistor (liquid sensors) developed at IMEM-CNR (Dr. Nicola Coppedè) because of their advantageous properties: low cost, small dimensions, easy to read, long term stability and reversible use. The textile structure of the device could be used to absorb spontaneously the fluids and measure their electrochemical properties, in simple and direct way without the employment of a microfluidics system. In this contest a novel employment of Textile-OECTs has been studied. Indeed the hydraulic oils, being non-polar fluids, cannot work as an electrolyte solution. For this reason, a new challenging procedure was developed and tested to extract from the oil through a mixing process with water, small molecules with an hydrophilic behavior. The analysis of the extracted water enables the monitoring of the hydraulic oil ageing through the organic electrochemical transistors again showing the same correlation: a lower analytes concentration in the more aged samples. It was demonstrated the possibility to monitor the hydraulic oil ageing in real time and on-board through novel methodologies, by using MOX sensors or Textile-OECT sensors. The two developed devices can prevent the breakdown in hydraulic machines, a direct consequence of the hydraulic oil degradation, providing a new solution for the predictive maintenance.

The last MOX sensors application, object of this thesis work (Chapter 5), was the monitoring of traces of main atmospheric pollutant gases. The atmospheric pollution is still a topical problem in most cities. The exhaust fumes released from motor vehicles, domestic and industrial flues are the main cause of the atmospheric pollutants such as carbon monoxide, nitrogen oxides, sulphur dioxide, ozone, benzene, etc., greatly harmful to the human health as well as the ecosystems. Therefore, the continuous monitoring of these components is of a critical importance to define reduction actions of atmospheric pollution. Nowadays, monitoring is usually performed in few fixed stations, and trough mobile stations (where the conventional equipment is installed on vehicles) for temporary measurement campaigns or occasional environmental impact estimations. The equipment used in these stations is often complex, expensive and

difficult to deploy, requiring frequent maintenance and calibrations. In this frame, the technology of thick film gas sensors is an optimal candidate to be implemented in a portable, low cost, small-sized and versatile equipment to monitor diffusely pollutant. For this aim, a stand-alone monitoring station based on MOX sensors prepared during this work has been realized, including electronics for acquisition, processing and wireless transmission of the data, providing them in real time. A particular attention has been addressed to the development of a suitable sensor for each pollutant gas to detect (carbon monoxide, nitrogen dioxide, ozone and benzene). The in-field experiments performed during this work concerned an industrial zone in Ferrara in addition to a monitoring in Naples at monumental site of "Maschio Angioino" (project on behalf of the University of Naples "Federico II") leaning out of an arterial road of heavy traffic close to docklands. The comparison performed between the temporal evolution of the conductivity changes of the sensors with the pollutants' concentrations, as measured by the analytical instruments located in fixed monitoring stations managed by ARPA resulted in good agreement.